HIGH TEMPERATURE EROSIVE WEAR OF A BOILER TUBE STEEL

By

Martin Suckling

A thesis submitted to the Faculty of Engineering of the University of Cape Town in fulfillment of the requirements for the degree of Doctor of Philosophy

Department of Materials Engineering
University of Cape Town
November 1996

ABSTRACT

This work is an attempt to evaluate the influence of critical operational parameters on the high temperature erosion of a 1Cr½Mo boiler tube steel. Erosion testing has been carried out in a specially designed and developed unique laboratory apparatus capable of simulating the conditions of temperature, particle velocity and flux as found in the economiser region of pulverised fuel boiler combustors in electricity generation power plants. The work has encompassed the effects of particle type, size, velocity and flux on the erosive wear rates of the 1Cr½Mo boiler tube steel at temperatures of up to 600°C. The response of the target to impacting erodent particles has been analysed using scanning electron and optical microscopy, transmission electron microscopy (TEM) as well as conducting cross-sectional microhardness tests. The change in the mechanical properties of the steel was determined by conducting tensile tests over a range of temperatures from 20°C to 565°C.

The effect of particle type on wear rates has been found to be significant, with the denser, harder silicon carbide (SiC) and silica sand (SiO_2) particles causing greater erosion than the friable plant coal ash. The effect of particle size has also been found to be significant. SiC and SiO_2 particles with a diameter of between 63-106μm cause up to 100% more wear than the larger 106-125μm particle size range. However, the use of plant fly ash as an erodent did not result in significant differences in erosion rate with changing size. Explanations for these effects takes into account factors such as aerodynamic forces and experimental error in the particle velocity calibration.

The effect of particle velocity was found to be substantial. Erosion rates were found to be proportional to the particle velocity raised to an exponent of 1.90 at 20°C for plant fly ash. SiC and SiO_2 velocity exponents were found to decrease slightly with increasing temperature. As the steel becomes less sensitive to particle impact due to its decreasing strength and increasing ductility.

A sharp decrease in erosion rate was found as the particle flux was increased beyond $2.1 kg.m^{-2}.s^{-1}$ at a velocity of $24 m.s^{-1}$. This decrease has been shown to be due to

extensive particle shielding of the target at a critical flux which is related to the mean distance between successive particles whilst still in flight.

In the high temperature gas blast apparatus, material removal was not affected significantly by oxide layer growth which remained dominated by erosion wear processes at all temperatures. The increased ductility and lowering of strength of the steel with an increase in temperature leads to much increased wear rates particularly above 300°C using the harder erodents. The softening of the ash with a rise in temperature was found to lower its erosivity resulting in minimal increases in the erosion rate of the steel with increasing temperature.

A thermal diffusion model has been used to examine the possibility of a cumulative heating effect causing material melting due to successive particle impacts. Cumulative heating was shown not to take place and isothermal conditions prevailed due to rapid heat diffusion through the steel.

Recommendations are made for combating erosive wear in the pulverised fuel boiler combustor industry through modifying flow conditions within the boiler to eradicate localised areas of high velocity and high particle mass loadings.

ACKNOWLEDGEMENTS

I wish to thank all of those who assisted me throughout this project, but in particular :

Professor C. Allen, my supervisor, for his consistently good advice and encouragement.

Messrs B. Greeves and J. Peterson for photography, messrs G. Newins and N. Dreze for technical support and design advice and Mrs M. Topic for laboratory assistance.

Mr C. Wicker and Mr R. Wellman of the Technology, Research and Investigations Group of Eskom for supplying materials and fly ash and for technical and scientific advice.

The staff and students in the Department of Materials Engineering for their support and encouragement.

Finally, the South African Foundation for Research and Development and Eskom for the provision of financial support.

Dedicated to my parents, Derek and Hilary Suckling for their unfailing support over the years.

TABLE OF CONTENTS

LIST OF ILLUSTRATIONS

LIST OF TABLES

1. Introduction

Erosion has been defined as the gradual removal of material by successive solid or liquid particle impacts and has been noted in many areas of engineering. These include :

- Erosion of turbine blades in aero-engines [1], gas turbines [2] and steam turbines [3]
- Erosion of boiler tubes in fluidised bed boiler combustors [4].
- Erosion of pipe bends in pneumatic conveyor lines transporting pulverised coal [5].
- Fly ash erosion of boiler tubes in pulverised fuel boiler combustors [6]

The principle of generating electricity from coal using fluidised bed combustors and pulverised fuel combustors is to utilise the thermal energy in the coal to raise the temperature and pressure of steam to a high enthalpy. The steam is then passed through high strength, low alloy steel tubes and expanded through turbines coupled to electrical generators.

In a fluidised bed an air draft feeds oxygen to a burning coal bed. The combustion gases and excess air then levitate a bed of particulates, which surround boiler tubes. Heat transfer to the tubes is by the bed particles, which are packed closely around the tubes, as well as the combustion gases. Heat transfer rates can be 2 to 3 times higher than in the more conventional pulverised fuel combustors [7].

The wear of the tubes submerged in the fluidised bed is caused by an interaction of erosion with corrosion [8]. However the wear mechanism has also been described as a process of three body microabrasion at tube temperatures up to 350°C, whereafter the wastage mechanism becomes oxide dominated [4,9].

In a pulverised fuel combustor, pulverised coal is ducted into the boiler and ignited. Heat transfer to the boiler tubes is by radiation from the coal flame and convection from the hot combustion gases. The by-products of the coal flame are coarse ash, fly ash and flue gases. The coarse ash particles fall out of the bottom of the boiler whilst the fly

ash is ducted out of the boiler, entrained in the flue gases. Erosion of boiler tubes in this environment is due to the impact of fly ash particles on the heat transfer surfaces.

The main differences in conditions between a fluidised bed combustor and a pulverised fuel combustor is particle velocity and mass loading. Particle velocities in fluidised beds are an order of magnitude lower than in pulverised fuel combustors, whilst the close packing of the particulate bed results in a higher particle mass loading on the boiler tubes. The wear mechanism of the tubes in pulverised fuel boiler combustor conditions has not been rigorously defined. There is thus a need to investigate high temperature erosive wear specifically for these conditions.

Solid particle erosive wear has received much attention in the scientific literature. The effect of variables such as particle type, size [10], shape [11], mass loading [12] and velocity [13] on erosive wear have been thoroughly investigated. The effect of temperature has also been examined [4]. However, the focus of erosion research at high temperatures has generally been concerned with the wear of boiler tube steels in fluidised bed combustors [4,14,15].

This work focuses on the erosion of boiler tubes by coal ash in pulverised fuel boiler combustors. The design of these boilers cause aerodynamic flow abnormalities. These result in localised regions of high particle velocity and mass loading compared with average values in the boiler duct. Severe erosive wear can occur in localised regions causing thinning of the tubes which, in the worst cases, result in tube leaks. In pulverised fuel plant and in particular dual pass boiler plant, the problem seems to be at its worst in the latter stages of the boiler duct when the fly ash particles harden as they cool and do not adhere to the tube surfaces, but rather transfer part of their kinetic energy to the tube material, causing erosive wear.

Tube leaks are difficult and time consuming repairs to effect which results in costly plant downtime. The economic benefits in effectively managing the problem of erosive wear of boiler tubes are thus obvious.

1.1 The aim of this research project

Although comprehensive studies on high temperature erosion have been undertaken for conditions of low particle velocity and high flux, the wear mechanism in regions of high localised velocities and low particle fluxes has yet to be methodically tested. This work is an attempt to simulate the process variables in the high temperature erosive conditions of boiler tubes in pulverised coal combustors by developing laboratory apparatus which allows a methodical means of identifying the critical variables involved in the wear mechanism. In this way, understanding of high temperature erosive wear in these conditions can be improved.

1.2 Research objectives

(1) To identify the process variables in pulverised coal combustors in South African power stations.

(2) To design and commission laboratory apparatus to simulate these conditions.

(3) To quantify the effect of process variables in order to gauge their relative importance in the overall wear phenomenon.

2. Erosive wear in coal fired electricity generation.

The relevance of this work pertains to a serious tribological problem experienced in pulverised fuel plant used by the local power utility to generate the majority of electricity in Southern Africa. The generation of electricity from coal utilises the thermal energy in the coal to heat steam to high temperature and pressure. The steam is then expanded through large turbines coupled to generators which convert the rotational energy from the turbines to electrical energy.

The process starts with the milling of the coal in ball mills, which is reduced to sub 100μm sized particles. After milling, the coal dust is mixed with warm air and ducted into the boiler. These boilers are physically very large; a boiler generating enough heat for the steam to run a 640MW turbine has a cross sectional area of about 13.7 X 13.7m and stands 63.0m high. Upon arrival in the boiler the air/coal dust mixture is ignited. The by-products of this exothermic reaction are coarse ash, fly ash and hot flue gases. The coarse ash drops out of the boiler whilst the fly ash is entrained in the flue gases and is ducted out causing erosive wear [16,17,18] of the heat exchanger tubes in its path. The configuration of a 640MW dual pass boiler is seen in Figure 2.1.

The coal that is burned in South African coal fired power stations is typically of a low calorific content and a high ash content ranging between 20 and 40% by mass of the coal [19]. The coals burned are also known to contain a high percentage by mass (15-40%) of quartz, a mineral thought to be largely responsible for the erosive wear that the fly ash causes [20].

Erosive wear of the steam carrying tubes can lead to tube failure which is costly in terms of material replacement and loss of production. Failure results when the boiler tube wall thickness decreases to a point when the hoop stress in the tube, due to the internal pressure from the steam, is sufficient to cause yielding of the reduced steel tube wall thickness followed by fracture.

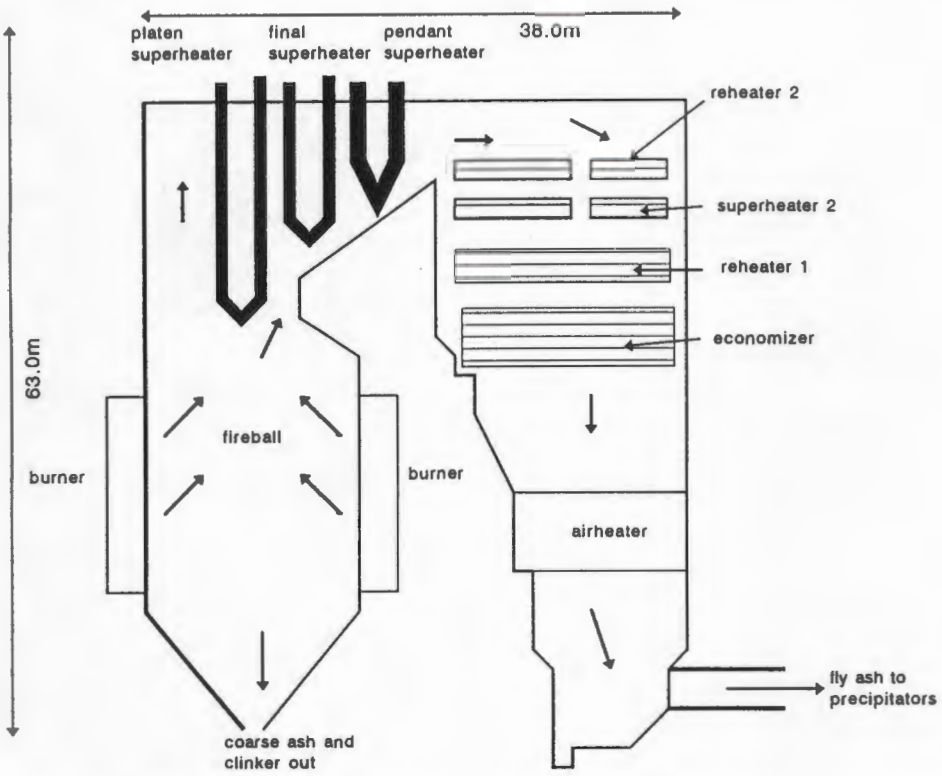

Figure 2.1: Diagram of a typical dual pass pulverised fuel boiler plant.

These failures have been termed a "middle aged" boiler ailment [18] i.e. general failures occurring from 50 000 hours of service onwards. However, premature tube failure can occur in regions of severe localised wear from as little as 10 000 hours (1 year) of service.

Although the failures can be the combined result of a number of factors such as

a) stress,
b) temperature,
c) oxidation/corrosion (gas side and steam side [21]),
d) erosion and
e) vibration [16].

Power plant engineers [16,17], as well as researchers [6], of industrial wear problems are of the opinion that ash impaction erosive wear is *the principal cause* of boiler tube failures in economiser, primary superheater and reheater groups of boiler tubes.

Rigorously defined, the problem of boiler tube erosion covers impaction of tubes by fly ash, falling slag, sootblowing and impact by unburned coal particles. However this work is concerned primarily with the impact of tubes by fly ash particles.

Clearly the particular conditions of power plant operation have a most important influence on any resultant erosive wear of the boiler tubes by coal ash. These factors of importance are closely examined in the following sections for both general and local power plant operation.

2.1 The magnitude of particle velocity in the boiler

Raask [6] suggests that the range of particle velocities in a pulverised fuel boiler combustor (PFBC) is generally between 8 and 22m.s^{-1}. However, for high ash, high quartz fuels, gas velocities are deliberately lowered to between 8 and 12m.s^{-1} . The assumption is made that the particles are at the same velocity as the combustion gases. Gibson [19] measured the variation of particle velocities across a boiler and found a range from 3 to 24m.s^{-1} using laser velocimetry from the right hand side to the left hand side of the back pass of a dual pass boiler (with the first pass on the left and the back pass on the right as depicted in Figure 2.1). Stringer [20] estimates particle velocities of up to 35 m.s^{-1} in localised areas of the boiler - and this is typically where regions of excessive erosive wear will be found. Upon examining boiler performance figures supplied by Stans [22], *average* gas velocities at the entrance to the first bank of tubes in a section vary from 8 to 11m.s^{-1} , which is within the minimum and maximum as quoted by Raask and Gibson.

2.2 Gas, particle and specimen temperatures

In addition to assuming that the gas velocity is the same as the particle velocity, the assumption is also made that the gas temperature is the same as the particle temperature in the boiler plant. Table 2.1 lists the ranges of *gas* and *tube* temperatures experienced in a pulverised fuel boiler combustor as well as the typical wear problem that is experienced at that particular location. Figure 2.2 shows *gas* temperatures at different locations in a dual pass boiler. The problem of excessive localised wear occurs in the latter part of the boiler where the particles and gases have cooled substantially which is shown in Table 2.1 and Figure 2.2.

Area	Range of gas temp. (°C)	Target surface temp. (°C)	Type of wear
Water walls	1200-1500	250-400	Slag deposits (clinker)
Radiant superheater	1000-1300	450-500	deposit build-up
Secondary superheater and reheater	800-1000	500-650	oxidation, deposit build-up
Primary superheater and reheater	550-800	400-450	erosion
Economiser	350-550	50-250	erosion
Airheater elements	100-350	50-300	some erosion

Table 2.1: A list of types and areas of wear with corresponding temperature regimes (after Raask [18]).

It can be seen from Table 2.1 that the temperature at which the fly ash entrained in the flue gas strikes the heat exchanger tubes varies between 500°C at the economiser, and 1200°C at the superheater. The temperature of the tubes in these regions are 250°C and 550°C respectively. It is postulated [18] that the higher the temperature of the ash / gas stream, the more the erosion propensity (i.e. the ability to inflict damage) of the ash depends on the corrosion resistance of the alloy it is striking.

Raask [18] also claims that at gas temperatures greater than 900°C, ash can form a deposit on a boiler tube. However, between 700 and 900°C, neither erosion nor excessive deposit build-up occurs. At gas temperatures less than 700°C fly ash starts to bounce off the tubes in its path as opposed to forming deposits i.e. it displays rebound as opposed to captive behaviour. Raask offers evidence from Taylor and Shell [23] who

state that for high temperature erosion studies the target temperature should be kept below 700°C in order to ensure that ash particle behaviour remains rebound as opposed to captive.

The economiser flue gas temperature is a maximum of 500°C. This temperature suggests that, in these conditions, ash particle behaviour is rebound as opposed to captive, which supports the claim that ash impaction wear is the principal cause of failure in the economiser section of a pulverised fuel boiler [16,17,18].

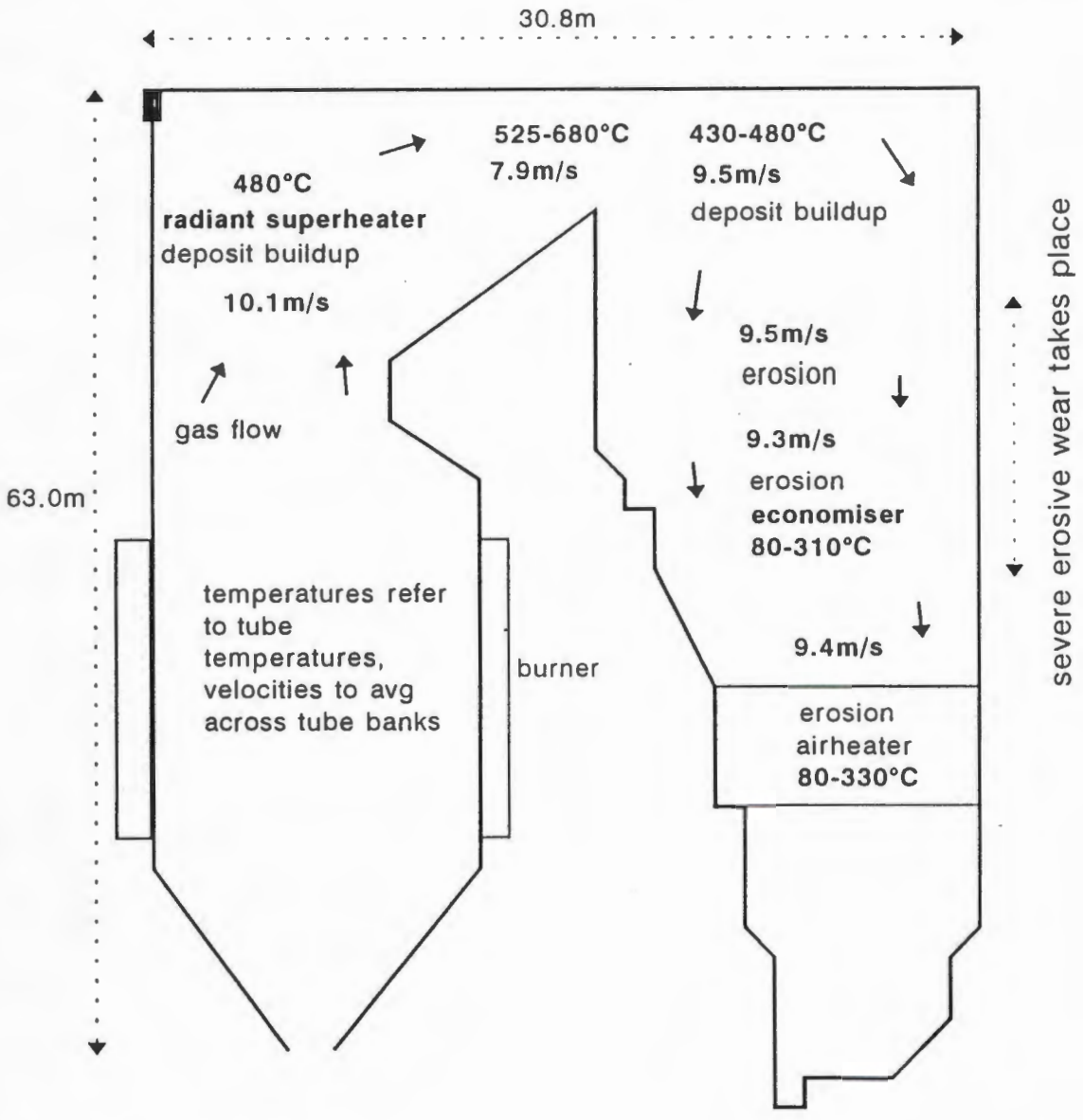

Figure 2.2 : Outline of a boiler supplying a 640 MW turbine, showing the gas temperature regimes in addition to the average gas velocities experienced in a typical dual pass boiler.

2.3 Erodent type and size

The by-products of the combustion of pulverised coal for the purposes of generating heat in a thermal power station are : coarse ash, fly ash, as well as the accompanying flue gases. The coarse ash consists of 10 to 20% of the total ash load and comprises of particles ranging in size between 0.075mm to as large as 500mm. The fly ash accounts for 80 to 90% of the total ash load and has a particle size range from 2 to 500μm [24]. The size distribution of fly ash from a South African plant is shown in Figure 2.3. Here it is seen how approximately 95% of the fly ash particles are smaller than 125μm in size. The size range of 63-106μm has a percentage bandwidth of 15.2% whilst the 106-125μm size range has a width of 4.5%.

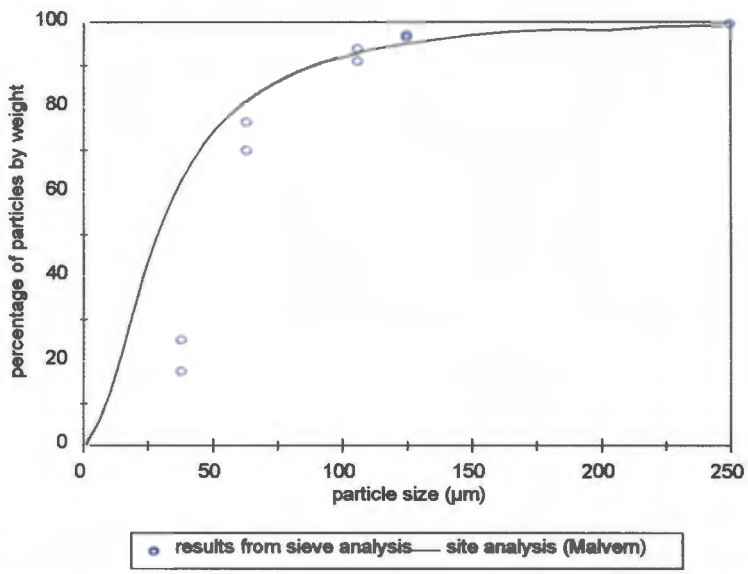

Figure 2.3 : Particle size distribution for fly ash from Hendrina power station, South Africa.

Fly ash is made up chiefly of oxides of silicon and aluminium, which are found in crystal form in quartz (SiO_2) and mullite ($3Al_2O_3.2SiO_2$). Although the chemistry of fly ash is relatively consistent, the mineralogy is less so. This is seen in Table 2.2 where the percentage occurrence of silicon as SiO_2 for different power stations ranges from 53.9 to 66.9%, whereas the range of quartz measured is 13.8 to 41.2%. This shows greater variability in the mineralogy, compared to the chemistry of the ash.

to 66.9%, whereas the range of quartz measured is 13.8 to 41.2%. This shows greater variability in the mineralogy, compared to the chemistry of the ash.

Power Station of ash origin	Silicon as SiO_2 %	Aluminium as Al_2O_3 %	Quartz (SiO_2) %	Mullite ($3Al_2O_3.2SiO_2$) %
Arnot	56.5	25.2	17.7	52.2
Duhva	56.7	29.1	17.1	59.2
Hendrina	56.2	27.8	41.2	39.0
Kendal	55.2	30.5	13.8	60.4
Lethabo	53.9	32.5	21.2	64.6
Matimba	66.9	20.6	18.0	49.1
Matla	55.0	27.6	14.7	36.7
Tutuka	57.1	25.4	28.2	44.2

Table 2.2 : Table listing major chemical and mineralogical constituents of fly ash from local boiler plants.

The smaller ash particles are spherical but as their size increases, their shapes become more and more irregular until they become amorphous agglomerations of spheres at a size of 100µm. This sequence of shape change from the sub 20µm particles to particles greater than 100µm can be seen in scanning electron micrographs of fly ash particles from a South African plant, shown in Figures 2.4,5 & 6.

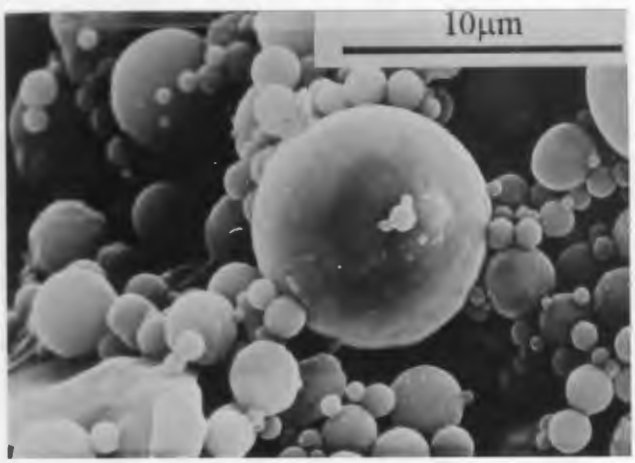

Figure 2.4 : Plant fly ash in the sub 20µm range showing how the particles are perfectly spherical and tend to attach themselves to one another (Lethabo power station).

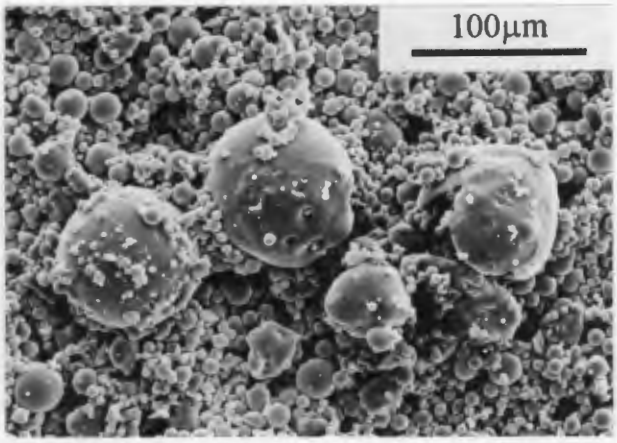

Figure 2.5 : Micrograph showing the sub 100μm size range of the smallest particles up to the largest spheres. The misshapen spheres are often hollow as can be seen by the sphere on the farthest right which has split open (Lethabo power station).

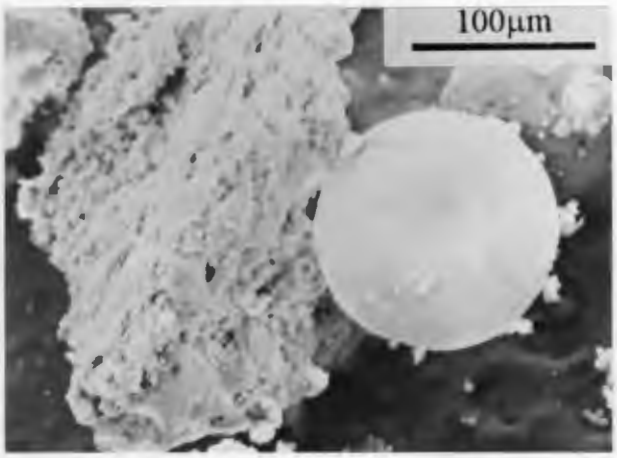

Figure 2.6 : Micrograph showing particles in a > 100μm size range. Here more irregular particles are seen in addition to spheres which are large particles of semi-combusted coal or char (Lethabo power station).

2.4 The mass flux or particle loading per unit area of the conveying gas

The effect of particle mass flux on the erosion of metallic materials at high temperatures is an interesting topic. It has been postulated by plant engineers [25] that changes in mass flux by orders of magnitude may influence the erosion mechanism itself with increasing temperature. Thus, the wear mechanism may change from being one of erosion dominant (high fluxes) to a corrosion/erosion mechanism (low fluxes) at high temperatures.

Mass flux has been defined as the mass flow rate of particles per unit area of specimen [26]. The area is determined by image analysis of the scar formed by the erodent particles impinging on a specimen normal to the gas stream. The units of flux are thus $kg.m^{-2}.s^{-1}$. Krishnamoorthy et al [5] controlled mass flux by changing the dimensions of the hopper gates on their erodent hopper. Thus it must be assumed that they measured mass flux in their gas blast erosion rig by dividing the mass flow rate of erodent into the gas stream (in this case air) by the cross sectional area of the ceramic nozzle of the apparatus.

To obtain similarity between apparatus and boiler conditions, mass flux was calculated as **$0.17kg.m^{-2}.s^{-1}$** using a method outlined in section 4.3. This calculated value of mass flux in a typical local boiler is less than the minimum outlined by Raask [18] in other commercial systems, but is within the same order of magnitude. It is however, the lowest flux of the ranges examined by workers dealing with erosive wear as seen in Table 2.3.

Researchers	Flux min $kg.m^{-2}.s^{-1}$	Flux max. $kg.m^{-2}.s^{-1}$
Raask [18]	0.3	0.6
Anand et al [12]	1	500
Krishnamoorthy et al [5]	3.33	33.3
Levy et al [27]	2.12	
Shipway & Hutchings [26]	0.4	47.6

Table 2.3 : The range of fluxes tested by other researchers.

An important point to stress is that the figure of $0.17kg.m^{-2}.s^{-1}$ is thought to be a minimum value of mass flux likely to be encountered in pulverised fuel boiler combustor conditions due to the known aerodynamic inconsistencies that exist within a boiler. It is postulated by Gibson [19] that "roping" of gas streams can occur within the boiler, which could result in changes in the average flux that has been derived, in addition to the fact that the boiler duct cross-sectional area is not constant. This may, as mentioned, have an effect on the magnitude of flux experienced by the heat transfer surfaces. Thus, in any experimental work the effect of a range of mass fluxes on erosion rate should be examined.

3. The effect of variables in the erosive wear of ductile materials

The review of the scientific literature is divided into two parts. In section 3.1 the critical environmental variables affecting erosive wear are discussed. These variables include the effect of particle velocity, type, size, flux and angle of impact on erosive wear. Specific attention is paid to erosion by coal ash particles as they are considerably more complex both structurally and morphologically than other particle types used in erosive wear studies.

In sections 3.2 to 3.5 the response of the target material to the impinging particles is examined. This includes the mechanisms of material removal at low and high temperatures and the effect of material properties such as ductility and microstructure on the erosion rate. An additional topic dealt with in section 3.6 is a review of the existing literature on the erosive wear behaviour of thermal sprayed metallic coatings. These coatings are commonly used to enhance the erosive wear performance of boiler tubes in coal fired power plants.

3.1 Impact parameters : A review of the literature pertaining to critical environmental variables in erosive wear

3.1.1 The effect of particle velocity and the nature of the particle and gas flow.

It is well documented that particle velocity is a major variable when considering erosive wear rates [10,13,28,29]. In the development of models for systems involving ductile materials (typically metals), erosion rates are generally considered to be proportional to the particle velocity raised to a power exceeding two. A small increase in velocity will thus result in a significant increase in the rate of material loss.

Although particle velocity is indeed an important consideration, the *nature* of the particle flow must also be considered. The difference in erosion rates between turbulent flow and laminar flow at similar particle velocities may be marked, according to Finnie [28]. This is an empirical result based on observations of components in service where erosive wear was caused by gas-borne particles. Components in known areas of turbulence were seen to wear at greater rates than those in regions where a smooth laminar flow was in evidence.

MacAdam and Stringer [30] performed tests in a fluidised bed where careful attention was paid to the distribution and severity of particle impacts on the surface of specimens. The results of these tests showed that approximately one quarter of all contacts were considered to be damaging. However, this was in a fluidised bed environment in which the damaging particles are partially constrained to the surface of the target by the closely packed particulate bed. This results in a low stress three body abrasive wear mechanism. The constraint is evidenced by the nature of the wear scars which show many particle direction changes.

It would therefore seem that great care must exercised in the interpretation of erosion test results conducted in fluidised beds compared with those from gas-borne particle erosion since the mechanism of material removal is different.

Tabakoff et al [31] performed a rigorous treatment of aerodynamic flow within their erosion windtunnel, using coal ash particles as the erodent. Their conclusions were interesting, not so much in terms of understanding the effects of velocity, flow and particle distribution on erosion rates, but rather how erodent particles behave differently within a fluid stream depending on their size and hence inertia.

Results of this testing showed that large numbers of particles, smaller than 30μm in diameter, were deflected away from the target as opposed to striking it. The deflection is caused by the flow of gas around the specimen entraining particles of low inertia into the flow path. However, more massive particles are not influenced to the same extent by the gas flow and are not deflected away from the target. There is thus a sharp fall in erosion rates when sub-30μm diameter particles are used as the erodent, as fewer particles strike

the surface. Furthermore, those particles that did strike the surface did so over a range of impact angles different from the angle of orientation of the specimen. This effect was more noticeable for specimen orientations less than 30°, as the gas flow appeared to be easily deflected below this angle.

Dosanjh et al [32] quantified particle inertia by defining a momentum equilibrium constant λ as :

$$\lambda = 2*\rho_p*d_p^{2}*u/(18*\mu*d)$$

where :

ρ_p	=	particle density
d_p	=	particle diameter
μ	=	fluid dynamic viscosity
u	=	gas jet velocity
d	=	nozzle diameter

Dosanjh et al [32] state that if $\lambda > 10$ then the particles in the gas stream do not follow the air stream lines. This means that the particles have enough aerodynamic penetration to strike the target rather than being deflected away from the specimen.

3.1.2 The effect of impacting particle shape, type and size

The effect of particle shape on erosion rates is reported to be significant. Using their gas blast apparatus, Levy and Chik [11] found that angular steel particles were up to four times more damaging to an AISI 1020 steel than spherical steel particles at the same velocity. Further studies [10], using spherical glass beads and angular silicon carbide (SiC) particles, showed an order of magnitude difference in material mass loss caused by the two erodents. At a particle velocity of 20m.s^{-1}, SiC particles caused 1.6mg of material loss compared to a loss of only 0.2mg when glass beads of a similar size (250-355µm) were employed.

This difference in behaviour was considered to be due to the sharp edges of the SiC cutting and displacing more material than the spherical glass beads. The spherical beads, with smooth surfaces, tend to deform and displace material across the steel surface. The more angular SiC particles result in greater cutting action which displaces material in the form of ridges and lips which are more easily removed by ensuing particle impacts.

It was also shown [11] that for a particle hardnesses greater than 700kg.mm^{-2} , erosion rates are constant regardless of particle type. This conclusion is based on tests comparing erosion rates obtained using silicon carbide, silica sand (SiO_2) and alumina particles (Al_2O_3) at 20m.s^{-1} on an AISI 1020 steel. This result differs from that of Palasamudram and Bahadur [33] who found that in a fluidised bed environment at 500°C, the erosion rate increased with an increase in particle angularity. The angular SiC particles used in these tests caused up to 4.5 times more wear than the similarly sized but more rounded SiO_2 particles.

The effect of particle size on erosion rates is an intriguing problem in gas blast apparatus. It appears that erosion rates not only depend on the kinetic energy of the impacting particles but also whether or not they will be deflected away from the target. As discussed in section 3.1.1, if the mass of the impacting particle is sufficiently low, it will follow the gas flow around the target surface and be deflected away as opposed to striking it. This is an opinion shared by Raask [18] and Tabakoff et al [31]. The cut off figure, below which damage to the target is negligible, varies depending on the experimental conditions employed, but the lowest particle size quoted is 30μm above which little deflection occurs.

Hutchings [34] concludes that for a particle size above 100μm, erosion rates are independent of size for ductile materials from results obtained using gas blast apparatus. There is an increase in erosion rate with particle size for a similar mass flux, until a particle size of 100μm is reached whereafter size is unimportant. This phenomena is well illustrated in Raask [18], where summarised results of other researchers show that for the erosion of ductile materials, a plateau is reached in erosion rates for a particle size of 100μm, when erosion rate is graphed against particle

size for a fixed mass flux of particles. However, Liebhard and Levy [10], also using a gas blast apparatus, showed that a plateau in wear rates is reached at 300μm when *spherical* particles are used whereafter rates decline with further size increases. With *angular* SiC particles, a plateau in wear rates was reached, but only at a particle size of 200μm.

3.1.3 Fly ash as an erodent

Fly ash as an erodent deserves particular attention due to its complex constitution and morphology in addition to the variation in its properties with size.

Fly ash particles are formed by the combustion of coal particles. The organic matter in the coal is burnt off releasing heat; a fundamental upon which the generation of electricity from coal is based. The release of this heat changes the nature of the mineral species in coal. These mineral species are chiefly mullite ($3Al_2O_3.2SiO_2$) and quartz (SiO_2).

The alumino-silicates in the coal are vitrified and converted into a glassy phase. The vitrification results in spheroidisation of the molten particles due to the surface tension of the liquid. The temperature of combustion which causes vitrification of the alumino-silicates is in the region of 1600°C. Thus, pulverised coal ashes consist mainly of spherical particles of low hardness, typically 600kg.mm^{-2} on average.

However, a temperature of 1600°C causes only partial vitrification of the quartz particles and approximately 50% of the quartz in the coal, as measured by x-ray diffraction, survives combustion [35]. It is believed that these quartz particles, which have a high hardness of approximately 1300kg.mm^{-2} are responsible for the damage caused by the impaction of fly ash on heat transfer surfaces. It has also been postulated that in the absence of mineralogical data, that a relationship exists between the chemical composition of the ash and its mineralogy [18]. Bosch [35] partly agrees with this view, but states that such a relationship is boiler specific. Thus, a general

formula cannot be used to apply to different pulverised fuel boilers burning different coals.

In addition to a variation in mineralogy in any one fly ash particle, mineralogy appears to change as a function of particle size. Bosch [35], compared the mineralogies of ashes of different sizes from the same boiler plant and noted that the quartz content of the coal ash particles decreased with a decrease in particle size. This is a significant result as it encourages finer milling of the coal which increases the coal particle surface area, raising the combustion temperature and in doing so increasing the vitrification of the quartz present in the coal. This in turn could result in a decrease in erosion wear rates, since quartz is believed to be the mineral in coal ash responsible for wear damage.

The shape of the coal ash particles also varies. For particles in the 2-80μm range, the shape is spheroidal [36]. However for sizes larger than this, the shapes diversify. This is detailed by Lauf [37] who quotes seven possible different shape and structure properties with which to classify coal ash particles. Lesch and Cornell [36] however, show only four possible particle groups :

a) Solid spheres
b) Hollow spheres (cenospheres)
c) Spheres filled with smaller spheres (plerospheres)
d) Sphere aggregates and sphere encapsulated mineral phases

Lesch and Cornell, however, do not mention the angular semi-combusted coal particles which can also be seen when examining a specimen of coal ash. Due to the short time spent in the boiler, some of the larger coal particles do not have time to fully combust and the ash is left with a coke content which is evident as a porous and non-spherical mass.

3.1.4 The effect of the particle mass flux i.e. particle loading per unit area of conveying fluid.

Much of the literature on the effect of particle mass flux on erosion has been conducted at room temperature [5,12,26], little having been reported on the effects of mass flux at high temperature. It is agreed though, that an increase in particle flux at room temperature results in a decrease in erosion rates.

Shipway and Hutchings [26] quote significant effects of particle flux on erosion that have previously been attributed to the phenomenon of target shielding. Shielding occurs when particles rebounding off the target collide with incoming particles thereby reducing the energy level at which the incoming particles strike the specimen surface. Previous work by Shipway and Hutchings [38] using low fluxes, shows the scar radius caused by particles impacting on a specimen at 90° to increase linearly with the logarithm of the mass of erodent used.

Based on the later experimental results [26], using lead glass spheres in the size range of 212-250μm, a particle flux greater than 0.76kg.m^{-2}.s^{-1} results in the particle scar radius to diverge from the linear relationship mentioned. This is attributed to the transition from particle-particle interactions having a negligible effect to becoming more significant. However, for the smaller 63-75μm particles, there appeared to be negligible differences between the fluxes tested which ranged from 0.4kg.m^{-2}.s^{-1} to 47.6kg.m^{-2}.s^{-1}. It was thus concluded that the probability of particle - particle interactions for the smaller particles is minute.

Anand et al [12] as well as Krishnamoorthy et al [5] agree that particle mass flux is an important factor in erosion testing and can affect results due to shielding of the target surface. Both groups of workers examined the effect of particle mass flux on the *erosion rates* of various materials. Anand et al found that erosion rates decreased with an increase in flux from 0.1 to 300kg.m^{-2}.s^{-1} when using 270μm Al_2O_3 particles, whereafter erosion rates remained constant. However when 63μm Al_2O_3 particles were employed, erosion rates were constant for a flux of over 300kg.m^{-2}.s^{-1} . Krishnamoorthy et al only

used 215μm sized SiO_2 particles. They too observed a decrease in erosion rates with an increase in particle flux over the range of 3.33 to 33.3kg.m^{-2}.s^{-1} .

Liebhard and Levy [10] sum their findings, as well as other workers by stating that for a given shape or type of erodent particle, the erosion rate is affected by :

a) the particle size,
b) the number of particles striking the surface per unit time (i.e. flux),
c) the particle kinetic energy i.e. velocity and
d) interference between striking and rebounding particles.

3.1.5 The effect of particle angle of impact on erosive wear

It is accepted, within the field of erosion wear testing that for flat plate specimens maximum wear rates occur at acute angles for ductile materials and normal for brittle materials [39,40,41]. The angle of the specimen relative to the approaching gas and particle mix does not necessarily imply that all of the particles in the gas stream will strike the surface of the material at this angle. Certainly, in conditions of turbulent flow, the motion of the particles will be made up of random orientations within a band of angles. It is thus more accurate to say that maximum wear will occur when the specimen is orientated at an acute angle relative to the particle flow, resulting in a greater probability of particles striking the surface at low angles of impact. This is backed up by the observations of Levy et al [42] who found that the basic mechanism of erosion does not change with impingement angle.

The effect of particle type on the angle of maximum wear in ductile materials is dealt with by Sundararajan [43]. In this work it is postulated that the frictional forces between the impacting particles and the surface introduces a high shear force which promotes lip formation ultimately leading to material loss. Results showed that for angular particles, maximum wear took place in the range of 13° to 22°, whilst for spherical particles the maximum wear rate was shown to occur between 40° and 45°. The conclusion is reached that the impact angle corresponding to peak wear rate is dependent on the coefficient of friction μ between the particle and the target surface,

which in turn depends on the particle shape. Increasing μ results in peak wear rates occurring at lower impact angles since there will be a greater drag force opposing the cutting and ploughing action of the impacting particles. This infers that more energy is transferred to the target, resulting in more extensive crater lip formation, ultimately leading to greater material loss.

3.2 A review of the response of the target to low and high temperature erosive wear

3.2.1 Mechanisms of material removal at low temperatures

Early detailed research in erosive wear phenomena defined the mechanism of material removal in ductile materials as being one of a cutting action at low angles of specimen incidence and one of deformation at high or normal angles of incidence [6,44,45]. Tilly [46] also suggested a two stage mechanism of material removal :

- Particles strike the surface of the material and make indents, possibly removing chips of material.
- The particles fragment after impact and then cause secondary damage.

Recent thinking on material loss mechanisms suggests that the volume of material displaced by a cut is not necessarily removed at once, but is lost in a series of repeated impacts. Levy [47] and Levy et al [48] postulated the "platelet" mechanism of material removal which is a combined extrusion - forging mechanism. The extruding action of an impacting particle on a target displaces material to form lips which stand proud of the surface. The forging action of the following particles flattens these lips, causing strain build-up. The strain build-up eventually leads to fracture of the material connecting the lips to the crater sides and the lips, or parts of the lips, are thus removed. This micro-mechanism shows the validity of examining the mechanical properties of a material such as work hardening ability in order to determine a material's suitability for application in an erosive environment [49].

3.2.2 Mechanisms of material removal at high temperatures : Conflicting opinions in the literature

There is a generally held view amongst researchers investigating erosion in fluidised bed boilers that material wastage of steel initially increases with rising temperature and then falls again. This peak in wastage rate with temperature varies as a function of particle velocity and size as well as the corrosion resistance of the target material [8,50,51]. Fluidised bed conditions of high temperature and low particle velocities is simulated in the laboratory by rotating specimens through fluidised bed furnaces.

The extent to which this peak predominates can be seen in Figures 3.1 and 3.2. Figure 3.1, which shows erosion rate as a function of temperature, exhibits a peak in wastage for AISI 304 stainless steel (eroded by 1mm alumina particles at a velocity of $2.7m.s^{-1}$), at a temperature of approximately 800°C. Erosion rates obtained for a carbon steel also eroded by 1mm alumina particles at $2.7m.s^{-1}$ and $4.3m.s^{-1}$ are included in Figure 3.1. There is a peak in erosion rates for the carbon steel at approximately 480°C, but it is not as marked as the peak seen for the AISI 304 steel with the same particle velocity of $2.7m.s^{-1}$. At the higher particle velocity of $4.3m.s^{-1}$ however, a definite peak is evident at a temperature of approximately 550°C. Although the peak in wastage of the AISI 304 steel is higher than the carbon steel, it occurs at a higher temperature. Thus it can be stated, based on the evidence shown in the figures, that the peak in wastage moves to higher temperatures with increasing alloy oxidation resistance [8].

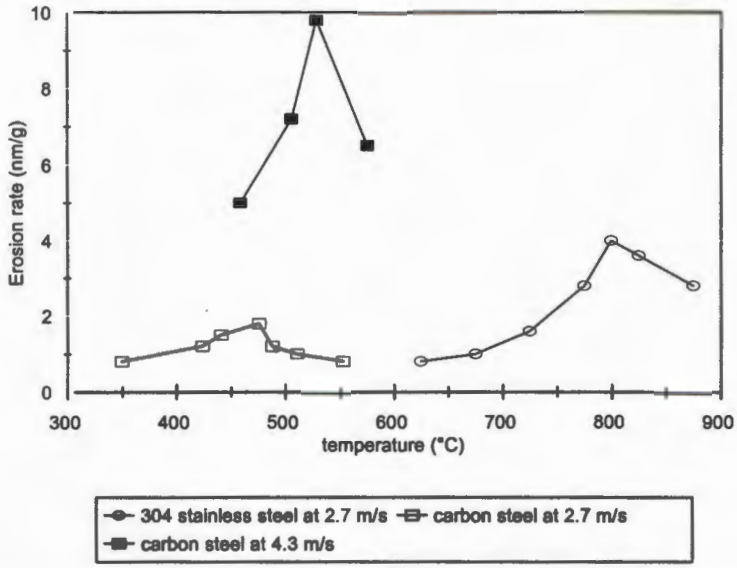

Figure 3.1: Wastage vs temperature for an AISI 304 stainless steel and a carbon steel noting the position and magnitude of the peaks in wastage for both materials [8].

Ninham et al [51] show results of erosion testing in the FB situation which also indicate a peak in material wastage with increasing temperature, the position and magnitude depending on the alloy composition. Figure 3.2 shows the results of erosion testing of an AISI 347 austenitic stainless steel and a bright mild steel at particle velocities of 1.7 and 2.5m/s, using 170μm alumina particles

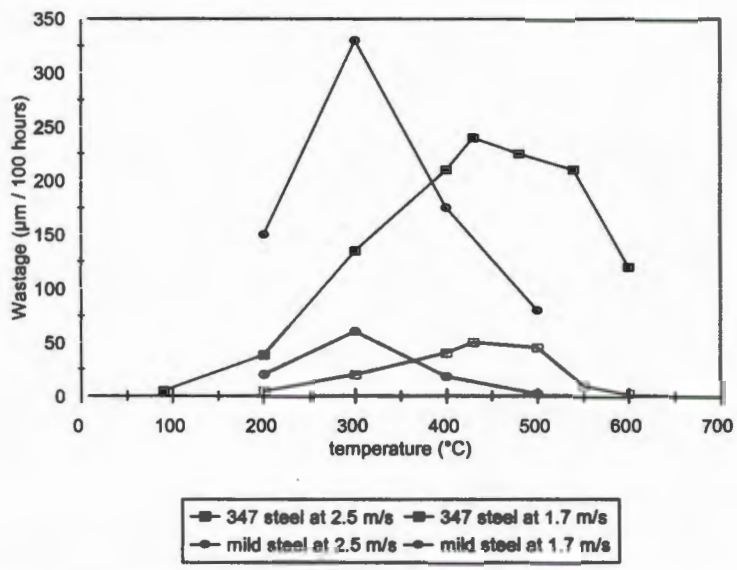

Figure 3.2 : Wastage vs temperature for two different steels whose peak wastages occur at the same temperature regardless of particle impact velocity [51].

It can be seen in Figure 3.2 that the peaks in wastage for the AISI 347 austenitic stainless steel tested at various velocities remain at the same position i.e. about 480°C. A similar phenomena is observed for the bright mild steel, which has a higher wastage peak at a lower temperature of approximately 300°C. Ninham et al [51] suggest that this peak can be understood in terms of the competition between increasing oxidation with temperature, and increasing oxide layer plasticity as the material temperature is raised. As the temperature increases, the oxide layer growth rate also increases. This brittle oxide layer also becomes more ductile with increasing temperature and is thus able to resist impacting particles without fracturing and spalling.

Wang et al [52] eroded a 1018 steel and found, similarly to Stack et al [8] and Ninham et al that metal wastage decreased upon the formation of an adherent oxide layer. Stack et al base their understanding of the peak phenomenon observed in their high temperature fluidised beds on a transition from erosion dominated (1) to corrosion dominated (2) behaviour. Corrosion dominated behaviour occurs when any material loss takes place primarily through the removal of corrosion products (oxide) by impacting particles as opposed to the general erosive damage of the bulk of material and the subsequent material removal. This is illustrated in the Figure 3.3 which positions these regimes on a simulated peak.

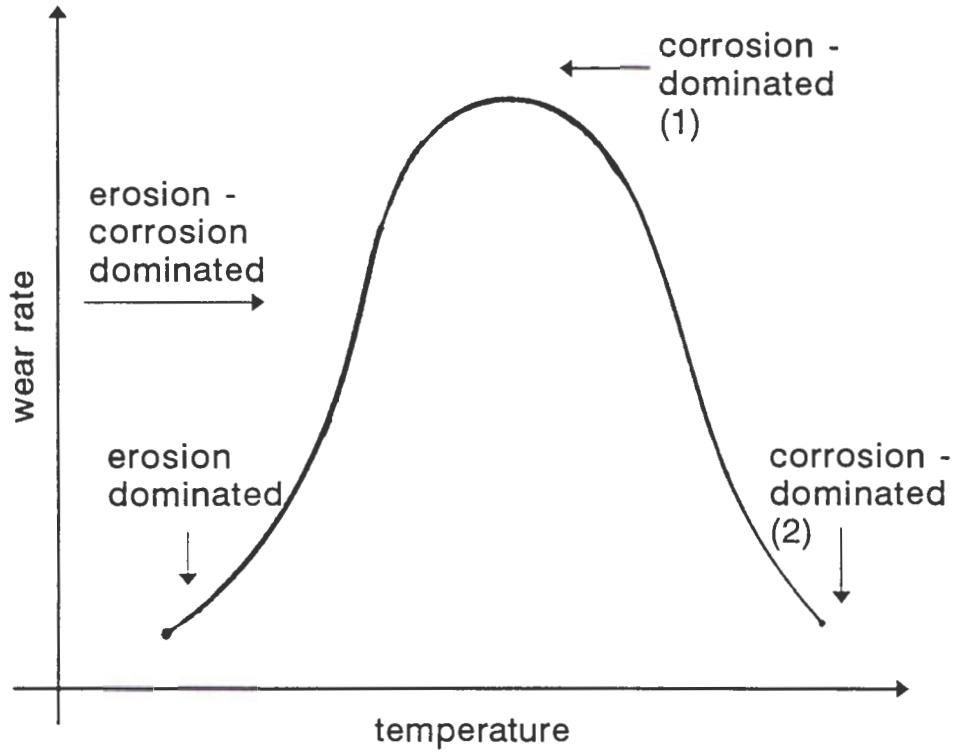

Figure 3.3 : Positioning of the regimes of erosion dominated behaviour and the transition to corrosion dominated behaviour [8].

There is evidence to suggest that in a high temperature erosive wear situation that the formation of an oxide layer will not protect the target material. This is well summarised by Kang et al [53] who state that at high temperatures and low velocities, material life is governed by oxidation and at high velocity by erosion. The differentiation between these regimes is dealt with more thoroughly in section 3.2.4.

MacAdam and Stringer [4] suggest from results of testing a 1018 steel in a fluidised bed, that it is rather a combined protective effect of the erosive particle deposit on to the oxide layer to form a duplex coating that offers the material protection. In these tests, the cylindrical specimen rod was pulsed downward 10mm and then drawn slowly up at frequencies of 0.25 to 2.5Hz, through a bed of 800µm quartz particles.

Olsson et al [54], from erosion tests on a 2¼Cr 1Mo steel using a gas blast apparatus and 180-360µm alumina particles at low particle velocities of between 2.6 and 8.2m/s, agree that the oxide layer is not likely to give adequate protection, as the erosive particles are very much harder than the steel or the oxide. Furthermore, differences in

the thermal expansion coefficients between the oxide layer and the substrate raises the stress at the oxide / substrate interface, promoting spalling.

Thus, material removal processes at high temperature and high velocities can certainly be oxide assisted but not oxide dominated. In tests conducted without any erosion effects, Cathcart & Pawel [55] considered the effect of sample geometry on material wastage by oxide scale loss. They observed the mechanical behaviour of oxide scales on tubes and noted that since the oxide surrounds the tube entirely, that it cannot grow without accumulating strain. The outer surface will be in tension and the inner in compression which leads to strain build-up resulting in scale fracture followed by scale loss. Even earlier work by Dils & Follansbee [56] on nickel based alloys proposed that strain build-up at the oxide layer / metal interface leads to oxide fracture and subsequent material loss. The resulting strain at the interface is equal to :

$$(\alpha_m - \alpha_o)*(T_1 - T_2)$$

where α_m = coefficient of expansion of the metal

α_o = coefficient of expansion of the oxide layer

T_1 = temperature of the metal

T_2 = temperature of the oxide layer

This is similar to Stephenson & Nicholls' concept of high temperature erosion being considered as material removal from a composite i.e. a ductile substrate and a brittle oxide [57].

The resultant strain at the interface leads to the oxide layer cracking and buckling. The mismatch is not just limited to the oxide layer / parent material, but can extend to materials where a duplex oxide layer develops. In this situation, mismatch between the first oxide layer and parent material as well as between the first and second oxide layers causes fracture of these layers leading to scale loss.

Maasberg and Levy [58] also found that the oxide layer was removed in a brittle fashion by a system of sequential cracking during erosion testing of pre-oxidised AISI 310

stainless steel and an experimental Fe-18Cr-5Al-1Hf alloy. This echoed earlier work [59] which also suggested an oxide loss mechanism of lateral cracking followed by scale exfoliation.

Stephenson & Nicholls [57] state when low energy particles (i.e. low velocity) are considered, scale fracture will not occur and in this case material recession rates will be determined by oxide layer loss through spalling [52,53,56]. Thus a material's response to high temperature erosion, listed in order of decreasing particle kinetic energy can be :

- substrate dominated,
- oxide modified,
- oxide dominated.

This is a similar opinion to Wright et al [60] who also suggest that the time between successive particle impacts should be examined to gauge oxide layer growth.

3.2.3 Time between successive particle impact :

The time between successive particle impacts on a material surface at high temperature is an important analysis to perform as it allows a calculation to be made of how thick an oxide layer can grow in that period. Clearly the flux magnitude will determine this time interval.

However Shipway and Hutchings [26] state that only rarely does the erosion rate of a material itself depend on particle flux, except when significant oxidative wear takes place between particle impacts. Instead, the variation of erosion rate with particle flux is largely due to particle-particle interactions. Private communication with Stack [61] supplements this opinion by stating that a peak in wear rate for a structural steel with temperature would probably not be seen in conditions of high velocity and flux.

3.2.4 Differentiating between the different erosion regimes

In the literature reviewed thus far, particularly in section 3.2.1 many comments have been made referering to high temperature erosion research being conducted using a fluidised bed arrangement. A typical fluidised bed rig is seen in Figure 3.4. Specimens are attached to a rotating shaft to simulate the erosive and corrosive conditions that typically exist within a fluidised bed boiler.

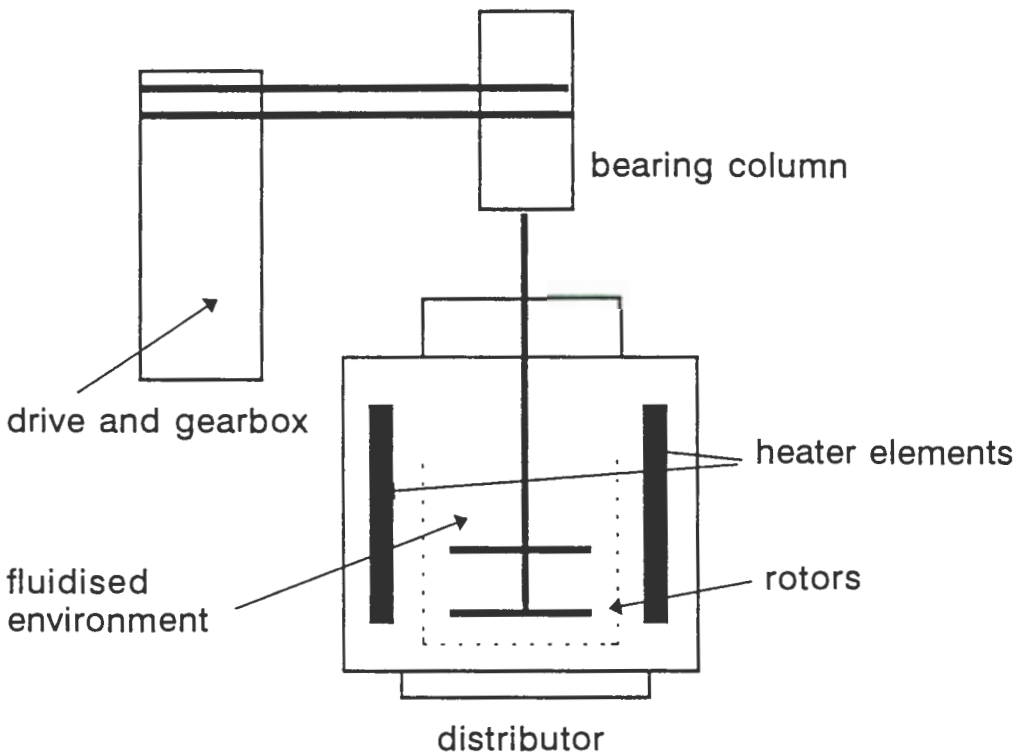

Figure 3.4 : A typical fluidised bed apparatus as used by Ninham et al [51].

There are many advantages of using a fluidised bed furnace when investigating high temperature material wastage due to erosive / corrosive wear.

- A steady temperature can be maintained.
- Cylindrical specimens, simulating boiler tubes can be completely immersed in the erosive environment.
- There is a variation in velocity as a function of the radius of the rotating arm allowing much data to be gathered in a single run.
- Long term tests are easily conducted.

The problem when examining results of high temperature erosive wear testing using fluidised bed apparatus and comparing these with high temperature erosive wear test results using a gas blast apparatus is that of differing particle velocities. Typical velocities used by experimenters in the fluidised bed field range from 1.5 to 5.0m.s^{-1} [50,51]. Particle velocities in air blast apparatus on the other hand span a range from 30m.s^{-1} [42] to as high as 305m.s^{-1} [62]. The difference in kinetic energies of similar sized particles in the two system types thus range from 2 to 3 orders of magnitude.

The issue of the applicability of fluidised bed data to gas blast apparatus data raises the point of differentiating between the different wear regimes. There is little doubt that parallels between the wear mechanisms occurring in the two different systems can be made but the extent to which mechanism influences material loss also has to be considered.

At low temperatures (<200°C) there is no doubt that pure erosion is the dominant mechanism of material removal in gas blast as well as fluidised bed apparatus [51]. However, when the temperature rises, the role of the oxide skin on the target becomes an issue. Stack et al [63] as well as Stephenson and Nicholls [57] categorise the degradation of materials in the fluidised bed erosive / corrosive environment as shown.

Stack et al [63]	**Stephenson & Nicholls [57]**	**Temperature range (°C)**
erosion dominated	substrate dominated	20 - 350
ero. - corr. dominated	oxide modified	350 - 480
corrosion dominated 1	oxide dominated	480 - 550
corrosion dominated 2		550 upwards

Both groups of authors agree that at high particle velocities material degradation at high temperatures is probably erosion dominated. For low energy particles, "scale fracture does not occur and therefore metal recession rates are determined by oxidation only" [57]. Hence the erosion mechanism in gas blast apparatus is likely to be erosion dominated as the particles have a high kinetic energy.

Another factor to consider is that the action of the erosive particles in the gas flow in gas blast apparatus is somewhat different to the erosive particles suspended 'fluid like' in fluidised beds. The flux of erosive particles in a gas blast apparatus is much lower per unit area than fluidised beds. Thus there are likely to be more particle strikes in a fluidised bed environment, coupled with an observed tendency for the particles to abrade the surface [4] as opposed to impacting and rebounding. Thus, the two situations can be catergorised as follows :

High temperature erosion gas blast apparatus	**High temperature erosion fluidised bed apparatus**
low particle flux	high particle flux
high velocities	low velocities
erosion dominated across the range of temperatures	erosion dominated moving to erosion - corrosion to pure corrosion

3.3 Material ductility as related to erosive wear

Tilly [64] suggested that a decrease in material ductility and an increase in strength and hardness, would result in an increase in erosion resistance for the ductile erosion case. Foley and Levy [65] have the reverse opinion and note that for a material to have high erosion resistance it needs to absorb the kinetic energy transferred to it by the impacting particles. Thus, the erosion resistance of materials increases with the increased ability to absorb strain energy.

Levy et al [42] also found that an increase in erosion rate with temperature is directly related to a decrease in the tensile strength of the material concerned. Their erosion tests were performed over a range of temperatures using nitrogen as the carrier gas to

avoid oxidation on the surface of the material. This was done to keep the mechanism of material loss solely to one of erosion.

Wang et al [52], using an experimental set-up which allowed cooling of the specimen whilst a hot gas was impinging on it, found that reduced metal wastage occurred when the amount of cooling through the specimen was reduced. They believed that the increased temperature lead to an increase in material ductility, reducing the erodent particles' individual ability to concentrate force at the point of impact. Conversely, increased metal wastage resulted when more cooling was employed since the lower temperature results in a surface with less ductility.

These results and opinions [42,52,65] concur with those of Kane and Torebelli [66], who state that it is often not a lack of high temperature corrosion resistance that causes excessive material loss at high temperature, but a loss of strength at temperatures of 650°C and higher. Cr, Ni and Mo steels containing 12 -25% Cr and 5 - 25% Ni are thus frequently specified for use up to 1150°C. Their austenitic structure and higher Ni content offer improved high temperature strength. In addition, they do not lose toughness with extended exposure to high temperatures as do ferritic Cr - Mo steels with 12% Cr.

Ball [49] examined the issue of material ductility in a more holistic fashion. If two different materials have the same yield strength and similar ultimate tensile strength (UTS), the more ductile material will not necessarily be the more erosion resistant. A particle strike causing a stress equal to or greater than the UTS will cause strain to fracture in both materials. Rather what is needed is a material with a good rate of work hardening and high UTS, resulting in the area under the stress-strain curve being high which means that the material's work to fracture is also high. This theory is backed up by results of testing with metastable austenitic stainless steels which have moderate yield strengths but high work hardening capacities corresponding to good wear resistance.

3.4 Material microstructure as related to wear

Levy [67] investigated the effect of microstructure on erosive wear by using two ductile steels and preparing them to form three different microstructures each as listed :

a) Coarse pearlite
b) Fine pearlite
c) Spheroidised carbides.

It was found that the mechanism of material removal changed with a change in microstructure.

- Coarse pearlite and fine pearlite : The material was removed from the surface in the form of chips which had cracked away from the brittle cementite lamellae.
- Spheroidised forms : The material was deformed plastically and less material was removed from the surface.

It was noticed that the spheroidised steel eroded at a lower rate despite having a lower strength. However, it did have twice the elongation to failure compared to the pearlitic steels. Thus, the conclusion was that the erosion rate is directly linked to the distribution of soft ductile phases and, within limits, the more continuous the ductile matrix, the lower the erosion rate. However, a balance between strength and ductility must be achieved because if the increase in ductility causes too great a drop in strength, erosion rates will increase.

Zum Gahr [68] suggests that the presence of second phases, such as carbides in steel, are detrimental to wear resistance. This should be seen in the light of Levy's [67] comment that erosion rates are indeed higher when the lamellar carbides are closely bordered by ferrite in the pearlite grains, whereas erosion rates decrease when the ductile phase is more contiguous.

These findings were confirmed by Wang et al [52] when using a 1018 steel in the annealed, normalised, cold drawn and as-quenched conditions. The homogeneity of the microstructure has a bearing on the erosion rate, with the lowest rate shown to be

the as-quenched 1018 which has a fine distribution of martensite and a little ductile ferrite.

In later work, in an attempt to achieve improved wear resistance by using a method other than precipitation hardening, strain hardening or martensite hardening, Levy et al [69] tried solid solution strengthening in eight different alloys. Iron and copper bases were used with varying amounts of aluminium and molybdenum in the case of the iron, whilst aluminium and titanium were used in the case of the copper. They found that there was either no improvement or a decrease in wear resistance with an increase in strength of the solid solution strengthened alloys. It was suspected that the improved strength of the alloys came at the expense of decreased ductility which caused either no improvement or a deterioration in wear resistance.

If the added effect of high temperature in the experimental matrix is considered, the situation becomes more complex. Wang et al [52] tested steels in the :

- annealed,
- hot rolled,
- normalised,
- quenched - tempered and
- cold rolled conditions.

Tests were conducted over a range of temperatures from 20°C to 650°C at a particle velocity of $20 m.s^{-1}$. It was found that wastage at the high temperatures is an involved chemical / mechanical interaction process. When erosion is the dominant material removal mechanism the microstructure with the best balance of ductility and strength showed the best erosion resistance. However, when scale removal was the dominant loss mechanism, the formation and morphology of the oxide layer was a primary consideration.

3.5 The effect of localised melting following particle impact

As the temperature of the specimen increases, its mechanical properties change, which could, in part, explain increases in erosive wear rates seen with increases in temperature.

An additional consideration in the explanation of increasing wear rates with temperature is that of localised melting. The impact of a particle will cause a localised temperature rise which, when added to the temperature of experimentation may approach the melting temperature of the target material. This could result in the wear mechanism changing from one of extensive plastic deformation to one of deformation assisted by localised melting.

Both Hutchings and Levy [70] and Doyle and Ball [71], established the likelihood of localised melting occurring during particle impact. Both approaches used a simple heat diffusion model to calculate whether there is a significant enough temperature rise due to successive particle impacts to cause localised melting which has a direct bearing on the material removal mechanism.

Doyle and Ball examined three cases of different materials eroded by 106-125μm SiC particles at a particle impact velocity of $40m.s^{-1}$. The materials used were alumina, ultrahigh molecular weight polyethylene (UHMWPE) and a grade 1030 carbon steel.

It was found that a rise in surface temperature following particle impact of the alumina surface was limited by an absence of adiabatic conditions. Thus, temperature rises are not significant but are still of sufficient magnitude to cause a more plastic response to impact and increasing the erosion rate.

UHMWPE has a low thermal diffusivity which results in entirely adiabatic conditions However, an important component in this analysis is the hardness of the material which is its effective resistance to indentation. Since this resistence to indentation is low for the UHMWPE, only small temperature rises can be expected since the energy is expended over large volumes of material.

The properties of the steel result in near adiabatic conditions and temperature rises of up to 500K could be experienced. Thus, changes in erosion conditions, such as the velocity,

size and time between successive erodent particle impacts, could result in changes in the thermomechanical effects experienced, which in turn could affect erosion rates.

3.6 Variables in electric arc sprayed thermal coatings

Thermal spray coatings can be applied in industrial situations to enhance the corrosion resistance of a low alloy substrate in high temperature corrosive conditions. Chrome and nickel containing powders are often used for this purpose, since they are able to develop tough and thick oxide layers.

Electric arc spraying of coatings is a practical and inexpensive method of depositing molten metal droplets on the bulk material surface to form an adherent layer. The bulk material surface is roughened before the application of a coating by blasting it with steel shot. The metal powders are contained in separate wires which are melted by striking an electric arc between them. The molten droplets of powder are blasted on to the substrate at velocities which range between 100 and 240m.s^{-1}. There is no alloying action between the deposited layer and the substrate. Rather the bond is a mechanical one and relies on the kinetic energy of the impacting molten metal particles to embed themselves in the roughened substrate.

In addition to providing corrosion resistance, thermal sprayed coatings are used in situations where high temperature erosion is a serious problem. Coatings are applied as sacrificial layers to prolong the time between complete component replacement due to excessive wear. This has obvious economic benefits.

This section provides a broad overview of the variables which influence coating wear. However, no extensive erosion tests have been carried out on electric arc sprayed coatings, despite this being a widely used method of applying thermal coatings in industrial wear situations. The literature covers wear tests on plasma, detonation gun, chemical vapour and physical vapour deposition. Results from erosion tests using

these methods are outlined as it is thought that similarities exist between the effects of test variables on these and the electric arc sprayed coatings.

3.6.1 The effect of hardness on the wear of coatings

Davis et al [72], eroded air plasma sprayed zirconia based ceramic thermal barrier coatings with 63-106μm SiO_2 particles at $30m.s^{-1}$ and showed an increase in erosion rates with a decrease in coating hardness. They did, however, state that hardness is not a dominating factor, but rather that the apparent porosity of the coatings has a greater influence on erosion rates.

Hogmark & Hedenqvist [73] found that increasing erosion rates can be related to decreasing coating hardness. They examined the tribological behaviour of thin hard physical vapour deposited (PVD) coatings such as a titanium-nitride (TiN) and chemical vapour deposited (CVD) coatings e.g. alumina.

Although hardness is an important facet of coating characterisation, it is not sufficient to consider hardness alone when performing a tribological characterisation of coated parts [74]. Indeed, Chiu and Liou [75] state that the resistance of a coated surface to impact damage depends not only on coating hardness but also on toughness and microstructure.

They compared theoretical predictions from thin plate elastic foundation theory to experimental results from SiC coated graphite and other layered specimens. This was to model the behaviour of thin brittle coatings. They showed that the critical energy to initiate damage on their glass slide models decreased with an increase in the elastic modulus of the substrate. The substrates tested were graphite, alumina and glass. They also found that the critical energy required to initiate damage in the SiC coating increased with increased SiC coating thickness.

Thus, it can be seen that hardness is an important consideration when examining the resistance of coatings to wear, but it cannot be examined in isolation when ranking coatings in order of their wear resistance.

3.6.2 The effect of thickness on the wear of coatings

Hogmark & Hedenqvist [73] also noticed that an increase in coating thickness increased wear rates which is illustrated in Figure 3.5. Erodent particle impact causes a strain build-up in the coating and sub-surface lateral cracking starts to occur in the hard brittle coating. These crack systems interact eventually resulting in the loss of fragments of the coatings. When the coating thickness decreases sufficiently, vertical cracks initiate and extend from the coating to the substrate which results in severe coating fragmentation and loss.

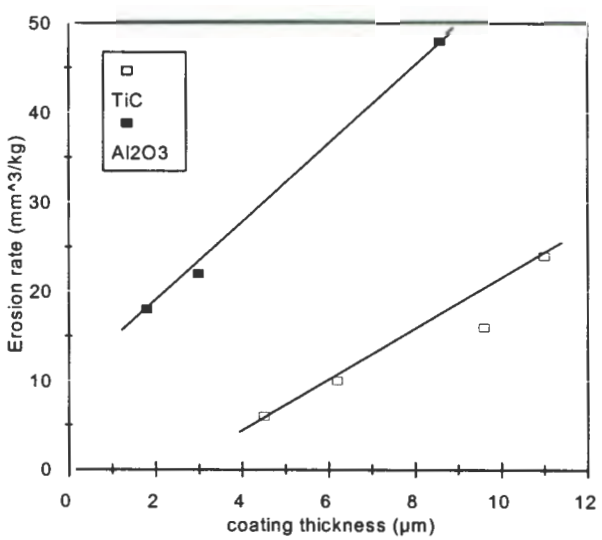

Figure 3.5 : Graph of erosion rate vs coating thickness showing an increase in erosion resistance with an increase in coating thickness [73]

3.6.3 The importance of coating microstructure when considering wear resistance

Olsson et al [76] state that a fine grain size, low porosity and a good coating - substrate adhesion promote better wear resistance. They also found that an increase in grain size

is related to an increase in coating thickness, due to slower cooling rates following application. This increase in grain size led to an increase in erosion rates, which is in agreement with Hogmark and Hedenqvist [73].

The negative aspects associated with applying a thick coating such as large grain size, high porosity and potential residual stresses, can be alleviated by a post application heat treatment consisting of quenching followed by tempering. This would of course increase the production cost, which would have to be weighed up against the improved wear resistance of the coated article.

The effectiveness of a post application heat treatment is borne out by Qureshi & Tabakoff [77], who found that the post application ageing of a chromium carbide coating on a stainless steel substrate showed the best wear resistance in their test series. The heat treatment transformed a fraction of the total Cr_2C_3 to a new type of carbide Cr_7C_3, which increased its hardness. An increase in coating hardness, resulting in increased erosion resistance is in agreement with Davis et al [72] and Hogmark and Hedenqvist [73]

3.6.4 The effect of particle velocity on the erosion of coated surfaces

Shanov et al [78] experimented with titanium nitride, titanium carbide and alumina CVD coatings applied to cemented tungsten carbide specimens. It was noticed that the erosion rate increases significantly over a range of particle velocities of 140-280m.s^{-1} when using 180μm alumina erodent particles. Furthermore, it was observed that these coatings were more sensitive to changes in particle velocity than the bare substrate. The velocity exponent of the substrate was found to be 2.52 and the highest from the coatings 2.82. However, the substrate eroded at a rate an order of magnitude greater than the coatings.

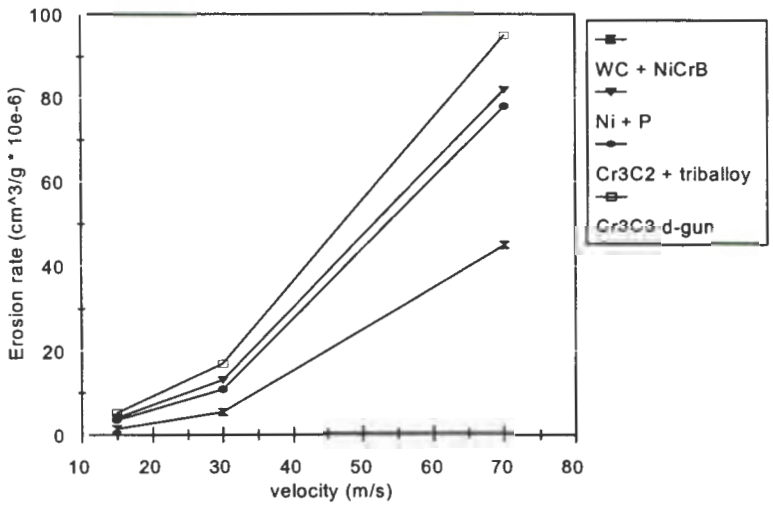

Figure 3.6 : Graph of Shui et al [79] clearly illustrating the trend of increasing erosion rates with increasing velocity

Shui et al [79] also examined the effect of velocity on coated surfaces. The results of this testing can be seen in Figure 3.6. They examined the erosion performance of detonation gun, sputtered and electroless coatings. Although a direct comparison with the bare 1018 carbon steel was not made, nor coating velocity exponents quoted, it is clear that the coating erosion rate increases substantially with particle velocity for all of the systems.

Thus it is to be expected that the erosion wear rates of coated surfaces are more sensitive than the bare [80] substrate to particle velocity. Furthermore, it is to be expected that wear rates will increase exponentially as a function of increasing particle velocity [81].

3.6.5 The effect of temperature on the wear of coated materials

The effect of temperature as a variable in test conditions is a complex one. This is in part due to the number of changes that temperature has on the bulk mechanical properties of the article under consideration.

Shanov et al [78] tested titanium carbide (TiC), titanium nitride (TiN) and alumina (Al_2O_3) CVD coatings over a wide range of conditions of velocities and temperature. The velocities ranged from 140 to 280m.s^{-1} and the temperatures from 20 to 650°C. They found that temperature had a weak effect on the erosive wear rate of their coated specimens, which can be seen in Figure 3.7. Wear rates decreased for the TiC and TiN and rose only slightly for the Al_2O_3 with increased temperature. The bare substrate, a cemented tungsten carbide, eroded at an order of magnitude higher than the three coatings. These tests were conducted at an angle of impingement of 90°, which is the angle at which maximum wear takes place for the brittle substrate and coatings.

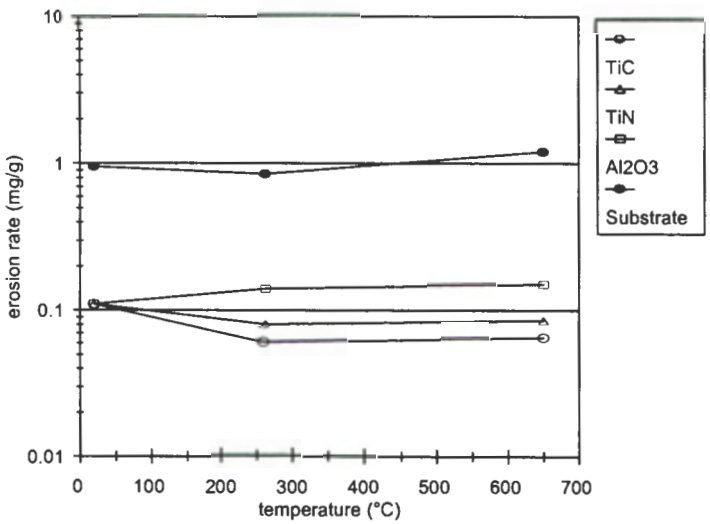

Figure 3.7 : Graph of erosion rate versus temperature for Nitrided and Carbided specimens, showing a weak effect of temperature on erosion rates [78] .

The drop in erosion rates with increasing temperature, as observed by Shanov et al [78], is indeed applicable only to the CVD coatings. Using the detonation gun technique of coating deposition, Sue & Tucker [80] performed erosion tests with chromium carbide and nickel chrome coatings on an Inconel 718 substrate. These coatings were prepared in two different microstructures and compared directly. In addition, the effects of temperature on the erosion rate of the coatings was examined exclusive of oxidation effects, by running the tests in an inert atmosphere. Tests were conducted using 27µm alumina particles at 120m.s^{-1}.

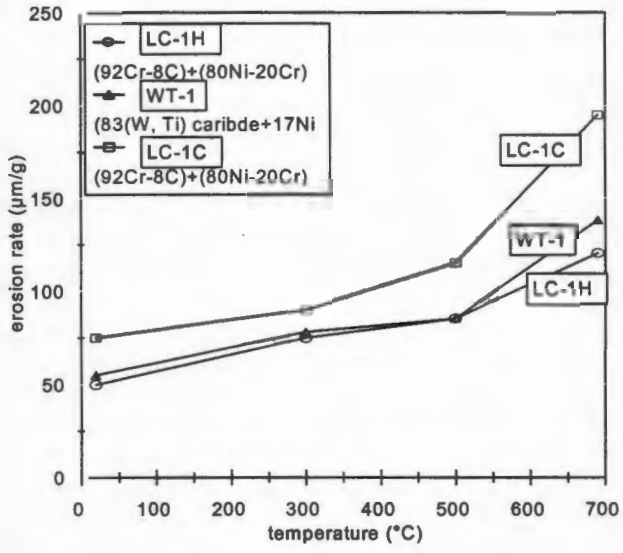

Figure 3.8 : Graph of erosion rate versus temperature for several detonation gun coatings, showing a stronger dependence of erosion rate on temperature [80]

A decrease in erosion resistance with temperature was observed and can be seen in Figure 3.8. Detonation gun deposited coatings are similar to arc sprayed coatings in that molten or semi-molten metal powders are directed onto the substrate at high velocities. The impact causes thin lenticular particles or splats to form on the surface. The decrease in erosion resistance is attributed to weakening of the splat to splat strength with temperature, which in turn is associated with a change in the coating microstructure [80].

4. The design of the high temperature erosion apparatus

This section describes the design and performance of the high temperature erosion rig that was commissioned for the purpose of investigating, under laboratory conditions, the phenomenon of high temperature erosive wear of boiler tube steel used in the South African pulverised fuel electricity generating industry. It outlines the design requirements and constraints as well as describing the features of the apparatus that make up the whole. The performance of the apparatus is discussed and the results from design testing are shown. In addition, the instrumentation and methods of measurements are discussed.

4.1 Design requirements and constraints

The following requirements were established for the design of a high temperature erosion rig following an analysis of coal fired boiler plant operation in South Africa :

- Working pressure : < atmos. i.e. 90kPa
- Working temp : range from 20 to 600°C (specimen)
- Erodent velocity : $10 m.s^{-1}$ to $40 m.s^{-1}$
- Erodent mass flux : 5 to 20% of the gas flow by mass
- Erodent type : plant fly ashes
- Erodent particle size : ranging from 20 to 150μm
- Operating time/run : 30 minutes initially, with scope for modification

The following list outlines certain constraints which had to be taken into consideration in the final rig design.

- The rig must be small enough to fit into limited laboratory space.

- The rig must be easily manufactured to shorten construction time, as well as being simple in design to allow easy maintenance.
- All of the erodent must be recovered from each run, with attention being paid to the respiritable range of particles (i.e. < 5 μm in size).
- Any combustion gases produced as a result of using a hydrocarbon flame to simulate boiler conditions must not be hazardous and be safely dispersed.
- Combustion gases must also be cooled before injection into the ventilation system.

Although the following points are preferences of a more general nature, there is some overlap with the constraints mentioned.

- The test specimens must be of a simple geometry so as to be easily machined and positioned. In addition, they must conform to a size that allows direct transfer from the rig to a scanning electron microscope for qualitative analysis of the wear surface.
- All parts of the apparatus should be easily obtainable / machineable, as well as being accessible to facilitate fast replacement or repair, since the erodent will not only erode the test specimen but the remainder of the rig as well.
- It was also desirable that all of the temperature measurement points should have feedback in order to continuously record operating parameters.

4.2 A description of the apparatus

Following a review of the research conducted into high temperature erosive wear, it was decided to build an apparatus which incorporated several common features of other designs together with added features considered necessary for this particular application. The final design is one in which compressed air is preheated, has erodent particles introduced into it and is then passed through a duct in which a hydrocarbon gas is combusted. This provides most of the heating power required to achieve the specimen

temperatures. The gas and erodent mixture then impinges on the target whereafter the mixture is cooled and the particles recovered.

This section explains the philosophy behind the design and then discusses each component of the apparatus in detail. Table 4.1 lists the main component features of other laboratory high temperature erosion apparatus and the separate components used in the present design to show how heed was taken of existing experience in this field.

Component	Bauver & McGough [82]	Colcough & Yeomans [83]	Tabakoff & Wakeman [84]	Current design
Burner	X			X
Combustion chamber	X		X	
Air heater (i.e. air preheat)		X		X
Erodent feed device	X	X	X	X
Vertical acceleration tube	X	X	X	X
Cooling section (i.e. a heat exchanger)	X		X	X
Erodent particle collector	X		X	X
Induced draught fan exhauster	X			

Table 4.1 : The X's in this table show the use of the component listed in the first column. These listed components show a common understanding of the features necessary for inclusion in the design of a high temperature erosion apparatus.

4.3 The design philosophy

In order to simplify as well as expedite the design process, it was decided to adopt a modular approach to the overall plan. It was predicted at an early stage that modifications would be necessary in order to develop a successful system. These would have to be implemented without having to rebuild large parts of the apparatus each time. The modular construction also allows easy maintenance and part replacement which is important when considering the harshness of the tribo-environment to which the apparatus is subjected.

The apparatus is shown in diagrammatic form in Figure 4.1, whilst Figures 4.2-4 show the apparatus in photographic form.

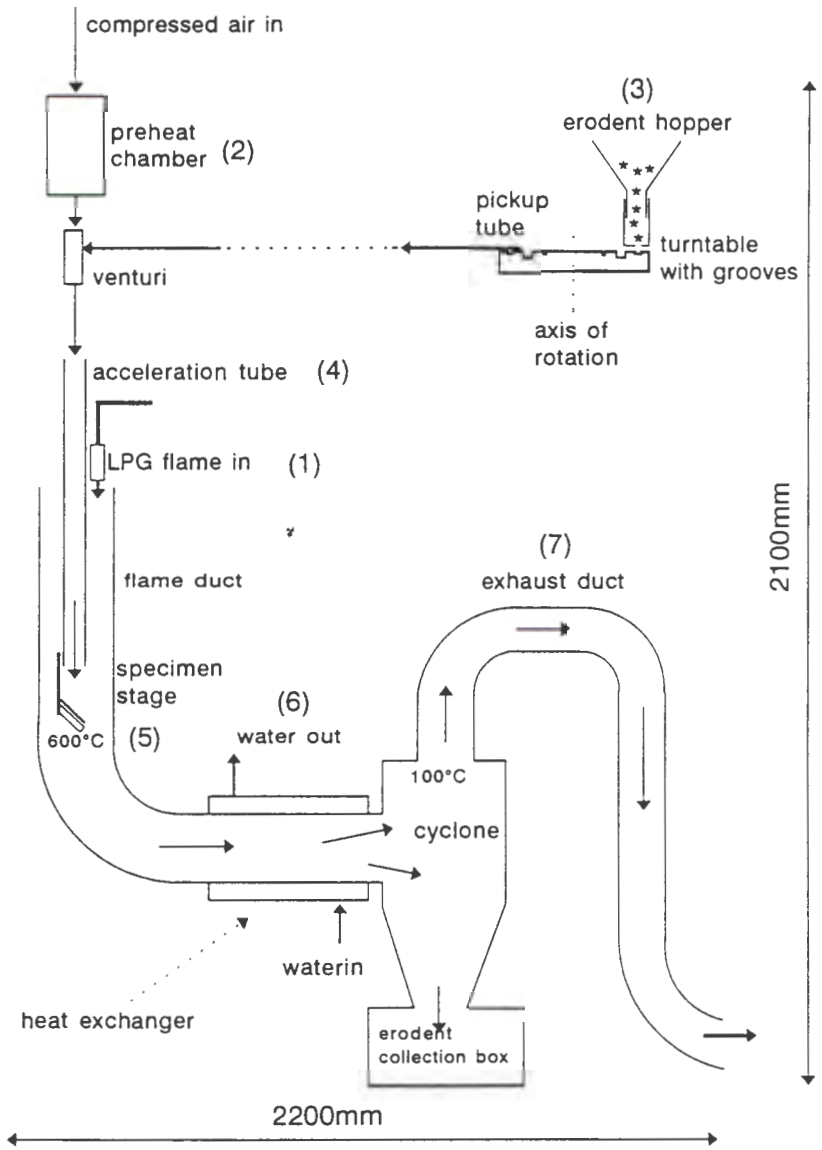

Figure 4.1 : Diagram of the high temperature erosive wear apparatus. The numbered features (1) - (7) correspond to those in the photographs of the apparatus.

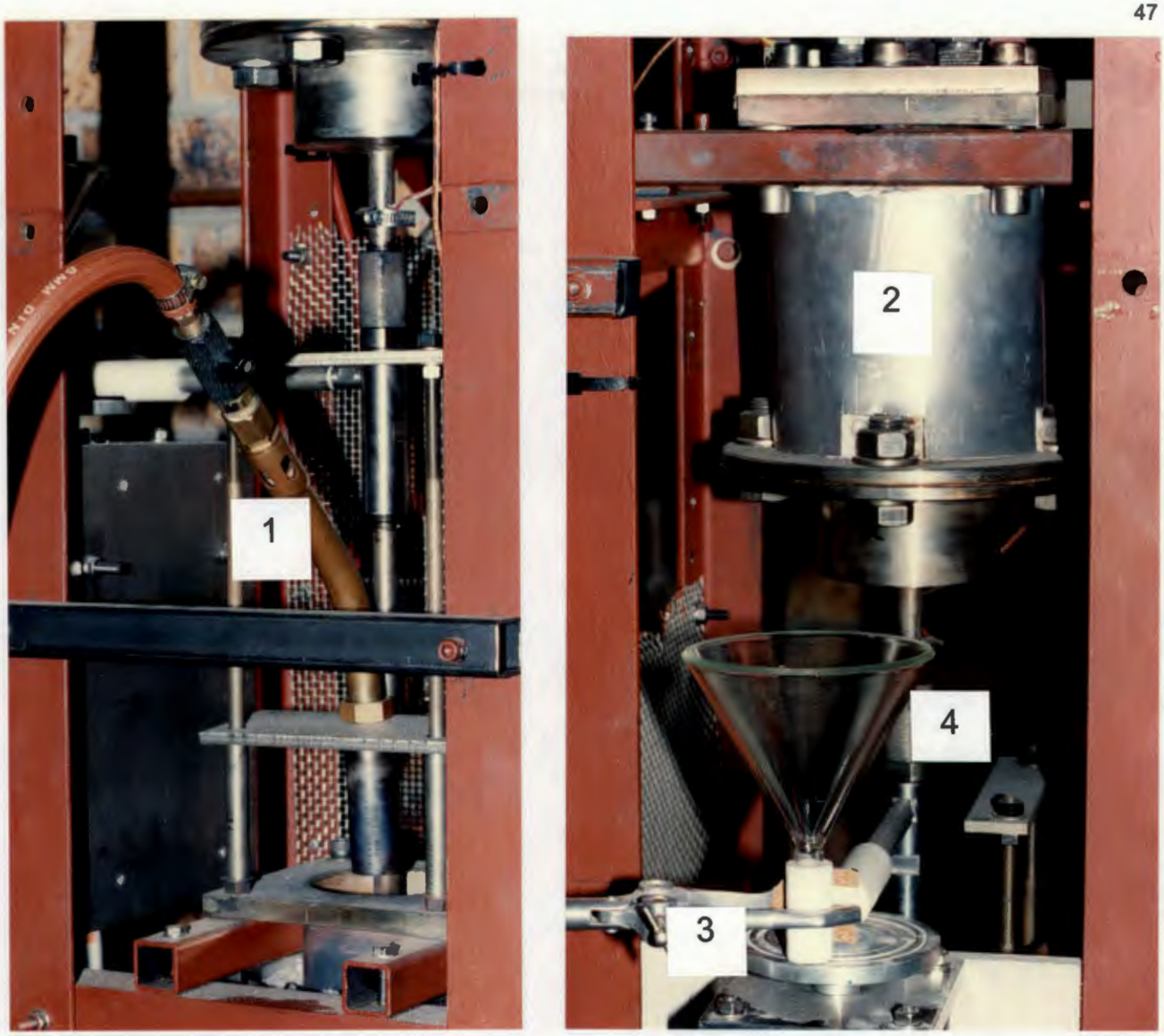

Figure 4.2 : Photographs of the erosion rig : (1) Gas flame, (2) Preheat chamber, (3) Erodent feeder, (4) Acceleration tube.

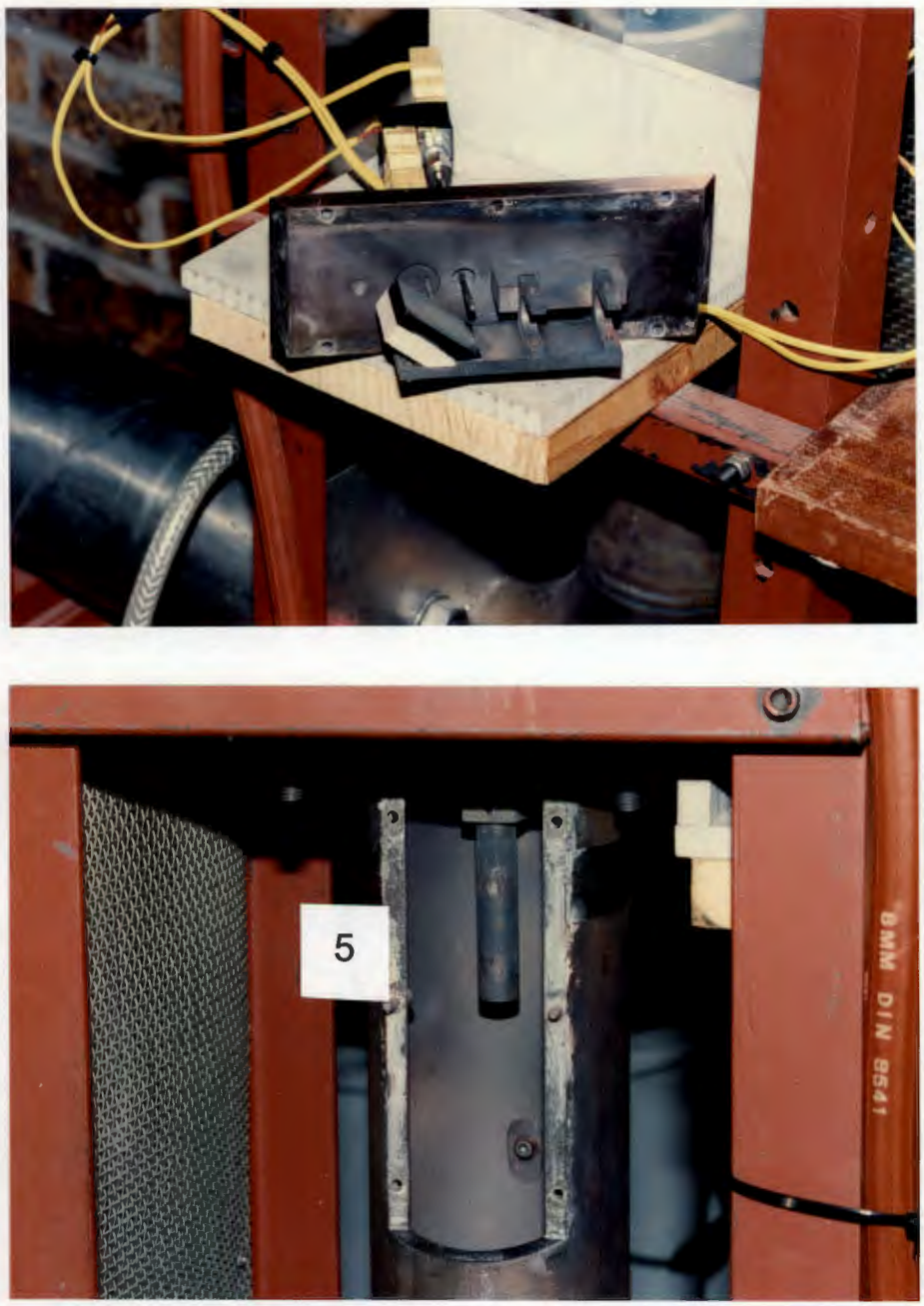

Figure 4.3 : (a) The test section, which is attached to the chamber cover plate to facilitate expeditious specimen removal following a test. (b) The specimen chamber (5) which the test section is inserted into.

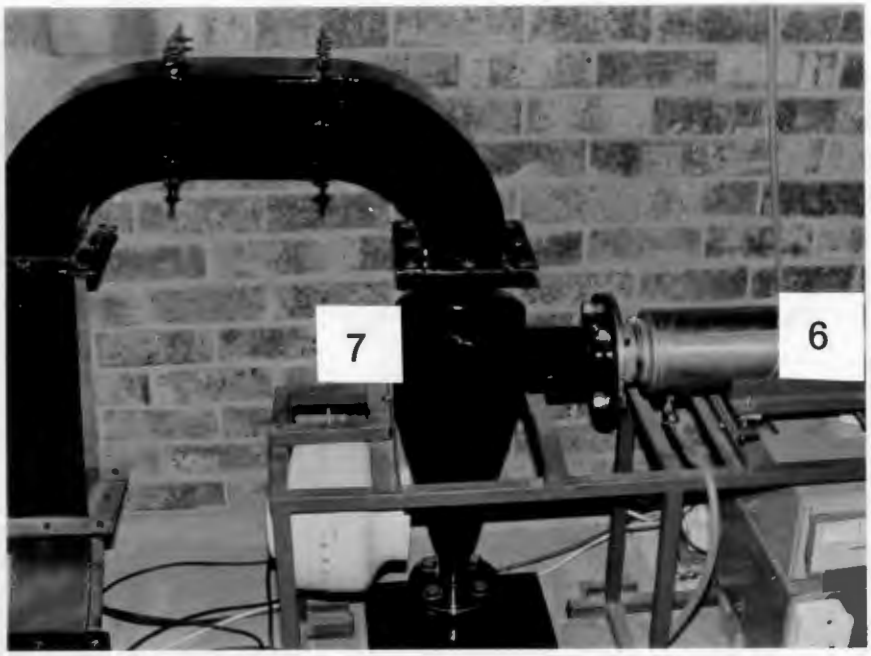

Figure 4.4 : The cooling section (6) coupled to the cyclone separator and exhaust duct (7). It can be seen how the exhaust duct effectively increases the height of the cyclone outlet pipe.

4.4 Detailed description of the methods of obtaining the high test temperatures : i.e. Combining the electrical preheat chamber and the L.P.G. flame

4.4.1 The electrical preheat chamber

The initial design approach was to mix the combustion products of the L.P.G. flame and erodent in a pressurised combustion chamber. However, the safety hazards of such a system precluded this. The safer approach adopted is to preheat the air in an electrically heated chamber. The acceleration tube then runs through a duct containing the hot combustion gases from the L.P.G. flame to achieve the necessary high specimen temperatures. This is similar in concept to the apparatus designed by Tabakoff and Wakeman [84], which is described as a "hot windtunnel".

The compressed air supply is passed through a water and oil coalescing filter prior to injection into the chamber. This ensures that the air has a low moisture content and is

debris free. The preheat chamber heats the air to ± 80 °C before its entry into the venturi and the acceleration tube. This is achieved by inserting ceramic heating elements sheathed in AISI grade 304 stainless steel into an expansion/contraction chamber. Six elements of 400W capacity each are used giving a heating power after losses of approximately 2.2 kW.

The elements are secured in the top of the preheat chamber by *Swagelok©* taper lock fittings and thus hang freely in the chamber. The cycling of temperature between operating and idle conditions and the differences in coefficient of thermal expansion between the ceramic filler, inconel windings and stainless steel sheath causes distortion of the elements. This can result in the inconel windings touching the sides of the sheaths inducing current flow to the rest of the apparatus. The heating elements and hence the preheat chamber thus have to be electrically isolated. This was achieved by powering the thermostat (which powers the elements) with an isolation transformer.

An additional complication found with the heating elements was that the ceramic within the sheath was exposed to atmosphere where the leads are connected to the power supply. Porosity in the ceramic causes it to become hydroscopic following high temperature work. If too high a current was passed through these elements after a prolonged time period between experiments, the moisture accumulated in the ceramic caused electrical shorting. As a consequence the temperature of the elements was set to 50°C for one to two hours, with a 0.6 bar supply of air, prior to extended use. Following this, a setting of 150°C was used for the preheat chamber.

Temperature control is provided by a *Eurotherm* thermostat, which, as mentioned, receives its power from an isolation transformer. A K-type thermocouple is attached to one of the *Swagelok©* taper locks to give rapid feedback to the *Eurotherm*. The feedback thermocouple was initially attached to the cone section of the preheat chamber. However, the cone is 90 mm in diameter and is constructed of AISI grade 316L stainless steel, which resulted in a considerable lag between start-up of the elements and any temperature increase at this point. This in turn resulted in excessive current being supplied to the

elements which shortened their lives considerably. Attaching the feedback thermocouple to one of the taper locks allows a more rapid response between the *Eurotherm* and the heating elements which results in improved element life.

4.4.2 Combining the electrical preheat chamber and the L.P.G. flame

It cannot be assumed, however, that the specimen is heated solely by the airstream and erodent particles or that thorough mixing of the airstream and combustion gases from the LPG flame takes place. This heating of the specimen and particles takes place through the following additive processes 1 + 2 + 3.

1. The radiant heat from the flame which at a gas flow rate of 1.2 kg/hour has a power output of approximately 7 kW (flame "power" = hydrocarbon heating value kJ/kg * gas mass flow rate kg/s [85,86]), heats the specimen up such that its surface is at a higher temperature than the impinging air / erodent mixture until equilibrium is reached.

2. The flame impinges directly on to the acceleration tube and heats it to temperatures exceeding 800°C. The hot surface heats the passing air and particles by convection and radiation.

3. The combustion gases from the flame mix with the intake of the air through the flame duct maintaining the temperature of the specimen chamber. It is unlikely that the gases mix with the air and the erodent in the 20 mm between the nozzle exit and specimen. The nature of the erodent carrying gas is oxidising.

4.4.3 Heating of the particles

The complexity of the heating mechanism makes exact prediction of the final temperature of the erodent particle difficult. The particles flowing in the acceleration tube are heated by a combination of convection from flowing through the hot tube, radiation from the glowing tube as well as possible conduction from collisions of particles with the tube wall. Heating of the particles by convection is initially analysed [87], followed by a discussion of the thermal conductivity of the particles.

Analysis of heating by convection involves the determination of a heat transfer coefficient for the glowing tube by using the dimensionless Reynolds (Re_d), Prandtl (Pr) and Nusselt (Nu_d) numbers in the following way [87] :

$$\mathbf{Nu_d = 0.023 * Re_d^{0.8} * Pr^{0.4}}$$

$$\text{and } \mathbf{Nu_d = h*d/k}$$

h = heat transfer coefficient ($W.m^{-2}.°C^{-1}$)

k = thermal conductivity of the air ($W.m^{-2}.°C^{-1}$)

$$\mathbf{q = h*(\pi*d*L)*(T_w - T_{b\,in})} \text{ (W)}$$

$$\text{and } \mathbf{q = m'*C_p*(T_{b\,out} - T_{b\,in})} \text{ (W)}$$

$$\text{hence : } \mathbf{(T_{b\,out} - T_{b\,in}) = h*(\pi*d*L)*(T_w - T_{b\,in})/m'*C_p}$$

q = available heat in the system (W)

T_w = tube wall temperature (°C)

$T_{b\,in}$ = bulk gas temperature at the entrance to the tube (°C)

$T_{b\,out}$ = bulk gas temperature exiting the tube (°C)

m' = mass flow rate of air ($kg.s^{-1}$)

Cp = specific heat of air ($kJ.kg^{-1}.K^{-1}$)

d = inner diameter of tube (m)

L = length of tube (m)

$$\mathbf{Nu_d = 97}$$

hence $\mathbf{h = 256 W.m^{-2}.°C^{-1}}$

and $\mathbf{T_{b\,out} = 490°C}$

Thus the final temperature of the air was calculated for the lowest air supply pressure to be used in materials testing. Although the air cannot reach the same temperature as the tube surface, the additive nature of the heating mechanism ensures that the final temperature of the specimen satisfies design requirements.

The range of particle velocities in the apparatus is 24 to 51m.s^{-1}. This implies a range of particle flights in the acceleration tube of between 0.025 to 0.012s. There was concern that this difference might result in a substantial difference in the temperature of the particles between low (24m.s^{-1}) and high (51m.s^{-1}) velocities.

However, if the heat transfer coefficient is dependent on the Nusselt number (Nu_d) this implies a dependence on particle velocity to the power of 0.8. There is thus a 191% *increase* in the heat transfer coefficient from the lowest velocity to the highest. This is in contrast to a 117% increase in velocity from the lowest velocity to the highest. This implies that the heating of the particles becomes more efficient as the air velocity increases. Furthermore, a comparison was made to check the time necessary to heat the three different erodent particle types to 600°C compared with the time spent in the acceleration tube.

This was achieved by equating the heat required in Joules to heat the particles; to the heat available in Watts multiplied by the time taken to achieve a uniform particle temperature.

$$\mathbf{C_p * m_{erodent} * \Delta T = q * \Delta t}$$

C_p = specific heat of the erodent particle (J.kg^{-1}.K^{-1})

$m_{erodent}$ = approximate mass of erodent at any time in the acceleration tube for an erodent mass flow of 12.8x10^{-6} kg.s^{-1}.

ΔT = required particle temperature rise

q = available heat in the system (W)

Δt = time taken to heat a particle uniformly (s)

The time taken to heat one particle up from 20 to 600°C is shown in Table 4.2. The times taken for a particle to reach the required temperature are shown for heating powers of 7kW and 1kW. It is clear from this analysis that the particles reach the required temperature with the available heating power supplied by the hot acceleration tube. The required temperature is reached a minimum of 2 orders of magnitude less than the time spent in the tube.

Particle type	Thermal conductivity ($W.m^{-1}.K^{-1}$) [88]	Specific heat ($J.kg^{-1}.K^{-1}$) [88]	Time to 600°C for q = 7kW (s)	Time to 600°C for q = 1kW (s)
Coal ash (56.2% SiO_2 and 27.8% Al_2O_3)	9.01	443	$11.8x10^{-6}$	$82.4x10^{-6}$
SiO_2	1.05	125	$3.32x10^{-6}$	$23.2x10^{-6}$
SiC	260	54	$1.43x10^{-6}$	$10.0x10^{-6}$
Al_2O_3	25.1	775		

Table 4.2 : A list of the thermal conductivities of the erodents (including the derived conductivity for coal ash) and the time taken to heat the mass of particles within the acceleration tube at any point in time from 20°C to 600°C.

4.5 The design of the erodent supply unit

The design of an erodent feeder giving a steady and smooth supply is critical to the reliability of test results. The initial system employed was a double cone arrangement whereby the flow of particles was controlled by fitting nozzles of various orifice diameters to the first cone. This controlled the rate of flow into the second cone by restriction which works well for mass flow rates of approximately 0.15 $g.s^{-1}$ of erodent and above. This was

obtained using a Teflon nozzle with a 1.2 mm diameter orifice. However, below this value the supply became intermittent. The erodent was then mixed with the airstream through a tube running from the second cone to a venturi.

The venturi is a crucial part of the apparatus which mixes the erodent into the airstream. By narrowing the diameter of the tube carrying the air, a high pressure stream is created which is expanded into a chamber of the same diameter as the tube carrying the incoming air. A low pressure zone is thus created within the chamber, enabling particles to be mixed into the airstream through an orifice at the side of the venturi (which will be referred to as the venturi mouth), behind the exit of the narrowed tube.

The original position of the venturi was ahead of the preheat chamber. However, when the preheat chamber reached an operating temperature of approximately 200°C, the back pressure generated by the expanding air inside the chamber was such that it changed the negative pressure at the venturi mouth to a positive value. When particles were introduced, they were immediately ejected from the hopper by the buffeting shock waves from the chamber.

It was initially thought that this was the result of "choking" at the chamber outlet. However, calculations showed that the threshold Mach number for the onset of choking was not exceeded. It was concluded that the buffeting was as the result of a resonance between the incoming force of the air and the back pressure within the heating chamber from the air expansion due to heating and subsequent forced contraction back into a narrow tube. By modifying the rig and installing the venturi after the preheat chamber (see Figure 4.1), this problem was overcome; unfortunately at the expense of a drop in air/erodent preheat temperature.

As a result of these flow difficulties, much time and thought was expended in the search for a simple and reliable erodent feed mechanism. A potential method examined at the time was a fluidised erodent bed. The advantages of a heated, fluidised erodent bed are :

- Good heat transfer from heating elements to the erodent / air mixture .
- Erodent (fly ash in particular) does not conglomerate and cause blockages [89] as often occurs when passing through narrow orifices.

The disadvantages are :

- Erodent supply to the acceleration tube is unsteady if the bed is pressurised, unless particles are passed through intermittently as shown by Chinnadurai and Bahadur [90].
- Supply of particles cannot be continuous over long time periods unless the fluidised bed is fed by yet another device i.e. the fluidised bed would still have to be fed by a hopper to hold its level steady. It was this final point which resulted in rejection of this potential feed mechanism as problems experienced with the erodent supply using the conventional double cone method would have been inherited by the fluidised bath.

To achieve the lower mass feedrates required to simulate the low mass fluxes experienced in pulverised fuel boilers it was decided to adopt the Shipway and Hutchings' [26] novel turntable feeder device. In this design a hopper is used to feed particles into a groove machined into the surface of a slowly rotating disk. A tube from a venturi then sucks the particles into the acceleration tube.

The device, shown in Figure 4.1, consists of an aluminium disk with grooves of varying depth and width. The disk rests on an INA AXK 0619TN + AS 0619 axial needle roller bearing washer combination. It is connected to an RS type 341-660 12 V dc motor which has a range of speed of 0 to 20 rpm via an RS Oldham flexible coupling type 748-027. Particles are supplied to the turntable by a glass hopper with a Teflon nozzle which has a 1.5 mm diameter orifice.

The exception to this arrangement is in the supply of fly ash which does not flow easily through any constriction of decreasing section such as a cone. Fly ash is thus supplied to

the grooves on the turn table by an 80 mm acetyl tube with a 10 mm inside diameter. Using the lowest speed possible the ash falls easily from its tube onto the turntable.

The particle mass feedrate and hence particle flux is thus controlled by the speed of the disk. For example Table 4.3 shows the dependence of the particle mass feedrate (of SiO_2 particles) and hence the particle flux on the rotational speed of the turntable for the outermost groove.

Rotational speed (rpm)	Particle mass flux ($kg.m^{-2}.s^{-1}$)
20	0.70
10	0.37
3.5	0.15

Table 4.3 : An example of how the particle mass flux is dependent on the rotational speed of the turntable (outermost groove).

4.6 Design of the Acceleration drop tube

Clearly the value of the particle velocity in the erosive wear test system is of the utmost importance. This will become apparent throughout this work. The diameter and length of the acceleration tube plays a crucial part in establishing the maximum velocity attainable in the system, as well as the nature of the flow i.e. laminar or turbulent [31,91].

The length of the tube necessary to achieve the maximum required velocity of $40m.s^{-1}$ as listed in section 4.1 was determined by examining the ideal case where there are no wall effects and no particle - particle interference. One dimensional Newtonian turbulent flow was assumed [92] and the forces on a 115µm fly ash particle of density $1990kg.m^{-3}$ (modelled as a perfect sphere) balanced as it is introduced in to the air flow :

Particle drag force + buoyancy = particle weight + fluid force

simplified : **Particle drag force = required fluid force**

The particle drag force F_D:

$$F_D = \frac{1}{2} * C_D * \rho_f * U_{rel}^2 * A$$

C_D = drag coefficient

ρ_f = fluid density

U_{rel} = relative velocity i.e. air velocity - particle velocity

A = particle cross-sectional area

F_D = 4.387×10^{-6} N (for a particle velocity of 40m.s^{-1})

= particle mass x acceleration

= 1.585×10^{-9} x acceleration (N)

As drag force F_D relies on the relative velocity between the air and the particles, drag force will decrease as the particles accelerate. A rigorous analysis entails examining small increments of tube length and stopping the iteration when the desired particle velocity was obtained. However, a simple case where linear acceleration was assumed was examined which resulted in a realistic value of tube length.

The acceleration and hence distance required to propel a particle from rest to 40m.s^{-1} were thus derived. This distance was found to be 289mm. However, the final length chosen was 600mm. This was out of concern firstly that the design calculations assumed no wall effects nor particle - wall interference and would hence underestimate the necessary length. Secondly, inadequate heat transfer would take place between the hot tube and the passing air and erodent mixture with a short tube length.

The choice of the diameter of the tube was as much a practical choice as a scientific one. Too large a diameter would have necessitated a large specimen size to ensure that all the

particles struck the exposed target surface. Too small a diameter would have resulted in large pressure losses as the gas expanded through the preheat chamber and then contracted into the acceleration tube. This would have had the effect of limiting the maximum particle velocity.

Losses in particle velocity which prevent the particles from approaching the gas velocity depend on the diameter *and* the length of the acceleration tube. An excessively long tube would also result in pressure losses due to wall / gas friction. As particle velocity is dependent on air supply pressure, a drop in supply pressure would result in a drop in particle velocity.

Eventually it was decided to adopt the same aspect ratio as that of Shipway and Hutchings [26] who used a value of 60. As the minimum tube length had been estimated at 289mm, this was lengthened to 600mm, which demanded a tube diameter of 10mm. The final 100mm of the acceleration tube which is of seam welded AISI 316L stainless steel, was bored to 10.00mm to remove the internal weld line. The nozzle exit was smoothed by machining a 45° chamfer and had 106-125μm diameter silicon carbide particles blown through it at $3.039 \times 10^{5} N.m^{-2}$ (2 bar) of air pressure to remove any remaining asperities. This was to minimise the divergence of the particles upon their exit from the tube.

4.7 The design of the test section of the apparatus : The specimen chamber and the specimen stage.

The physical size of the test section is seen in Figure 4.2 and Figure 4.3. The test stage is attached to the cover plate. This allows the coverplate and test stage to be removed simultaneously thereby reducing specimen changeover time. A graphite based gasket material adequately seals the gap between the coverplate and the chamber.

The attachment of the specimen stage to the chamber cover also means that the necessary thermocouples are permanently in place ensuring the repeatability of temperature measurements. Two K-type thermocouples are fixed at this point, one to measure the temperature of the specimen immediately behind the impact surface and the other adjacent to the acceleration tube nozzle in order to continuously record ambient temperature conditions in the specimen chamber.

The specimen is attached to the stage by means of a cap screw from the rear and it allows all of the impacting particles to strike the exposed surface. Lateral movement of the specimen is inhibited by 1mm ridges on each side of the stage. The plate backing the specimen stage is machined out of a *Morganite ceramic fibres inter ohm* alumino-silicate fibre board. This acts to insulate the specimen from the remainder of the AISI 316L stage.

A 1.9mm hole is drilled in the side of each specimen to the centre to accomodate a K-type thermocouple and thus ensure an accurate temperature reading during testing. The stand-off distance from the centreline of the nozzle to the centre of the specimen is fixed at 20mm. The specimen orientation is 40° to the gas stream. Changing the stand-off distance would involve shortening the acceleration tube, whilst the specimen orientation is changeable by replacing the stage.

4.8 The design of the cooling and cyclone / exhaust system of the apparatus

4.8.1 The cooling system of the apparatus

The cooling of the gas mixture is achieved by passing it through a duct surrounded by a water jacket. Although cooling would be more effective by passing the mixture over banks of tubes to increase the cooling surface area [93], the aggressiveness of the high temperature erosive conditions precluded this. The configuration of the heat exchanger is seen in Figure 4.1 and Figure 4.4. It consists of an inner and an outer tube. The inner AISI 316L stainless steel tube has a diameter of 90mm, whilst the outer tube is a 4mm thick, 130mm diameter AISI 304L stainless steel tube. The outer tube is 600 mm in length and thus has a 3.67 litre cooling volume. The water inlet is at the end of the heat exchanger, closest to the cyclone, whilst the outlet is located at the other end.

The length of the outer tube was determined from considerations of heat transfer [87]. The required drop in gas temperature was used to calculate the amount of heat that needed to be lost. This quantity was related to the change in water temperature that must occur as it absorbs this heat. A mean cooling water temperature was then derived, after which the area over which heat transfer must take place was determined. The diameters of the available tubes were known and thus by selecting a tube diameter, its length could be determined from the required heat transfer area. This approach is detailed as follows :

$$\mathbf{q = m_g C_g \Delta T}$$

where

	q	=	heat from cooling gases (kW)
	m_g	=	mass flow rate of the gases (kg/s)
		=	0.010
	C_g	=	spec. heat of the mixture ($kJ.kg^{-1}.K^{-1}$)
		=	1.433 [94]
	ΔT	=	change in temperature (K)
		=	500

thus q = 0.010*1.433*500

= 7.165kW

ΔT_m , the log mean temperature difference for counterflow double tube pipes [87] is then found as 240K.

If **q = U*A*ΔT_m**

where U = Overall heat transfer coefficient
(estimated at 320 $W.m^{-2}.°C^{-1}$ [87])
A = Heat exchanger area (m^2)
= $0.09375m^2$

hence **L = 373mm**

The outer tube was thus chosen to be 600mm in length to ensure adequate cooling.

4.8.2 The cyclone / exhaust system of the apparatus

After cooling, the mixture passes through a cyclone to separate the erodent from the gas mixture to minimise damage to sensitive laboratory equipment and ingestion of particles by the operator. Key points in cyclone design [95,96] are outlined before commenting briefly on its effectiveness :

The principle of cyclone operation is to create a vortex in the cylinder by imparting a tangential velocity to the incoming gas and erodent mix. The effect of the tangential velocity is two fold. Firstly, it throws the heaviest particles to the outside of the cylinder where they roll down the sides of the cyclone to the collection box. Secondly, the vortex swirls to the bottom of the cyclone, to a point above the collection box, and then changes

direction and swirls up and out. The majority of the remaining particles then drop out of the gas stream, and fall into the collection box at the bottom.

It is important to have a good seal between the cyclone and the collection box, as any leakages appear to disturb the vortex which results in reduced efficiency. Cyclone design appears to be largely empirical, hence the design rests on maintaining geometric similarity with proven designs. The cyclone used in this work was of mild steel plate welded construction, with a 4mm thick section in the initial cyclone section, and 3mm plate for the rest, since the initial section was found to wear considerably faster than the rest of the device, due to the gas and erodent mixture impinging on it at an acute angle.

The important dimensions in the design are listed below and shown in Figure 4.5.

Hc = height of inlet pipe
Sc = clearance of outlet from the bottom of the inlet
De = diameter of the outlet pipe
Dc = diameter of the initial cyclone section
Lc = height of the initial section
φ = angle of the conical section
Zc = height of the angled section
Tc = total height
Jc = diameter of pipe into the collection box

Sc = 0.25*Hc
Dc = 2*Hc
De = Hc
Jc = 0.5*Hc
φ = 14° or less
Lc = Hc + 2*Sc

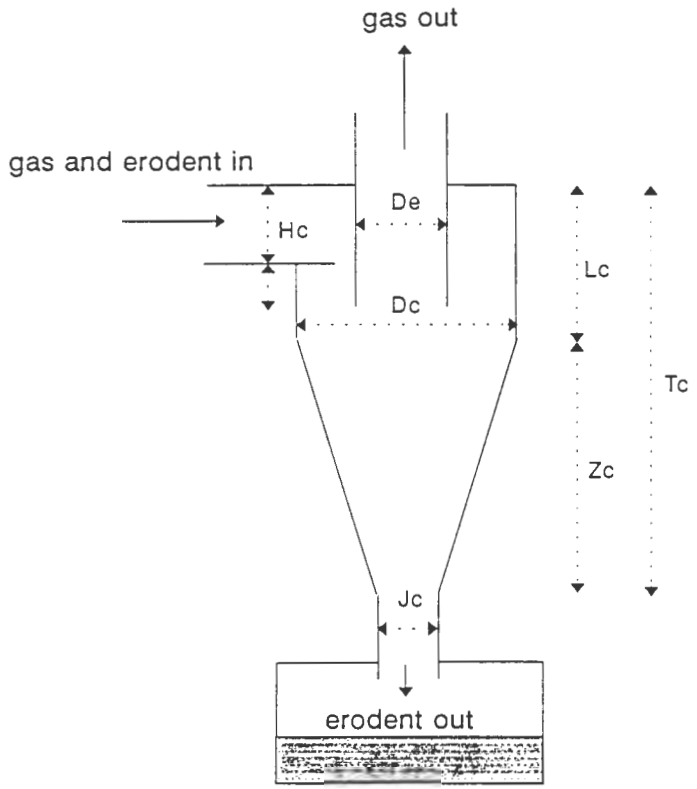

Figure 4.5 : Diagram of the cyclone showing the important dimensions.

It was initially planned to have an induced draught fan situated in series with the cyclone/filter at the cyclone outlet. Its purpose was to suck the gas/erodent through the cyclone resulting in a negative pressure in the rest of the ducting which ensures continuity of flow as well as preventing leakages.

However, the induced draught fan was replaced by an industrial vacuum cleaner. This served the additional task of collecting the small particles in a fabric filter. This arrangement worked well except when the rig was operated at high temperatures and the outlet temperature of the cyclone approached the softening temperature of the polymeric parts in the vacuum cleaner. It was thus decided, before going to the expense of custom building an I.D. fan/filter system, to test the effectiveness of the cyclone alone. Particle recovery was good but not completely effective. An exhaust duct was subsequently designed and fitted. This was to serve the purpose of increasing the heat transfer surface area thus cooling the gas/remaining erodent sufficiently for the vacuum to be used. This configuration is seen in Figure 4.1 and Figure 4.4.

However initial tests without the vacuum showed that the cyclone efficiency had been increased to a near 100% recovery rate. This was due to the increase in the height of the cyclone outlet and the device working more effectively on a slight positive pressure from the incoming flow. The success of the combined cyclone/exhaust duct system was tested by wetting a piece of blotting paper and then holding this just clear of the final outlet. The paper was then examined under a light microscope to find any evidence of the post impacted erodent. No evidence of the erodent in the size range tested (106-125μm SiC) was found. Although the debris in the collection box was not weighed, it was assumed that all of the particles were recovered in this receptacle. These tests were conducted with a high erodent mass feed rate of $0.2 g.s^{-1}$ and an air supply pressure of $3.039 \times 10^5 N.m^{-2}$.

4.9 The performance of the apparatus

The main features of the erosion apparatus have been described in order to give an appreciation of the thought processes behind the final design and an accurate summation of the development that went into its manufacture. The following sections deal with the performance of the apparatus. Each sub-section commences with a description of the instrumentation necessary to determine the performance of the apparatus. The performance is then described in detail to show the extent to which the potential of the apparatus has been exploited.

4.9.1 Instrumentation and Data capture of temperatures

The recording of temperature is done by means of K-type thermocouples at several locations. Thermocouples which read both specimen and specimen chamber temperatures are sheathed in stainless steel but are not earthed. All other thermocouples are attached to the apparatus using jubilee clips. Compensating lead is used to connect the thermocouples from their location to a personal computer (PC) which acts as a data logger. Care is taken when connecting the thermocouple wires to the compensating lead to ensure that no electrical losses result.

The voltage readings are channelled through an analogue to digital (A/D) converter (a *Boston Technologies PC73A*) before being continuously logged and/or viewed continuously on the PC screen. Software was written to continuously log temperature data as a function of time. Eight points of measurement are possible. Only five, however, were used for initial equipment testing. Once a test has been run, the logged data can be imported into a spreadsheet to allow expression in graph form.

Electrical noise was originally thought to be a factor causing fluctuations in temperature readings. The problem was solved in part when the earth leakages from the heating elements were eliminated by isolating the power supply. However the problem was only solved in full by earthing the PC to the apparatus. It was thought that due to the many power supplies in the vicinity of the apparatus that some current leakages were likely, and that prior to earthing the PC, a closed loop was formed, which created a small potential difference between the rig and the PC, thereby affecting temperature readings.

4.9.2 Temperature testing

Testing was carried out to determine the range of temperatures which can be achieved in the system and to determine the accuracy of measurement that can be expected at elevated temperatures.

Thermocouples were placed at a number of critical positions during initial design tests. The main concern was that the heat exchanger would not cool the gases as effectively as calculated before they entered the cyclone, resulting in the cyclone overheating as well as introducing excessively hot gases into the building ventilation system. In addition, the contribution of the cyclone to cooling the mixture was not expected to be great as it could only rely on cooling by convection from the draught of a fan that was positioned for this purpose. It became clear from these tests that the outlet temperature was indeed too high for safe operation, particularly for the polymeric materials in the industrial vacuum cleaner and the change to an extended duct was made.

The temperature of the specimen chamber and the specimen was found to rise quite suddenly after gas ignition, but reach a plateau after several minutes. This can be seen in Figure 4.6 and Figure 4.7.

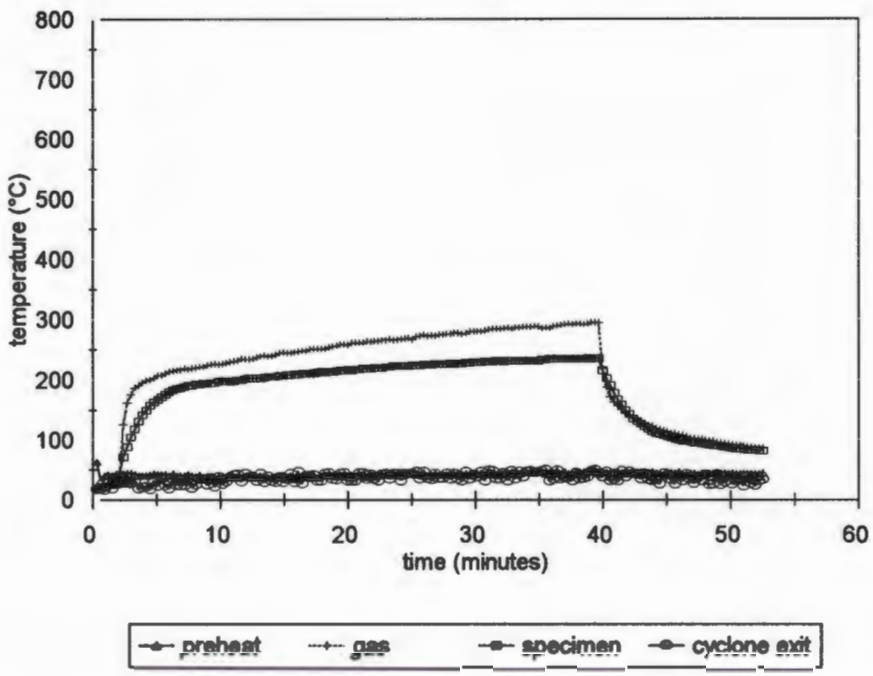

Figure 4.6: Graph of temperature at various positions on the apparatus vs time for a 200°C run. Air supply pressure 0.6 bar, gas supply pressure 20 kPa.

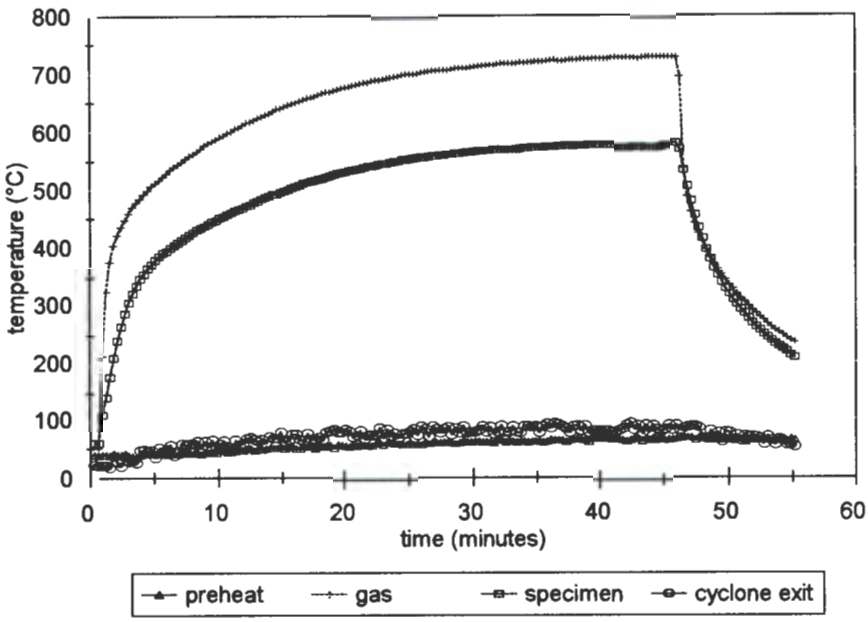

Figure 4.7 : Graph of temperature vs time at various positions on the apparatus for a 500°C run. Air supply pressure 0.6 bar, gas supply pressure 120 kPa.

The time to temperature following ignition of the gas ranges from 10 minutes at the lowest gas pressure setting to 30 minutes at the highest. This corresponds to operating temperatures of 200 and 550°C respectively. When the gas is switched off temperatures drop quickly. However, the time to reach room temperature following extended operation at high temperature can take up to two hours.

Gas temperatures in the specimen chamber as well as the specimen temperature are displayed during all tests. Once the temperature behaviour of the apparatus was established, the temperature versus time data was no longer logged. Readings were taken at the start and finish of a test and the average quoted as the test temperature.

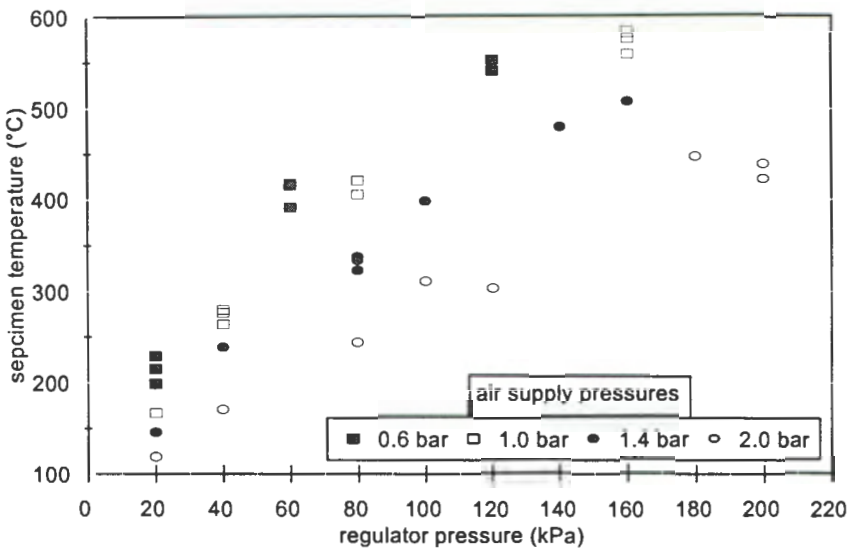

Figure 4.8 : Specimen final temperature versus gas regulator supply pressure for several different air supply pressures. The quoted air pressure is the unit displayed on the pressure regulator where 1 bar = 1 atmosphere of pressure above atmospheric pressure i.e. $2.026x10^5 N.m^{-2}$.

4.10 Measurement of gas and particle velocities

4.10.1 Measurement of the gas velocity

Gas velocity was measured using a static pressure pitot tube with pressure lines run to a *Therm2295-2* digital manometer. The pitot tube was constructed out of spinal column needles and conformed closely to BS 1042 #2.1 [97,98]. The needles had their sharp points ground such that the nozzle was normal to the axis of the needle. The two needles are mounted in a stage which can be attached to the acceleration tube. The manometer has a maximum service temperature of 60°C, thus it was not possible to test the air velocity at high temperatures. Particle velocity was however tested at high temperatures and this will be discussed.

A gas velocity profile [92] was measured using the pitot tube which was then numerically manipulated so as to calculate flow rate and hence derive average velocity. This was done to establish the reported differences between particle and gas velocity in gas blast erosion apparatus [84,91].

The following quadratic equation for a 2 dimensional velocity distribution across the acceleration tube was determined for the four air supply pressures tested namely : 1.418, 1.621, 1.823, $2.026 \times 10^5 N.m^{-2}$.

$$v_{fluid} = -2.956*10^6*r^2 + v_{fluidmax}$$

v_{fluid} = fluid velocity ($m.s^{-1}$)
r = tube radius (m)
$v_{fluidmax}$ = maximum stream velocity ($m.s^{-1}$)

The flowrate Q ($m^3.s^{-1}$) = $2\pi\int rv(r)dr$ from -r to r i.e. -5mm to +5mm
and $Q = A*v_{average}$

$v_{average}$ = fluid average velocity ($m.s^{-1}$)
A = cross sectional tube area (m^2)

$$\text{Thus } v_{average} = (2\pi\int rv(r)dr)/A$$

Air average velocity is shown graphed against air supply pressure in Figure 4.9. Velocity is seen to rise steeply with supply pressure. It can be seen that the air velocity tends to a maximum as a function of pressure. This maximum is limited by the nature of the flow within the apparatus. Figure 4.9 also shows that the particle velocity is lower than the gas velocity, this difference increasing with increasing gas supply pressure.

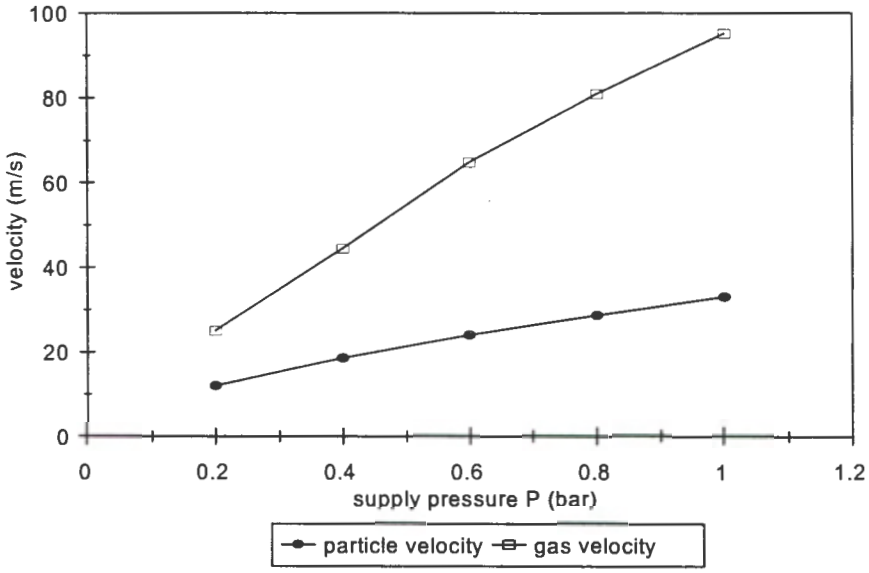

Figure 4.9 : Particle and gas velocity vs supply pressure for 106-125 μm SiC particles at a flux of 2.5 kg.m^{-2}.s^{-1}, illustrating the difference between gas and particle velocity (1 bar = 1 atmosphere of pressure above atmospheric pressure i.e. 2.026x10^{5}N.m^{-2}).

4.10.2 Measurement of the particle velocity

The determination of the particle velocity as a function of air supply pressure was found by using the double disk method as developed by Ruff and Ives [99], over a range of mass fluxes (mass flux = mass feed of particles from the erodent feed mechanism / cross sectional area of down tube).

The results for a flux of 2.5kg.m^{-2}.s^{-1} are plotted against supply pressure in Figure 4.10. Following the method of previous researchers [100,101] a linear regression (as shown in Figure 4.10) was initially performed on these results to obtain a straight line relationship between the particle velocity and the air supply.

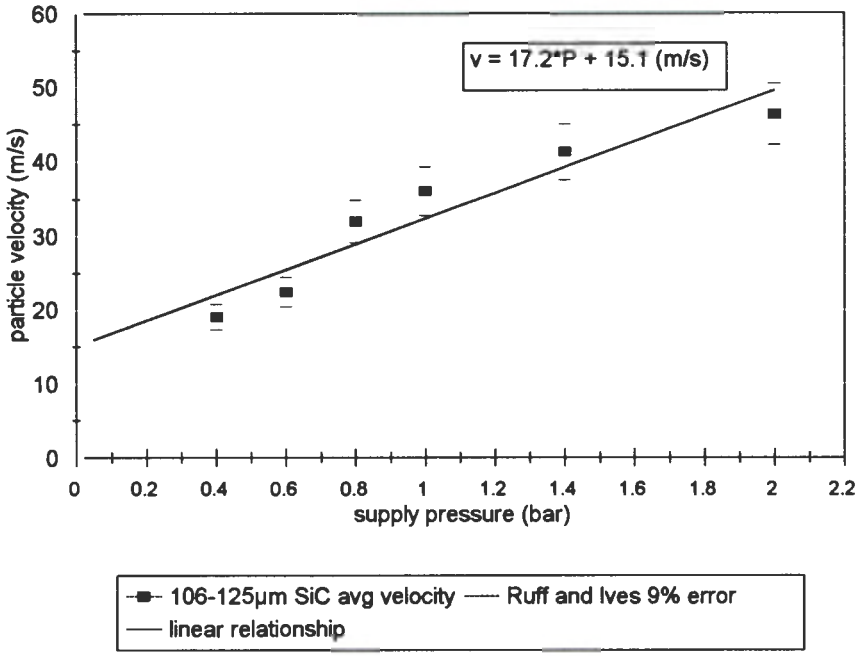

Figure 4.10 : Particle velocity of 106-125 µm SiC at a flux of 2.5kg.m^{-2}.s^{-1} vs air supply pressure at 20°C.

i.e. for P > 0.2 bar,

$$v_{particle} = 17.2*P + 15.1 \ (m.s^{-1})$$

$v_{particle}$ = particle velocity ($m.s^{-1}$)

P = air supply pressure (bar, where 1 bar = 1 atmosphere of pressure above atmospheric pressure i.e. $2.026 \times 10^5 N.m^{-2}$)

It can be seen from Figure 4.10 that if the straight line through the data points is extrapolated back towards the origin, it would intersect the y - axis at a value greater than zero. This is clearly incorrect, as it would imply that erodent particles could flow in the system without any air passing through. Further experiments were performed at lower and higher air pressures in order to obtain a more accurate relationship between the particle velocity and the air supply pressure.

The complete range of data obtained with air pressures between $1.418 \times 10^5 N.m^{-2}$ and $3.039 \times 10^5 N.m^{-2}$ using silicon carbide as the erodent particles is shown in Figure 4.11 together with the relationship that was determined between particle velocity and air supply pressure.

$$\text{If } \mathbf{v_{particle} = k*P^{np}}$$

$$\text{then } \mathbf{\ln(v_{particle}) = \ln(k) + np*\ln(P)}$$

where :

k = a constant

np = the particle velocity exponent

Hence if $\ln(v_{particle})$ is plotted against ln(P) then np can be found from the slope of the resulting straight line and used in the relationship $v_{particle} = k*P^{np}$. The constant is then exp(y-axis intercept).

Experimental error as opposed to experiment data scatter was determined by partially differentiating the variables in the equation used to derive velocity from the Ruff and Ives double disk calibration method. The maximum error was determined to be ± 9%.

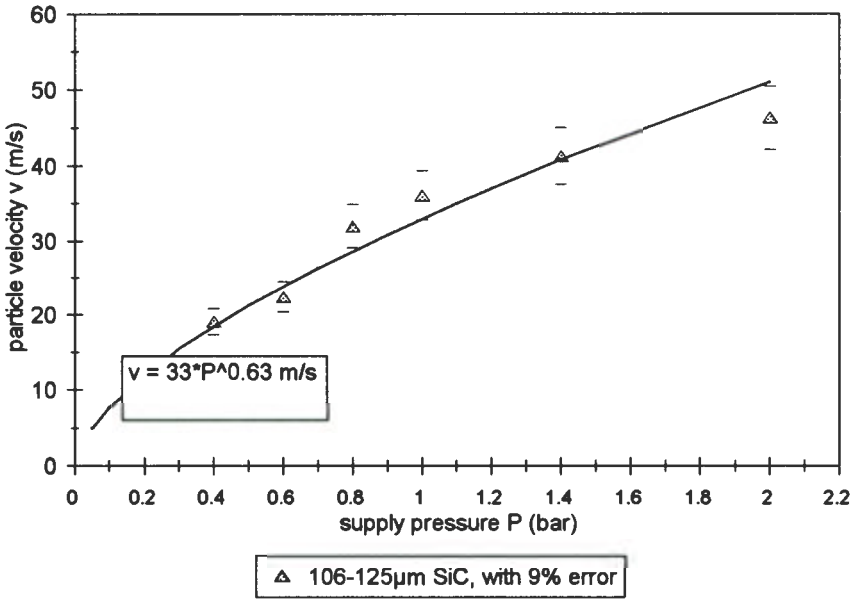

Figure 4.11 : Particle velocity vs air supply pressure for 106 - 125 µm SiC particles at 20°C. An exponential relationship passes through the points which is a more satisfactory fit than the previous straight line graph.

There was initially some concern that there would be a change in particle velocity with a change in mass flux due to the amount of interference between the particles increasing with increased flux. However, tests showed that particle velocity is independent of particle flux which is evidenced in Figure 4.12. In this series of experiments, particle fluxes ranging from 0.20kg.m^{-2}.s^{-1} to 9.8kg.m^{-2}.s^{-1} were tested. Despite there being almost two orders of magnitude difference between the smallest and largest flux, no distinct trend relating particle flux to velocity can be seen. This is an opinion shared by Shipway and Hutchings [26].

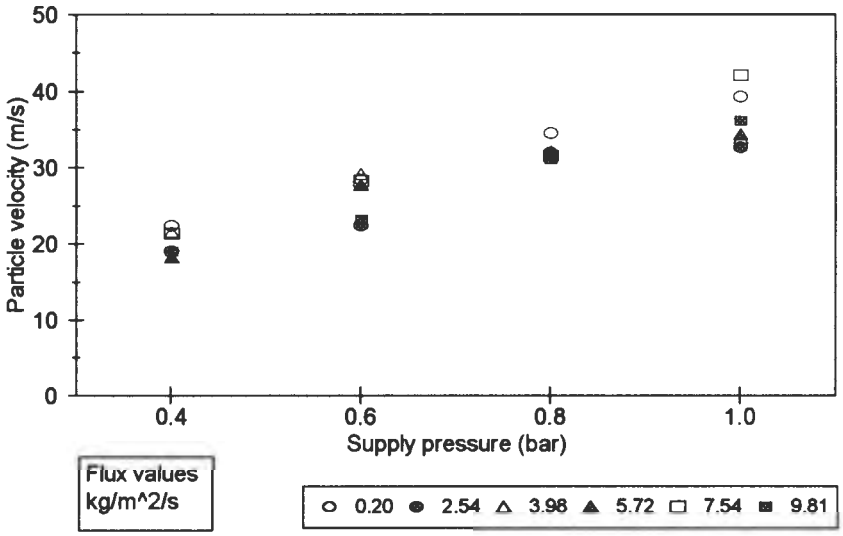

Figure 4.12 : Particle velocity of 106-125 μm SiC particles vs supply pressure for various fluxes, showing no clear relationship between flux and velocity despite the wide range tested.

4.11 Determination of the necessary mass flux to achieve similarity between plant and apparatus

Mass flux is calculated in the gas blast apparatus by dividing the mass feedrate of erodent by the cross-sectional area of the exit nozzle. Mass flux has also been defined as the mass feed rate of erodent particles divided by the area of the erosion crater on the target material [26]. However there is less error and less time involved in measuring the cross sectional area of the exit nozzle than in measuring the eroded scar. Hence for reasons of simplicity and accuracy, the former definition is adhered to.

It is clearly necessary to obtain the range of fluxes which operate in practice. However, the derivation of these fluxes can be approached in two ways.

The first approach is the most simple, and, in retrospect, yields the most useful result.

Approach (1) :

From boiler performance figures, the total air into the furnace and the fly ash load can be obtained, both in units of $kg.s^{-1}$.

For a 640MW unit at 100% MCR (Maximum Continuous Rating) total air in to the boiler is 609.2 $kg.s^{-1}$.

The fly ash load in a similar boiler under the same conditions is 32$kg.s^{-1}$ (which equates to 146 tons per hour [24].

For a boiler cross section of just less than 15x15m the mass flux at this point is approximately :

32/188 = **0.17$kg.m^{-2}.s^{-1}$**

The mass fraction of the eroding particles in the gas stream can then be derived.

i.e. Fly ash load / total air (approximately) = 32/609.2 = 5.3% by mass.

Approach (2) :

The second approach uses the mass fraction of fly ash in the boiler to calculate the erodent mass flow rate in the erosion test apparatus by multiplying it by the apparatus air mass flow rate.

The air mass flow rate is determined using a fluid dynamics approach in which a compressible fluid expands from a reservoir to atmosphere. In this case the reservoir was the compressed air supply, expanding to atmosphere through the nozzle of the acceleration tube [92]. The mass flow of the air was derived for a particular pressure setting (pressure controls the particle velocity) and the erodent mass feed rate found by taking 5.3% of the air mass flow rate.

A summary of the derived mass flow figures using experimentally derived average air velocity figures appears in Table 4.4.

Supply pressure Bar	Supply pressure (in SI units) $N.m^{-2} \times 10^5$	Mass Flow of air $kg.s^{-1}$	Avg. air velocity (at room temperature) $m.s^{-1}$
0.40	1.418	0.0042	44
0.60	1.621	0.0061	65
0.80	1.823	0.0076	81
1.00	2.026	0.0090	95

Table 4.4: This table relates the supply pressure of the compressed air to the mass flow of the air as well as its velocity as it is discharged from the acceleration tube nozzle.

The erodent mass feed rate required to fulfil the 5.3% of gas mass flow rate criterion is shown in Table 4.5 together with the mass flux derived from the erodent mass flow rates.

Supply Press bar	Supply pressure (in SI units) $N.m^{-2} x10^5$	Avg. air vel $m.s^{-1}$	Ero. feed $g.s^{-1}$	Mass flux $kg.m^{-2}.s^{-1}$
0.40	1.418	44	0.223	2.84
0.60	1.621	65	0.323	4.11
0.80	1.823	81	0.403	5.13
1.00	2.026	95	0.477	6.07

Table 4.5 : This table shows the necessary erodent feedrate to fulfil the 5.3% of air mass flowrate requirement.

In this analysis it is assumed that there is no mass flow rate change of the air conveying the particles since the specimen is only 20mm from the end of the acceleration tube nozzle. This distance is not sufficiently great enough to give the air opportunity to mix with the combustion gases.

Although Approach (2) is mathematically sound, it overlooks the fact that the erodent particles in the experimental apparatus are not at the same velocity as the fluid stream. This is shown from independent rotating double disk tests which determine particle velocity, compared with pitot tube tests performed to test the fluid velocity. This phenomenon is also noted by other researchers [31,91].

Thus, if mass flux is derived by taking a percentage of the mass flowrate of the fluid stream, the assumption is automatically made that the particles attain the same velocity as the gas. This results in mass fluxes an order of magnitude higher than found in Approach (1). This will lead to wear rates which are not representative.

Thus, the most reliable representation or simulation of mass fluxes experienced in coal fired boilers is that shown in Approach (1). i.e. **$0.17 kg.m^{-2}.s^{-1}$**.

4.11.1 Similarity of flow between plant and apparatus conditions

Similarity of operation between plant and experimental apparatus cannot be judged solely in terms of particle fluxes and velocities since the nature of the gas and particle flow also needs to be examined in order to establish experimental credibility. Unfortunately, geometric similarity cannot be obtained in the laboratory, as the apparatus dimensions are quite different to a full sized pulverised fuel boiler plant. However, dynamic similarity is achieved in both systems if the Reynolds' number exceeds 30 000. In this case the flow is fully turbulent.

The Reynolds number Re is defined as :

$$\mathbf{Re = \rho * v * D/\mu}$$

ρ = gas density
v = gas velocity
D = hydraulic diameter
μ = gas dynamic viscosity

Considering two extremes in laboratory apparatus operation :

1. Cold operation
2. Hot operation

1. Gas temperature = 300K (Cold operation)
   hence ρ = 1.18 $kg.m^{-3}$
   and Re = 1.93×10^5 i.e. > 30 000

2. Gas temperature = 900K (Hot operation)
   hence ρ = 0.392 $kg.m^{-3}$

and Re = 3.03×10^4 which is close to 30 000.

This second Reynolds number can be compared to the number obtained by Gibson [19] using a model geometrically similar to a boiler plant.

Gibson's Reynolds number Re = 2.77×10^4 (cold model)

The **plant** Reynolds number Re = 3.78×10^4 (hot operation)

It is was concluded therefore that dynamic similarity between the apparatus and plant had been achieved.

4.11.2 Measurement of the particle velocity at high temperatures

All of the initial particle velocity tests using the Ruff and Ives method were performed by bench mounting the preheat chamber, venturi and acceleration tube in existing room temperature erosive wear test apparatus. It was originally planned to use a similar method of velocity calibration as per Shipway and Hutchings [26] i.e. an optoelectronic device which, using two pairs of infra-red emitters and detectors, is able to time particles over a fixed distance. However, the difficulties of operating this device at high temperatures precluded the use of this design.

It was thus decided to continue using the Ruff and Ives device for velocity calibration, albeit in modified form, in situ at high temperatures. The configuration of the modified device is seen in Figure 4.13. The shaft to which the disk is attached had to be extended, as the motor could only be run outside the specimen chamber due to the high temperature inside. Space was also restricted. The disk was fixed at a stand-off distance of 20mm, the same as the specimen. The disk was made smaller than in the room temperature apparatus in order to fit into the narrow confines of the chamber. In addition, it had four slots machined in the top disk to allow eight marks to be made in one run as opposed to the two marks when only one slot is present. It was felt that this would improve the

accuracy of measurement, as each particle velocity quoted for a specific temperature is the result of eight readings.

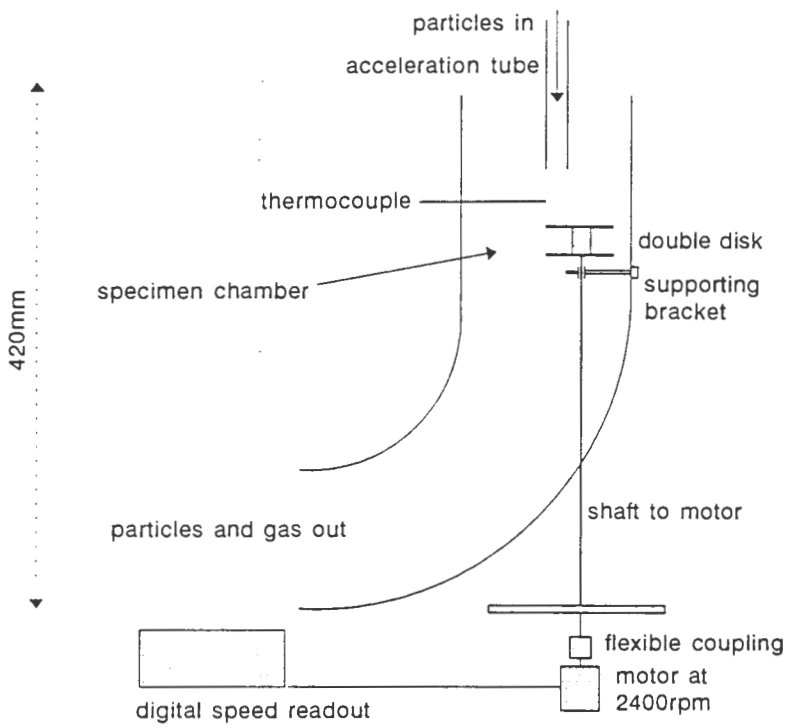

Figure 4.13 : The configuration of the modified Ruff and Ives device to fit into the specimen chamber of the high temperature erosion apparatus to calibrate particle velocity at high temperatures.

Problems were encountered with this device : Firstly, a bracket supporting the shaft close to the disk with a bronze journal bearing seized as soon as the temperature of the specimen chamber exceeded 250°C. The journal was bored out to give a larger tolerance for the silver steel shaft. However this worsened the situation, as vibration then occurred. This vibration again lead to seizure which was evidenced by noticeable fretting marks on the journal. The bronze bearing was subsequently replaced with a graphite bearing which was self lubricating over the range of temperatures. It thus became possible to run the Ruff and Ives device at 2400rpm for indefinite periods. However this test period was never more than 60 seconds once the apparatus had reached the desired operating temperature.

The rotating disk resulted in a deleterious flow effect when the rig was run at high temperature. The effect was not noticeable, however, when the lowest gas regulator pressure setting was used. At the maximum temperatures, the spinning disk caused a blockage effect [102] when a large volume of combustion gases was being passed through the specimen chamber. This caused dangerous random flame flashbacks placing a definite ceiling of approximately 325°C on the maximum test temperature at which velocity calibration was possible.

The results of the velocity calibration with increasing temperature is shown in Figure 4.14 and listed in Table 4.6. Although there is a scatter of 1.48m.s^{-1} (5.71% at 24m.s^{-1} particle velocity), there is no distinct trend of increasing velocity with increasing temperature. This was a surprising result as it was expected that as the air density decreased with increasing temperature it's velocity would increase to maintain a constant mass flow rate. This increase was in turn expected to result in an increase in particle velocity. The decrease in air density with temperature is shown in Figure 4.14 along with the particle velocity calibration. It was thus concluded that the particle velocity remains constant over the range of test temperatures.

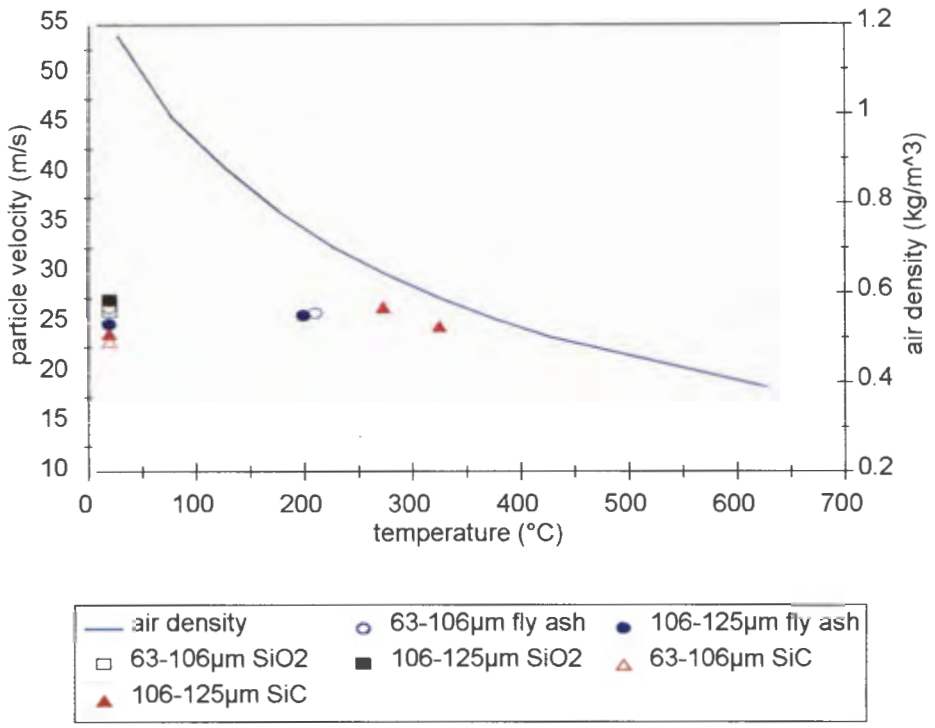

Figure 4.14 : Particle velocity vs air temperature showing no distinct trend of increasing particle velocity with decreasing air density.

	Particle Velocity ($m.s^{-1}$) 63-106µm	Particle Velocity ($m.s^{-1}$) 106-125µm
Erodent : Fly ash		
20°C	26.60	24.90
200°C	26.00	25.75
Erodent : SiO_2		
20°C	26.25	27.35
200°C	-	-
Erodent : SiC		
20°C	23.2	24.0
273°C	-	26.6
325°C	-	24.7

Table 4.6 : A comparison of the particle velocity with the test temperature, showing a scatter of values but no upward trend from low temperature to high.

4.12 A comparison of the final performance and the design requirements

Table 4.7 compares the final performance of the apparatus compared to the initial design requirements. The working pressure of the apparatus is marginally higher than atmospheric owing to there being no induced draught as originally planned. The working temperature ranges from 20°C to a maximum of approximately 619°C and can be held for a maximum of 45 minutes before the gasket material in the apparatus begins to deteriorate rapidly. The temperature range quoted of 20°C to 619°C is only attainable at a particle velocity of 24m.s^{-1} (i.e. 0.6 bar of air supply pressure) as the higher velocities result in a greater mass of cool air flowing through the system requiring more heat than is available. A maximum temperature of 450°C is attainable at the highest particle velocity of 51m.s^{-1}.

Variable description	Variable range required	Variable range achieved
Working pressure	90 kPa (absolute)	greater than atmospheric
Working temp.	20 - 600°C	20 - 619°C, though only > 600 at 0.6 bar of air
Erodent velocity	10 - 40 m.s^{-1}	24 - 51 m.s^{-1}
Erodent mass flux	5 - 20 % by mass of gas flow	0.3 - 15 % of apparatus gas flow, however, 5% by mass plant conditions are simulated
Erodent type	plant fly ashes	any erodent may be used
Erodent particle size	20 - 150µm	63 - 250µm
Operating time / run	30 minutes	25 minutes / high temperature run excluding warmup time

Table 4.7 : The design requirements are compared with the final performance figures achieved in this table.

Velocities range from 24m.s^{-1} to a maximum of 51m.s^{-1}. Erodent velocity is greater than required at the high end of the range. It is not, however, possible to get lower than 24m.s^{-1} without the apparatus overheating. The issue of achieving similarity in terms of particle mass flux between plant and laboratory has been discussed in the literature review and will

not be repeated here. However it can be assumed that the required mass fluxes have been achieved, with the required erodent types.

The particle sizes to be employed can be any size greater than 63-106μm range. This is due to flow problems with particles smaller than 63μm, particularly with plant fly ash.

Finally, the time restriction of 25 minutes is placed on operation of the apparatus in conditions of the highest achievable temperatures, at an air supply pressure of 0.6 bar, and a gas regulator pressure of 120 kPa (see Figure 4.8). This is to avoid overheating and rapid deterioration of the gasket material in many sections of the apparatus. The apparatus has been run for up to one and a half hours continuously at more moderate conditions of 0.6 bar of air and 40 kPa of gas.

5. Experimental Methods

5.1 Materials tested

5.1.1 Steels

Several low carbon, high strength low alloy steels that are commonly used for boiler tubes were tested. These are shown in Table 5.1.

BS 3604	Sub-classification	DIN equivalent	ISO 2604 equivalent
HFS 620-440	1Cr ½Mo	13CrMo44	TS 32 Cat IV
HFS 622	2¼Cr 1Mo	10CrMo910	TS 34 Cat IV
HFS 660	½Cr ½Mo ¼V	14MoV63	TS 33 Cat IV

Table 5.1: Standard equivalents of the tested steels.

The HFS660 and 622 were only used in the initial testing of the apparatus. The HFS620 was used as the standard material for the remaining erosion tests. A full breakdown of the nominal chemical analyses of the steels is shown in Table 5.2.

BS3604	C %	Si	Mn	P	S	Cr	Mo	Fe
HFS 620-440	0.10-0.15	0.10-0.35	0.40-0.70	0.030	0.030	0.70-1.10	0.45-0.65	bal
HFS 622	0.08-0.15	0.50	0.40-0.70	0.030	0.030	2.00-2.50	0.90-1.20	bal
HFS 660	0.10-0.15	0.10-0.35	0.40-0.70	0.030	0.030	0.30-0.60	0.50-0.70	bal

Table 5.2 : Composition range of the HFS range hot finished seamless (HFS) tube form adhering to BS3604, 1990.

All materials were received in plate form since it is not possible to machine erosion specimens out of boiler tubing. Specimen dimensions were 20mm wide, 6mm thick and 35mm long with a 1.9mm diameter hole drilled 4mm from the target surface to

accommodate a 1.5mm diameter K-type thermocouple. The specimen is backed by an insulating alumino-silicate fibre board mounted on the AISI 316L stainless steel specimen stage. Thus, the temperature registered by the thermocouple at this point is the uniform temperature of the specimen.

5.1.2 Electric arc sprayed coatings

Two electric arc sprayed thermal coatings that are commonly used as sacrificial protective layers for boiler tubes were also tested. Strips of HFS620 were cleaned and roughened by blasting with steel shot before being coated, to ensure good coating / substrate adhesion. The tested coatings and their nominal chemical composition and thickness are shown in Table 5.3.

	Composition	Thickness (μm)
Coating 1	43Cr 53Ni 4Al	100
Coating 2	26.5Cr 67.75Fe 5.75Al	100

Table 5.3 : A list of the tested coatings and their nominal chemical compositions.

5.2 Solid particle erosion testing

5.2.1 The erodents

Three erodents were used in this work namely : fly ash, silicon carbide (SiC), silica sand (SiO_2). Fly ash is a complex material as it consists of several different majority elements which in turn exist in several different mineral forms. Although the chemical composition of different fly ashes is similar, a range of mineral contents is seen. This is illustrated in Table 5.4.

Element	Average across 8 samples (%)	Mineral species	Range across 8 samples (bal. = glassy phase) (%)
Si as SiO_2, Al as Al_2O	56	Mullite ($3Al_2O_3.2SiO_2$)	15-50
Si as SiO_2	25	Quartz (SiO_2)	2.5-25
Fe as Fe_2O	5	Haematite (Fe_2O_3)	2.5-8.5
Ca as CaO	5	Lime ($Ca(OH)_2$)	0.3-3.0

Table 5.4 : A list of the range of the chemical and mineralogical makeup found in an xray florescence and xray diffraction analysis of eight South African fly ashes showing consistency of chemical composition, but variability of mineralogy.

Eight ashes were obtained in total to perform comparative erosivity tests. However, only one fly ash from a single coal fired power station, which had been collected over a period of time at fairly consistent conditions of boiler load, was used in the examination of the effects of different erosion variables. This ash was collected over four months on eight different occasions at similar conditions of boiler load and from the same electrostatic precipitator. The minimum and maximum loads at the time of collection were 172 and 198 MW. It was thus considered that the ash gathered was a reasonable representation of the fly ash mineralogy and morphology from this particular power station.

In addition to any compositional variation, the morphology of fly ash varies from angular to spherical particles. Particles which are agglomerations of spheres, or spheres and angular particles, create difficulties during the sieving of ash into the desired test size ranges. The bond between the agglomerated particles is not strong which causes them to separate when vibrated and sieved. Thus the sieve pores quickly become clogged. A related problem is the ash flowability when introducing particles into the apparatus. The complex shapes become interlocked and result in arching and bridging across any flow regulating orifice.

The unsieved ash spanned a size range of 5 to 250μm. A size distribution of the fly ash used is shown in Figure 5.1. This was sieved in ranges of < 38μm, 38-63μm, 63-106μm and 106-125μm. Approximately 10 kg of ash was sieved which was extremely time consuming; with the result that only a limited amount of the 106-125μm was procured for comparative testing due to the small volume fraction (5.5%) of this size range in the coal ash sample.

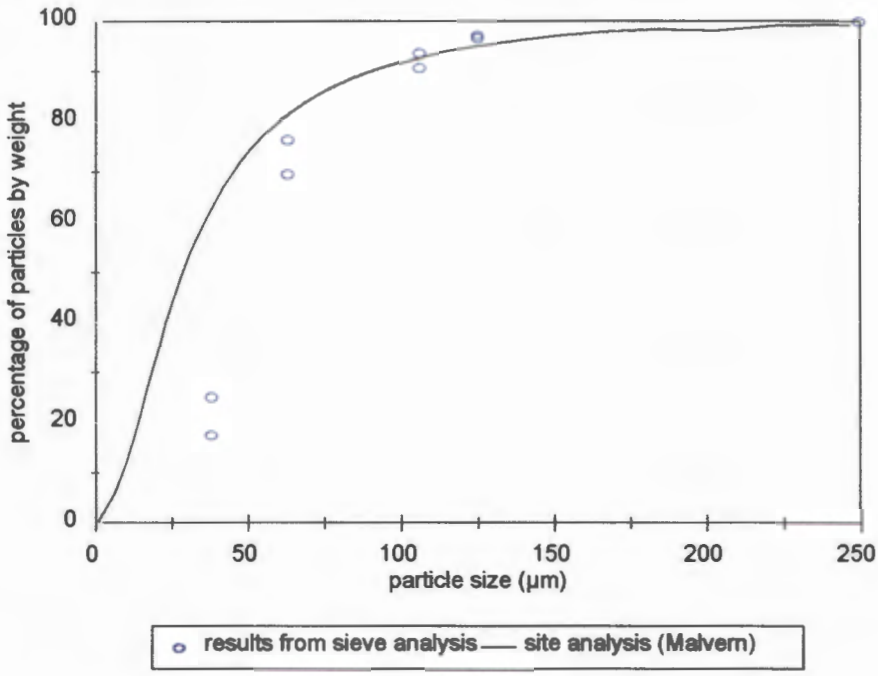

Figure 5.1 : A size distribution of the plant fly ash used in erosion testing.

The scope of the ash testing was thus limited, due to difficulties experienced in :

a) procuring a representative sample,

b) sieving the sample to obtain sufficient amounts of erodent,

c) developing a method to introduce the ash into the erosion apparatus (as described in section 4.5).

Thus commercially available SiC and SiO_2 particles were employed in the test matrix to ascertain whether their behaviour was similar to that of fly ash which might allow future work to be conducted using either erodent as an ash substitute. SiC and SiO_2 are plentiful, easily sieved and flow under gravity. The erodents were sieved prior to testing within the size ranges required which were 63-106μm (220 grit) and 106-125μm

(120 grit) using a *Fritsch* vibratory sieving device and *Kingtest* stainless steel sieves. The sieves were cleaned between tests by using a soft brush to remove particles wedged in the sieve apertures.

5.2.2 Specimen preparation

The specimens were ground with a diamond wheel to R_a = 0.5μm and then further polished using a 600 grit abrasive paper to R_a = 0.05μm prior to an erosion test. During initial room temperature erosion work, ground specimens were used to obtain mass loss data. However, there was a protracted period before these ground specimen surfaces recorded steady state mass losses. All specimens were subsequently ground and polished following machining, using the method described.

Initially, specimens were normalised for 60 minutes at 800°C and then given a similar surface grinding treatment as the as received specimens. The erosion resistance of the normalised specimens was then compared with the as received specimens. However, since no difference in erosion resistance was found between the two groups, all subsequent tests were conducted using the as received specimens.

Coated specimens were tested in the as received state. All of these samples had an extremely rough surface profile due to the shot blasting of the parent material prior to coating application. Any mechanical grinding and polishing of these coatings tended to expose peaks of the substrate. Thus, the recording of erosion rates using polished coated surfaces would not give an accurate reflection of the erosion resistance of the coating itself. Consequently, erosion testing of these specimens was carried out on the original as received surfaces.

5.2.3 The standard method of conducting high temperature erosion tests

The specimens were ultrasonically cleaned in alcohol for two minutes, dried and then weighed on a *Sartorius* digital balance scale to an accuracy of 0.01mg before being placed in the apparatus. The specimens were left in the apparatus until the

temperature had stabilised to within ±15°C of the control temperature for tests conducted above ambient temperature. This took from 10 minutes at the lower end of the temperature scale, to 30 minutes at the top end of the scale.

After blasting with the erodent, the specimen was allowed to remain in the specimen chamber until it was cool enough to be handled by the operator (with Kevlar gloves, the handleable temperature is approximately 200°C) which took approximately 10 minutes at the highest temperatures.

Initially, a single dose of erodent was used to achieve a mass loss from which an erosion rate was obtained. The motivation for this was based on work performed at high temperature by Chinnadurai & Bahadur [90] who used only one run using 100g of erodent from which an erosion rate for the sample was obtained by dividing its measured mass loss by the mass of erodent.

However, it was found in this work that a steady state mass loss was only recorded following an initial dose of erodent. This was evident in room temperature tests, as well as at the higher temperatures. This effect is seen can be seen in Figure 5.2, which graphs cumulative mass loss versus cumulative mass of erodent at 20 and 500°C respectively.

A representative erosion rate can only be obtained by taking the slope of a best fit line through the data points as opposed to taking the slope of the line joining the last data point to the origin. Joining the last data point to the origin can underestimate the erosion rate by 22 to 35% based on the results shown in Figure 5.2.

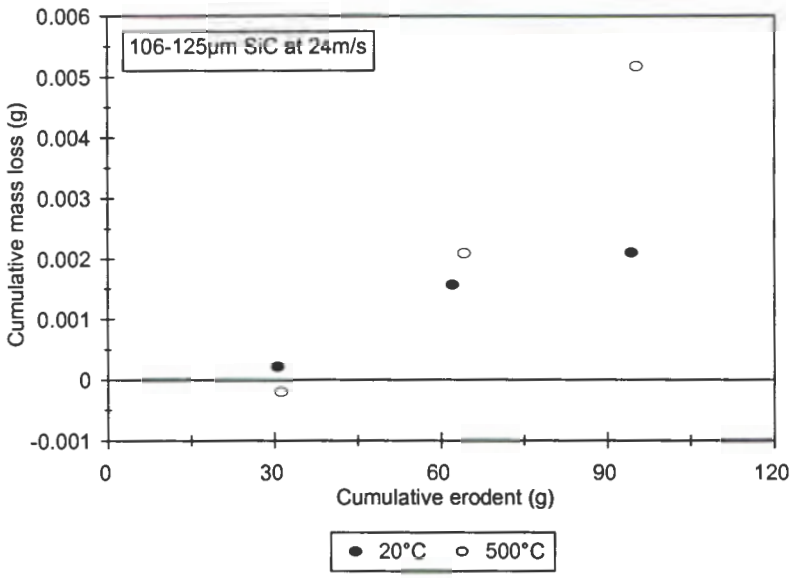

Figure 5.2 : Graph of cumulative mass loss vs cumulative mass of erodent for a 20°C and a 500°C run.

Hence, the approach that was subsequently taken was to give the specimen a large initial erodent dose of 60g prior to being cleaned and weighed to give a starting mass. The specimen was then eroded up to three more times with 30g of erodent charge and the erosion rate calculated by determining the constant from a linear regression of the cumulative mass loss versus cumulative erodent data, which is in effect the slope of a best fit line through these points. The experimental error is thus quoted as the error of the constant in the linear regression.

The mass loss per gram of erodent is converted to volume loss by dividing by the density of the steel :

$$E = m'/\rho$$

where m' = constant from the linear regression of the cumulative material mass loss versus cumulative erodent data.

and ρ = density of the steel

Erosion tests were conducted using the three different erodents to quantify differences in erosivity as a function of temperature. Velocity tests were conducted for 4 different

velocities ranging from 24-51m.s^{-1} using 106-125μm fly ash, SiO_2 and SiC particles. Particle flux tests were conducted using 106-125μm SiO_2 over a range which spanned nearly two orders of magnitude between the smallest (0.17kg.m^{-2}.s^{-1}) and the largest flux (8.4kg.m^{-2}.s^{-1}).

During all of the tests the angle of the target remained constant at 40° for the following reasons. The apparatus was originally designed to use fly ash of less than 100μm diameter as the sole test erodent. Coal ash particles are spherical in appearance below a size of 38μm and consists of agglomerations of spheres in addition to some angular particles between 38-106μm. Since Sundararajan [43] showed that the angle at which maximum wear takes place for spherical particles to be 40°, it was believed that this angle would be appropriate for this work. However, testing was also performed on room temperature apparatus to test the effect of angle on erosion rates of the HFS620 steel using fly ash and SiC. The angles tested ranged from 20 to 90°. A summary of the test conditions is seen in Table 5.5.

Test type	**Erodent**		
	Fly ash	**SiO_2**	**SiC**
Velocity (m.s^{-1})	24 (at room temperature only) 33 41 51	24 (across range of temperatures) 33 41 51	24 (across range of temperatures) 33 41 51
Flux (kg.m^{-2}.s^{-1})	0.17 (across range of temperatures)	0.17 (across range of temperatures) 2.1 3.5 8.4	0.17 (across range of temperatures) 2.1
Temp range (°C)	20-600	20-600	20-600
Size ranges (μm)	63-106 106-125	63-106 106-125	63-106 106-125
Spec. Orientation	40° (across range of temperatures)	40° (across range of temperatures)	40° (across range of temperatures)

Table 5.5 : A summary of the test conditions used to complete the erosion testing.

5.3 Microscopy

5.3.1 Optical microscopy of cross-sectioned specimens

Worn specimens were cross-sectioned and mounted in epoxy resin in order to perform a metallurgical examination and conduct microhardness tests. Specimens were sectioned through the centre of the erosion crater and after polishing on a 0.25μm diamond impregnated felt pad were etched in 2.5% Nital solution to reveal their microstructure. All specimens were viewed in a *Reichert MeF3A* light microscope.

5.3.2 Scanning electron microscopy of eroded surfaces

Worn specimens were ultrasonically cleaned in ethanol followed by isopropanol before being mounted on aluminium stubs with a conductive carbon-containing glue. The specimens were specifically designed / dimensioned to allow for a fast transfer from the erosion apparatus to the *Cambridge S200* scanning electron microscope. The worn specimens were viewed at 25kV as this setting yielded micrographs with a good resolution.

5.3.3 Scanning electron microscopy of erodent particles

The erodent particles were also examined using the scanning electron microscope. Particles were mounted on aluminium stubs with a conductive carbon-containing glue and were clad with gold - palladium to ensure electrical conductivity. Particles were viewed at a 20kV potential difference, as they became electrostatically charged at settings higher than this resulting in considerable florescence.

5.3.4 Transmission electron microscopy

Transmission electron microscopy was used to view the extent of subsurface deformation of eroded specimens. Thin foils from the damaged specimens were prepared in the following way :

1) A square section was cut from the scar area and milled from the rear into a tile 12mm x 12mm x 0.85mm thick.
2) The erosion crater was coated with approximately 100μm of *Lacomit*, a proprietary lacquer. This was to protect this surface from any damage during the ensuing grinding process.
3) The tiles were ground using a 600grit SiC abrasive paper to a thickness of 200μm. Disks of 3mm diameter were then punched out of the tiles.
4) The disks were ground to a thickness of 80-120μm with a 1200grit SiC abrasive paper. The *Lacomit* coating was removed at this stage by gently grinding the eroded surface smooth.
5) A 10% by volume perchloric acid and methanol solution was used as the etchant in the subsequent electropolishing process.

Specimens were electropolished in a *Struers Tenulpol-3* jet polisher at a potential difference of 30V and a current of 0.2A. The etchant temperature was held at between -10°C and -20°C using a dry ice and ethanol mixture.

Transmission electron microscopy was carried out on a *Jeol 200CX* at an accelerating voltage of 200keV using a single tilt specimen holder.

5.4 Microhardness testing

5.4.1 Microhardness testing of worn specimens

Microhardness tests were conducted as a function of depth below the damaged surface on a selection of worn surfaces using a *Matsuzawa MXT α7* digital microhardness tester. The cross-sectioned specimens were mounted in epoxy resin, parallel faced and then automatically polished on a *Struers Rotopol-22* to ensure a flat face for good quality hardness indentations. A Knoop indentor was used for the readings at a load of 25 gf. The Knoop indentor yielded better quality results than the Vickers' indentor as the width of the indent is wider leading to less error in measurement.

Three readings were taken at depths of 10, 20, 50, 100, 150μm etc, until a constant hardness was reached. Care was taken to space individual indents at least three diagonals away from each other so readings were not affected by the plastic zone surrounding an indentation. The average of the three readings at each specific depth was then plotted against depth to determine the extent of plastic deformation below the surface.

5.4.2 Microhardness testing of the erodent particles

Microhardness tests were conducted on the erodent particles which had been mounted in epoxy resin. The *Matsuzawa MXT α7* digital microhardness tester was also used for these tests. However, a Vickers indentor at 100gf was favoured here, as the width of a flat section of erodent particle surface is small and it is important for the entire indentor to make an impression on the particle.

Microhardness was difficult to measure, particularly of the fly ash particles, as they consist mainly of two different mineral species and a glassy phase which results in a wide scatter of hardness values. The hardness measurements were conducted on 106-125 μm particles only.

5.5 Tensile testing

5.5.1 Characterisation of the test material performance at high temperatures

Tensile tests were conducted on a *Zwick 1484* Universal Testing Machine using a vertical cylindrical alumina tube furnace to characterise the change in mechanical properties of the HF 620 steel as a function of temperature.

Tests adhered to the ASTM E25 1985 (standard recommended practice for elevated temperature tension tests of metallic materials), using specimens machined in the rolling direction according to ASTM E8M. This standard states that the time of holding the specimen at temperature prior to the start of the test should be governed by the time necessary to ensure that the specimen has reached thermal equilibrium. Otherwise the test should not take less than twenty minutes.

The strain rate was 10^{-4} s^{-1} and the preload 150 N. The temperature of the furnace was controlled by a *Eurotherm* thermostat receiving feedback from a K-type thermocouple which was positioned next to the specimen. Another K-type thermocouple gave continuous feedback via a *Boston Technologies PC73A* card to a personal computer which could be logged or displayed or both.

6. Results

6.1 The effect of different erodent type

6.1.1 Analysis of the plant fly ash prior to and post target impact

The ash in the 106-125μm size range consists of spheres, agglomerations of spheres as well as friable unburned or semi-combusted coal particles. This amalgamation of particle shapes is seen Figure 6.1 and Figure 6.2.

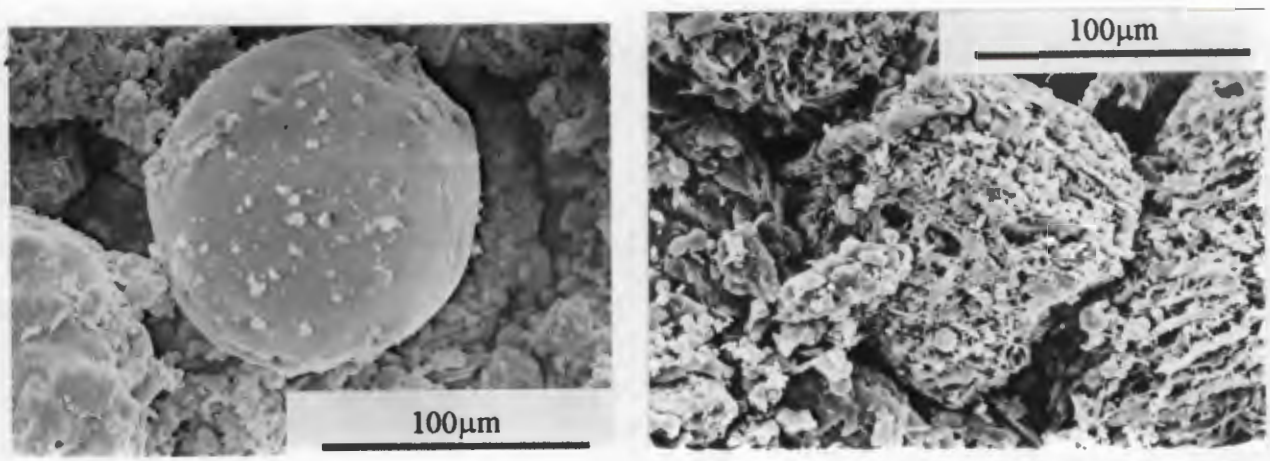

(a) (b)

Figure 6.1: Scanning electron micrographs of 106-125μm coal ash particles as used in erosion tests. (a) The spherical nature of fully developed ash particles is clearly evident. (b) This micrograph illustrates the fact that angular particles are also found in any one sample of this particular ash. These angular particles comprise of semi combusted pulverised fuel (i.e. coal) or quartz particles which have survived the combustion process.

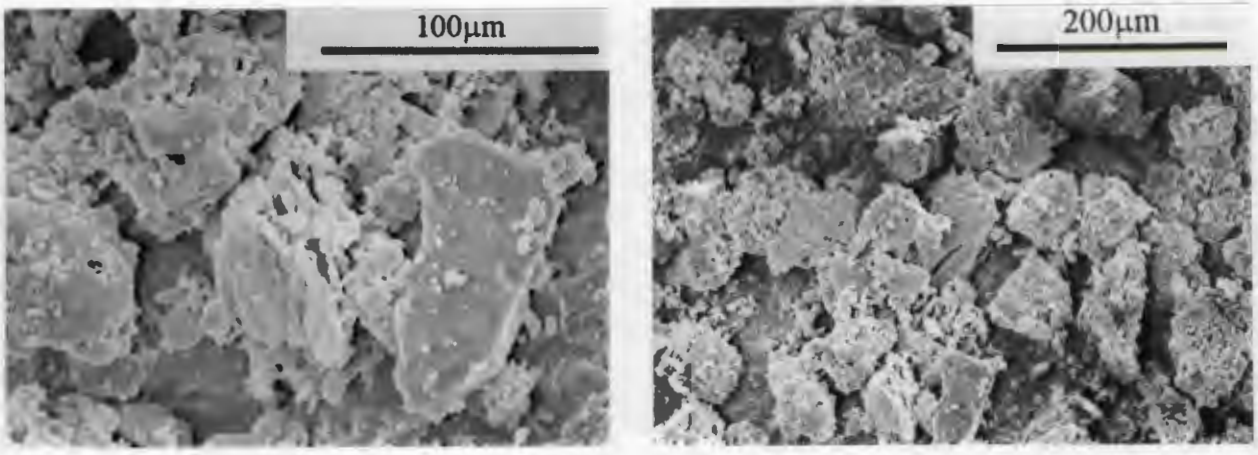

(a) (b)

Figure 6.2 : Scanning electron micrograph of 63-106μm ash particles as used in erosion tests. (a) A low magnification micrograph showing the mix of angular and spherical particles found in this size range. (b) Showing the mix of agglomerations of spherical particles and angular particles.

There is also evidence that the coal ash particles fragment on impact, which is seen in Figure 6.3(a). The fractured particle can be compared to an intact particle prior to impact in Figure 6.3(b). There was no difference in post impact particle appearance as a function of temperature. Figure 6.3(a) shows a fly ash particle recovered after tests run at 500°C using an as received plant coal ash that was graded in the 150-250μm size range. It can be seen by the flat featureless fracture surface that the particle has failed in a brittle fashion. Clearly part of the particle's energy would have gone into the fracture process rather than damaging the target surface.

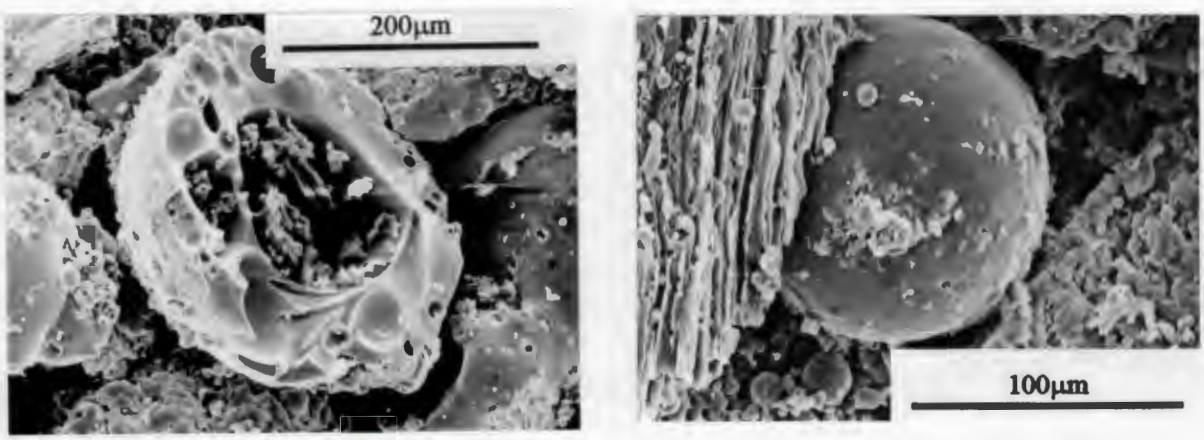

(a) (b)

Figure 6.3 : (a) A damaged coal ash particle following specimen impact at temperature >500°C. (b) Coal ash prior to impact.

6.1.2 *Differences in erosive wear rates between different power plants*

An attempt was made to correlate the erosive wear rates of a boiler tube steel using coal ash particles from eight different local power stations with their quartz content. These erosion tests were conducted at a particle velocity of 72m.s^{-1} to ensure high wear rates and a high particle mass flux of 6.6kg.m^{-2}.s^{-1} in room temperature erosion apparatus. Eight coal ashes in the size range of 106-125µm were tested.

Due to their mix of shapes, coal ash has a high angle of repose which was measured to be 47°. Angle of repose is defined as the angle between the horizontal and the side of a cone formed when pouring a powder on to a flat surface. This can be linked to the minimum angle of a chute that particles will flow down under the influence of gravity for a given chute material and chute material surface finish. Coal ash particles also form arches when their flow is restricted by a controlling device such as a valve or an orifice. This causes flow stoppages. The only way to maintain ash flow was thus to use a steep sided chute, with a large orifice to control flow. This resulted in high particle mass flow rates, and hence the high particle flux of 6.6kg.m^{-2}.s^{-1}. The results from this testing are seen in Figure 6.4 where the ranked erosion rates of the eight ashes are compared with their percentage quartz content.

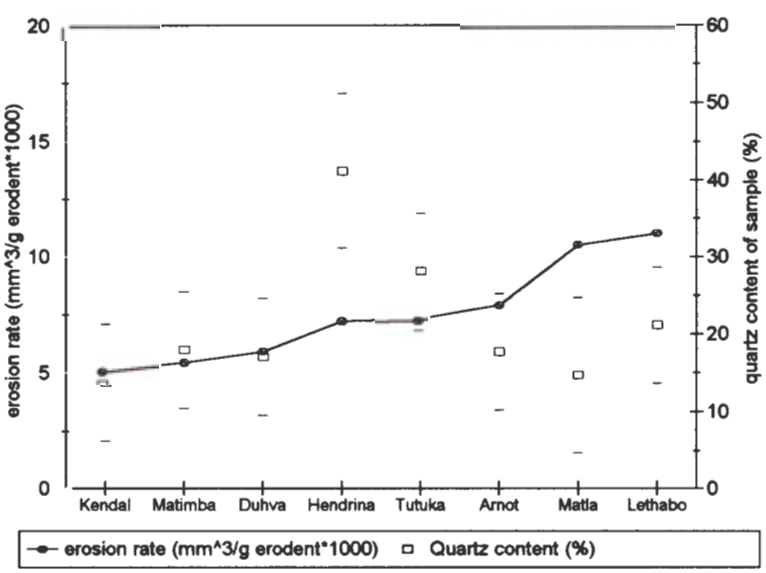

Figure 6.4 : Graph of erosion rate and quartz percentage content in eight different South African power stations.

Although there is a 100% increase in the erosion rate between the least erosive and most erosive ash tested in the same conditions of particle velocity and flux, this increase did not appear to be directly related to the measured quartz content of these ashes. The ash with the noticeable highest quartz content (Hendrina power station) as determined by quantitative xray diffraction (XRD) fell in the middle of the erosivity ranking. This test result was exaggerated by an estimated 20% error to the interference by an unidentified compound. However, even were this result is excluded, an upward trend in erosion rate with increasing quartz content cannot be discerned within the experimental error of the XRD results.

6.1.3 Analysis of the SiC and SiO_2 particles prior to and post impact

The SiC particles seen in Figure 6.5(a,b) have angular, faceted surfaces, and there are no obvious surface defects. The SiO_2 particles shown in Figure 6.6(a,b) have a more rounded appearance than the SiC, with porosity evident on the surface.

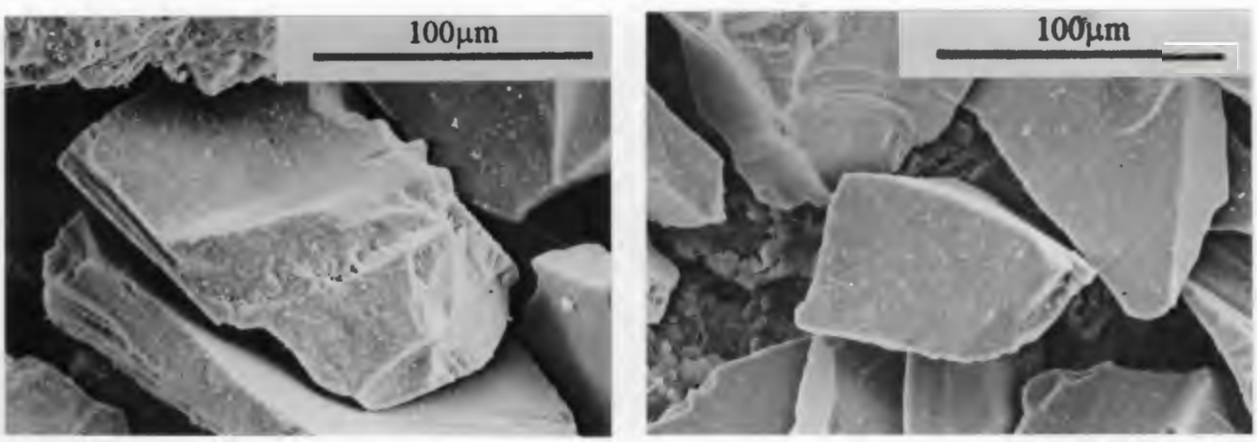

(a) *(b)*

Figure 6.5 : (a) Scanning electron micrograph of 106-125µm SiC particles as used in erosion tests. (b) 63-106µm SiC particles. Note the angularity of the particles and their smooth faceted surfaces.

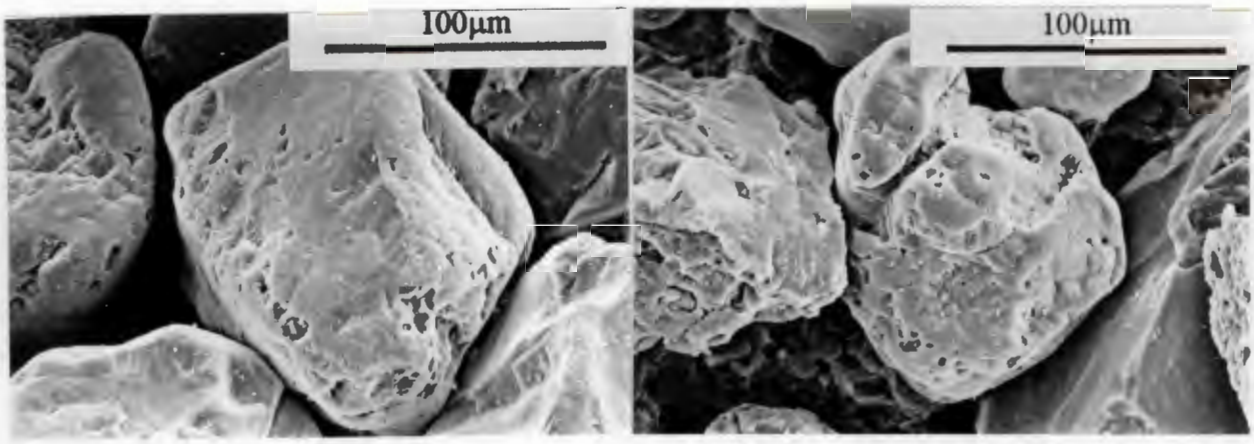

Figure 6.6 : (a) Scanning electron micrograph of 106-125μm SiO_2 particles as used in erosion tests. (b) 63-106μm SiO_2 These particles have a more rounded appearance, and do not have the smooth faceted surfaces that the SiC particles do. A number of inconsistencies can be seen such as pores and nodules. The difference in structure between these particles is evidenced in the microhardness test results.

Although there are no gross visible changes to the SiO_2 and SiC particles after impact, particles collected after tests conducted across a range of temperatures show that sharp edge protrusions have been chipped off upon impact. This is seen in Figure 6.7(a,b) which shows fresh fracture surfaces on these particles. No differentiation in particle appearance as a function of temperature was observed.

Metallographic analysis of the specimens impacted by SiC particles show isolated sites where the edges of particles have been chipped off during impact and remained embedded in the material. This is seen in Figure 6.8 and confirms the observations made of the SiC particles post impact.

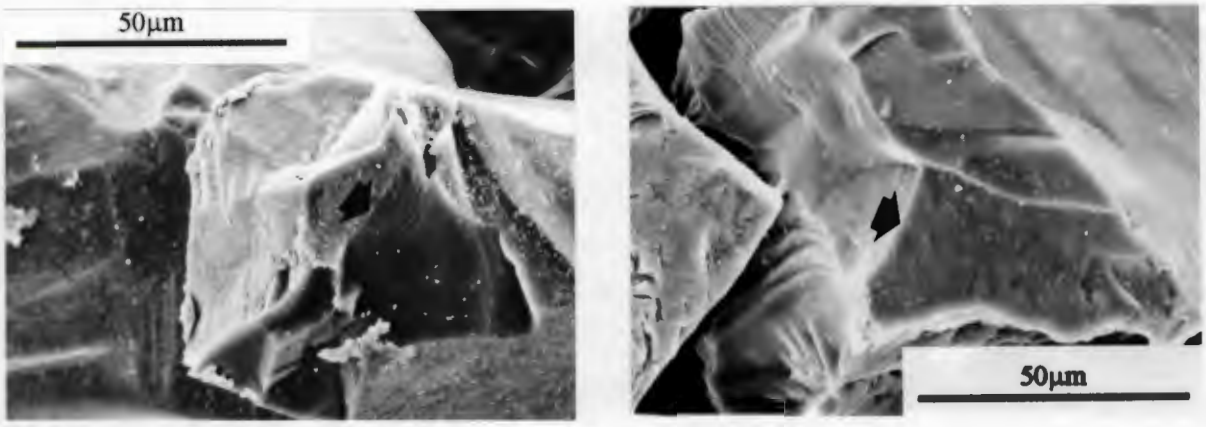

(a) (b)

Figure 6.7 : (a) A SiC particle showing a fresh fracture surface where a corner has chipped off. (b) An SiO_2 particle also showing a fresh fracture surface where an edge has chipped off

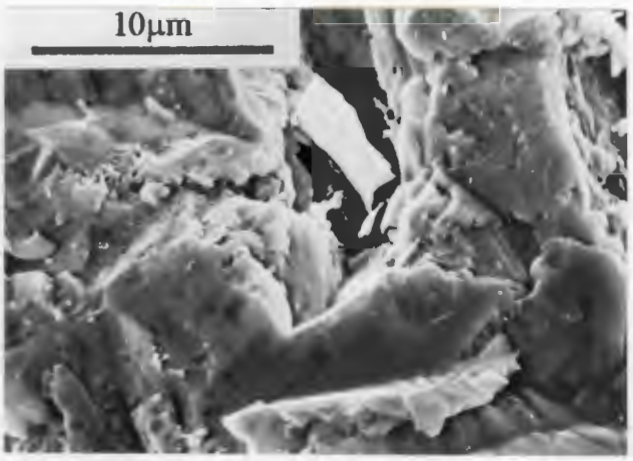

Figure 6.8 : Evidence of a SiC chip lying embedded in the target surface.

6.1.4 The effect of temperature on erosion wear rates for fly ash, SiC and SiO_2

The effect of temperature up to 550°C, on the erosive wear of a 1Cr½Mo steel using different erodents is shown in Figure 6.9. Both silicon carbide (SiC) and silica sand (SiO_2) particles (106-125μm) result in a marked increase in the wear rate of the steel with an increase in specimen temperature. This increase becomes particularly noticeable above temperatures of 300°C. The wear rate using SiC and SiO_2 particles is 12% greater at 300°C than at room temperature. However the rate at 500°C is 130% greater than that at room temperature. The SiC and SiO_2 particles appear to have similar erosivities over the range of temperatures investigated.

The erosion rate when using plant coal ash in a similar size range increases only 31% from room temperature to 500°C.

These comparative tests were conducted at a particle velocity of 24±2 $m.s^{-1}$ at a particle mass flux of 0.17-0.23 $kg.m^{-2}.s^{-1}$. Mass flux in this work is the mass flow rate of the erodent into the system divided by the cross sectional area of the erodent carrying tube.

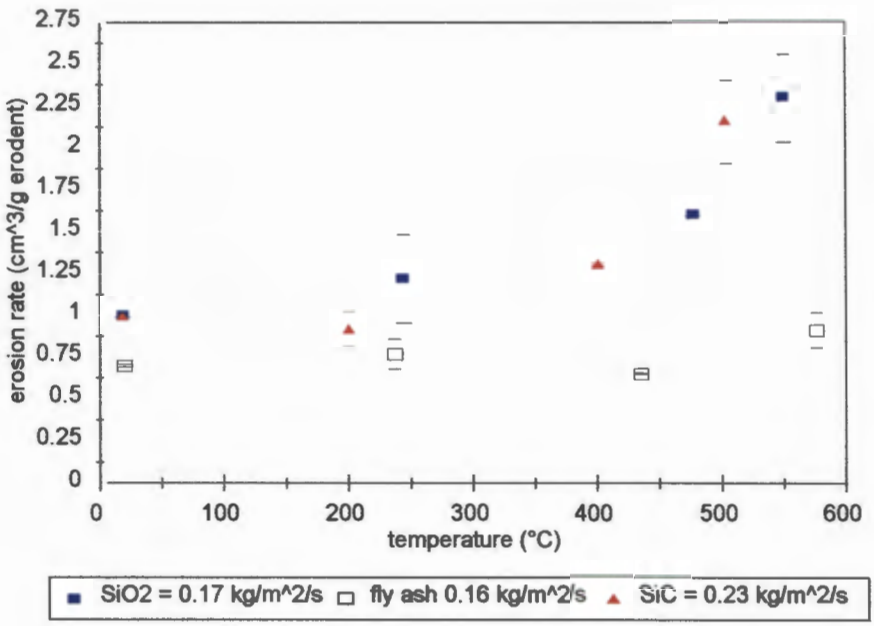

Figure 6.9 : Graph showing differences in particle erosivity at a constant particle velocity 24 ± 2 $m.s^{-1}$ and a particle flux between 0.16 and 0.23 $kg.m^{-2}.s^{-1}$. SiC and SiO_2 particles cause similar damage across the range of tested temperatures, whilst the coal ash particles cause 75% of the damage from SiC and SiO_2 at room temperature, and only 36% at 550°C.

The smaller diameter 63-106µm SiC and SiO_2 particle also cause similar erosion rates in the same conditions of particle velocity and flux. Although it would seem as if the SiC particles cause more wear, this is within the data scatter. Figure 6.10 shows that the erosive wear rate for the boiler tube steel increases by approximately 45% at 300°C and 230% at 550°C compared to the room temperature wear rate for both erodents. These increases are higher than those recorded for the larger erodent particles (106-125µm) at a similar velocity of 24$m.s^{-1}$. However it should be noted that the particle flux

was much higher for the smaller size at 0.96kg.m^{-2}.s^{-1}. The effect of particle flux on erosion rates is discussed in detail later.

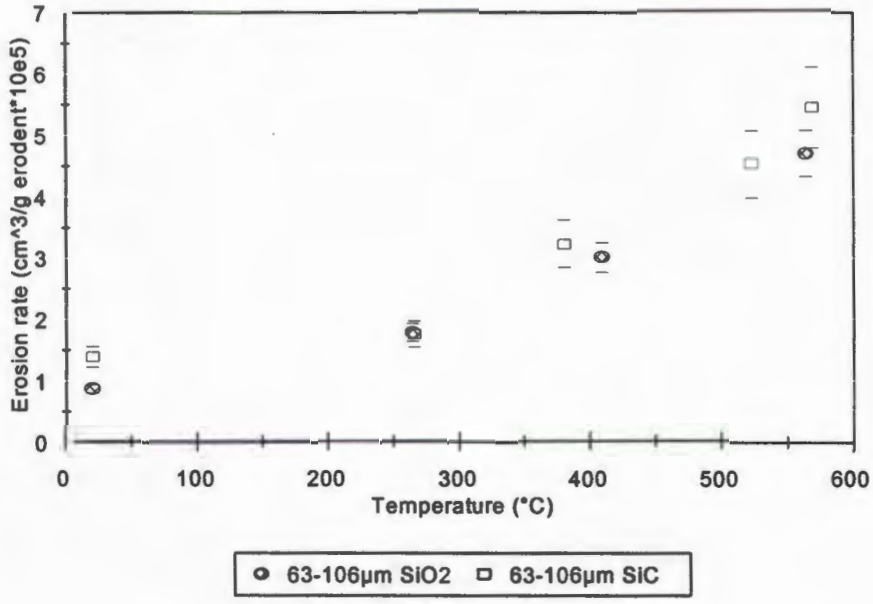

Figure 6.10 : Graph of erosion rate versus specimen temperature for 63-106 µm SiO_2 and SiC particles which reproduces the trend seen in the larger size ranges of the different particles causing similar wear rates.

An analysis of the density and microhardness of the erodent particles was also conducted. Microhardness test results show SiC particles to have the highest average hardness of 2481 HV 100gf as seen in Table 6.1. This is in agreement with Sheldon and Kanhere [29]. The SiO_2 particles have a lower average hardness value of 1374 HV 100gf whilst the fly ash has the lowest hardness of 976 HV 100gf.

Particle	Density $g.cm^{-3}$	Hardness HV	hardness std deviation	hardness range
SiC	3.24	2481	426	2144-3386
SiO_2	2.88	1374	390	715-1892
FA	1.99	976	608	446-1951

Table 6.1 : Particle density, hardness, with the large variation in the hardness results also shown. This variation is particularly noticeable with the coal ash particles.

Thus despite the SiC being 1.8 times harder than the SiO_2 particles, they nevertheless cause erosion of a similar magnitude. These hard particles cause similar amounts of deformation, which eventually results in similar material mass loss. The coal ash particles which have an average hardness of only $976kg.mm^{-2}$ compared with the $2481kg.mm^{-2}$ of the SiC, cause only 75% of the damage caused by SiC or SiO_2 particles at room temperature and 36% at 550°C.

This minimal increase in erosion rate is thought to be due to the softening of the glassy phase in the ash with temperature which lowers its erosivity [6]. The softening point of an alumino-silicate glass is defined as the point at which the glass will deform under its own weight and is approximately 915°C. The silicate rich glassy phase in fly ash however, begins melting from 815°C. Thus softening of the glassy phase in the ash could be expected from lower temperatures. The fact that the erosion rate does not actually drop off but climbs slightly is significant as it would indicate that the hard quartz particles which have a high melting temperature of 1500-1800°C are unaffected by temperature and are thus mainly responsible for the surface damage to the steel target. The mineralogy of the plant coal ash tested is shown in Table 6.2.

Mineral description : Hendrina power station	Percentage occurance : Quantitative XRD analysis (%)
Mullite : $3(Al_2O_3).2(SiO_2)$	39
Alpha quartz : SiO_2	41.2
Lime : CaO	
Anhydrite : $CaSO_4$	
Calcite : $CaCo_3$	
Hematite : α - Fe_2O_3	
Magnetite : γ - Fe_2O_3	0.7
Glass phase	19.1

Table 6.2 : A quantitative analysis of the plant coal ash used in this work (Hendrina power station).

6.1.5 The effect of erodent type on angle of maximum wear

106-125µm plant fly ash and 106-125µm SiC particles were tested across a range of angles to determine the angle of specimen inclination at which maximum wear took place. These tests were conducted in a room temperature apparatus at a particle velocity of 24m.s^{-1}. The fly ash particles caused a peak in erosive wear rate at approximately 40°, whilst the SiC caused a peak at approximately 20°. This can be seen in Figure 6.11 and Figure 6.12.

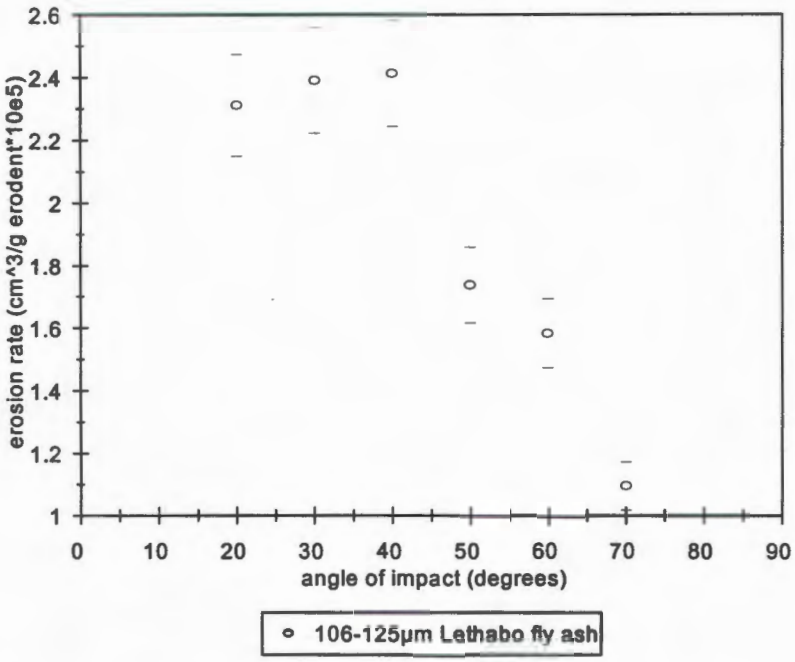

Figure 6.11 : Erosion rate vs angle of impact for a 106-125µm plant fly ash.

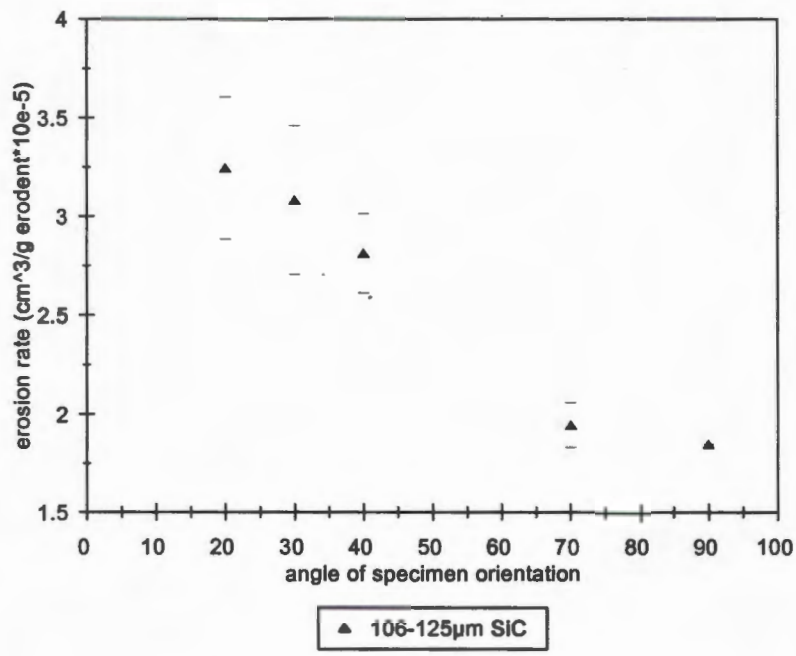

Figure 6.12 : Erosion rate vs angle of impact for a 106-125µm SiC.

6.2 The effect of different erodent size

Figure 6.13 shows the effect of two particle sizes on erosion wear rates for temperatures up to 550°C using SiC and SiO_2 particles. These size ranges were 63-106 µm and 106-125 µm. These tests were conducted at an impact velocity of 24±2 $m.s^{-1}$ and an average particle flux of 2.2 $kg.m^{-2}.s^{-1}$.

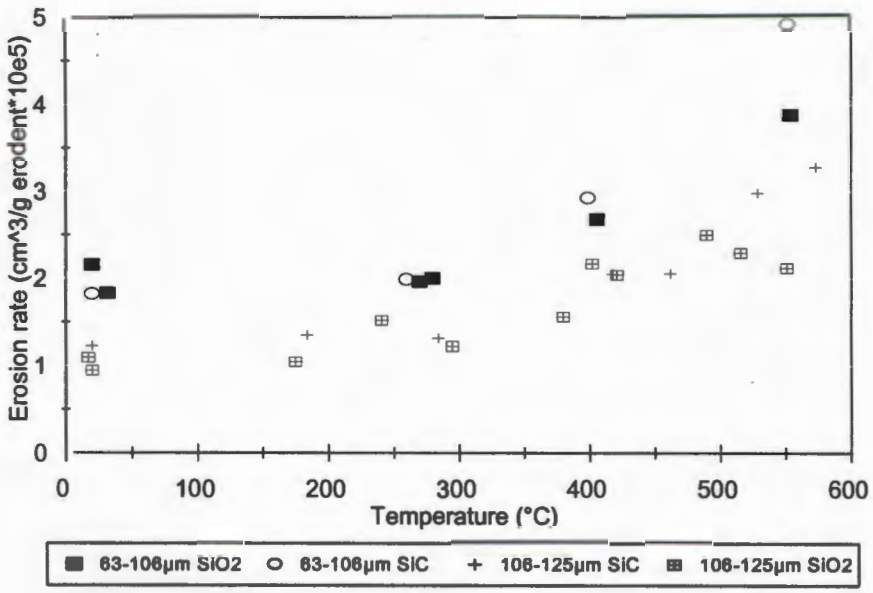

Figure 6.13 : Erosion rate versus temperature for Silicon Carbide and Silica sand particles in two different size ranges, all at a mass flux of 2.7kg.$m^{-2}.s^{-1}$. It can be seen from this graph how the 63-106 µm particles result in a higher erosion rate than the 106-125µm particles.

The results (Figure 6.13) clearly show that the smaller size particles (63-106µm) result in up to 100% more wear of the steel under such conditions compared to the larger sized particles (106-125µm). The rapid increase in wear rates above 300°C is seen in both the 63-106µm as well as the 106-125µm size range.

However, when testing 63-106µm and 106-125µm ash, the differences are not as marked. Indeed, the experimental error associated with testing the ash makes it difficult to distinguish which size is responsible for greater wear.

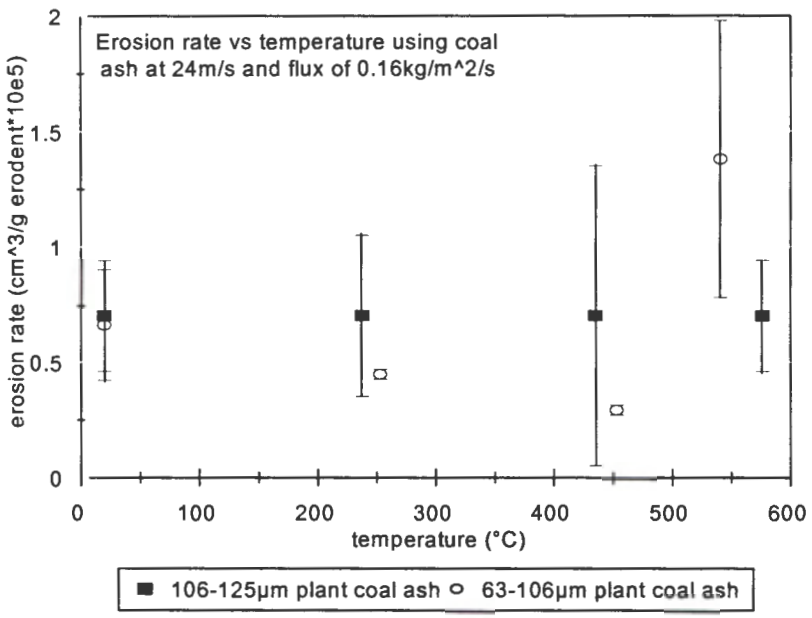

Figure 6.14 : Comparative testing of the 63-106µm and 106-125µm plant coal ash (Hendrina power station).

The wear surfaces of specimens eroded by 63-106µm and 106-125µm SiC particles were also examined. The surfaces of these specimens bombarded by 5g of SiC particles at $24m.s^{-1}$ and a flux of $0.17kg.m^{-2}.s^{-1}$, are shown in Figure 6.15(a) and (b) respectively. In addition, the particles used are shown at the same magnification above these micrographs in order to place the size of the damage sites and the size of the particles into perspective.

Impact sites which have not yet been struck by another particle(s) are clearly seen, as the edges of the crater or cut are still well defined. These strikes are likely to be those from the final particles passing through the system. The scanning electron micrographs were taken in the center of each specimen.

Eight 20x100µm rectangular segments in a 160x100µm area in the centre of the wear crater were examined. This equates to the exposure size of a scanning electron micrograph. Five photographs corresponding to an area of 80000µm^2 or 8% of 1mm^2 were examined. The length of each site was measured and the number of sites totalled. Approximately 50 counts were made per photograph for the 63-106µm particles and 25 for the 106-125µm particles. This equated to 245 and 115 counts respectively. The average number of strikes per 160x100µm area were multiplied by 62.5 to change the units to strikes per mm^2. The roughness of this area was also measured with a Talysurf surface profilometer. The results of this testing are shown in Table 6.3.

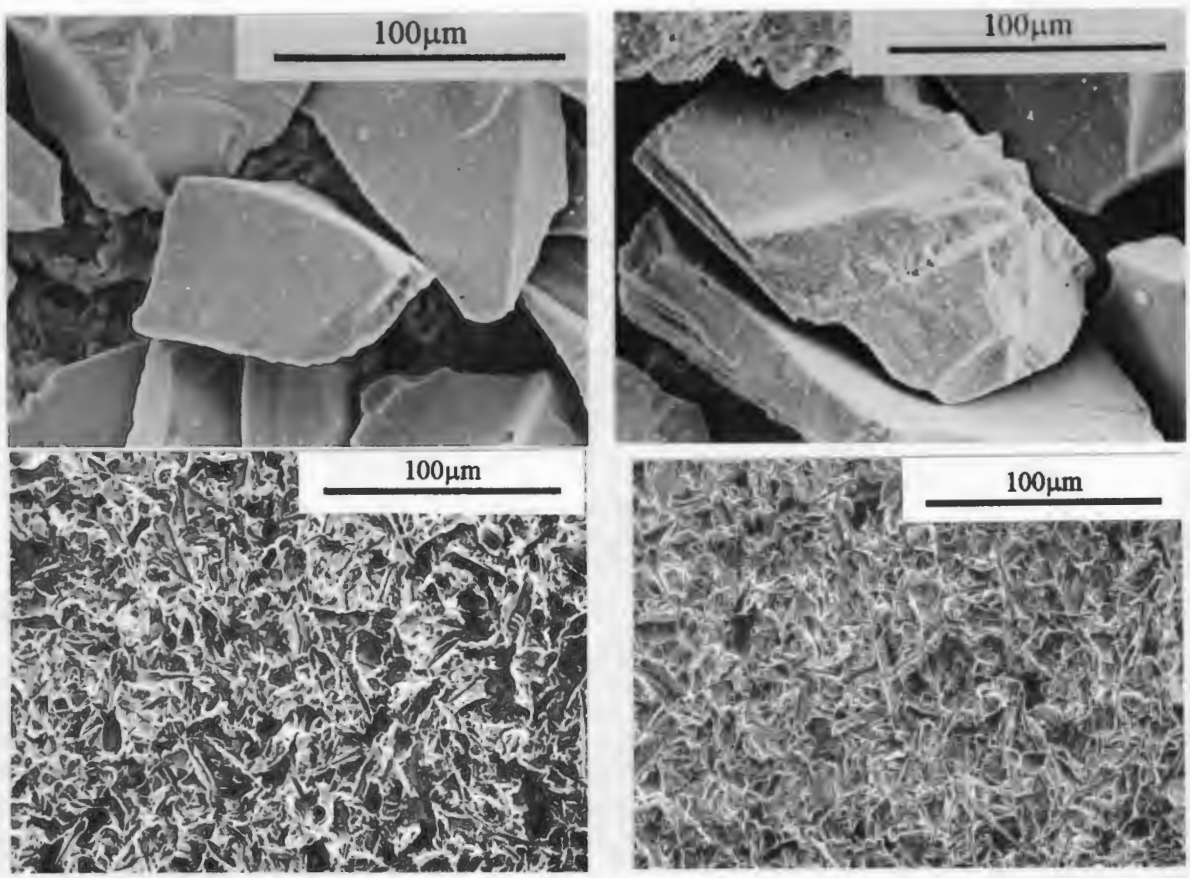

Figure 6.15 : Scanning electron micrographs of steel samples bombarded by a fixed mass (5g) of (a) 63-106 micron and (b) 106-125 micron SiC particles.

	Particle size 63-106μm	Particle size 106-125μm
number of strikes/mm^2	3063	1438
average length of damage site	10.12±4.03μm	21.72±6.18μm
maximum peak to valley roughness R_{ymax}	0.01	0.03
estimated number of particles in the 5g sample	6.1x10^5	2.4x10^5

Table 6.3 : Results of analysis of wear surfaces of specimens bombarded by 63-106 micron and 106-125 micron SiC particles.

It is estimated that there are 2.5 times more 63-106μm particles in a 5g sample than in an equivalent sample of the 106-125μm size range. Despite this, only 2.1 times more strikes are seen on the wear surface of the specimen. It is also seen that despite the average mass of a particle from the 106-125μm size range being 2.5 times greater than that of a particle from the the 63-106μm range, the length of the damage site they cause is on average only 2.1 times larger. This difference in impact site size also results in an R_{ymax} roughness 3 times greater for the 106-125μm particle damaged site than the 63-106μm particle damaged site.

Thus, fewer of the 63-106μm compared to the 106-125μm particles strike the centre of the target than are aimed at it. This implies that particles are being deflected by the gas flow, some perhaps not even striking the specimen. Although the 106-125μm particles are 2.5 times more massive the impact sites they cause are only 2.1 times larger on average. It is thus possible that the smaller particles slide and cut more, relative to the larger particles.

6.3 The effect of particle mass flux on erosion

The erodent chosen for an investigation in to the effect of particle flux on erosion rate with temperature was SiO_2 (106-125μm) because of the limitation imposed by the supply of ash of a consistent constitution.

All of the flux testing was performed at the same air pressure setting of $1.621 \times 10^5 N.m^{-2}$, which corresponds to a particle velocity of $24 \pm 2 m.s^{-1}$. It was established that there is no significant velocity variation over a range of fluxes tested from 0.20 to $9.8 kg.m^{-2}.s^{-1}$ (see section 4.2.2). A range of 0.17 to $8.4 kg.m^{-2}.s^{-1}$ was chosen for these erosion tests. A flux of $0.17 kg.m^{-2}.s^{-1}$ is the minimum required to achieve similarity with plant conditions (see section 5.3) whilst the flux of $8.4 kg.m^{-2}.s^{-1}$ is the maximum attainable when using the turntable feed device.

It is apparent from Figure 6.16 that the erosion rate indeed increases with a decrease in particle flux but only to a level where any further decrease in particle flux does not make significant changes to the overall erosion rate recorded.

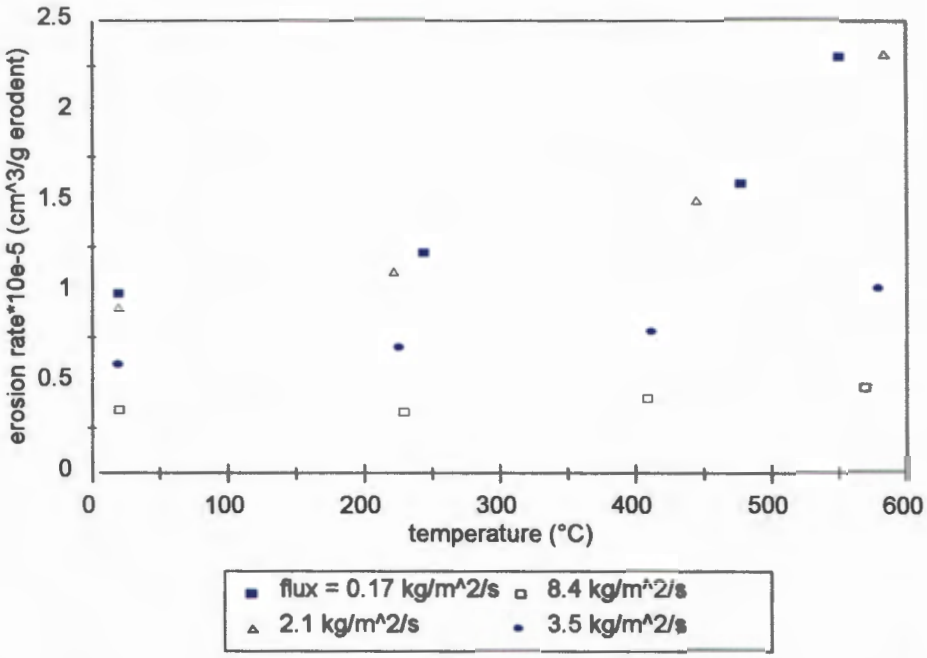

Figure 6.16 : Graph of erosion rate versus temperature for 106-125μm SiO_2 particles all at 24±2 $m.s^{-1}$, bombarding the HFS620 steel, at a fixed specimen orientation of 40°. Note how for all of the fluxes there is an increase in erosion rate with temperature, the lowest fluxes result in the highest erosion rates and the highest fluxes the lowest.

As the particle flux decreases from 8.4kg.m^{-2}.s^{-1} to 0.17kg.m^{-2}.s^{-1} the erosion rate increases by approximately 285% at room temperature from 0.354x10^{-5} cm^3/g erodent to 1.01x10^{-5} cm^3/g erodent. It should be noted however that a decrease in flux by 12.4 times from 2.1kg.m^{-2}.s^{-1} to 0.17kg.m^{-2}.s^{-1} increased the erosion rate by only 10%.

6.3.1 Oxidation of the specimens

Figure 6.17 shows the results of a comparison that was performed between mass gain due to oxidation and mass loss due to erosion. The steel samples were cleaned and weighed and then oxidised in a furnace for 6¾ hours in total to ensure an appreciable mass gain. The samples were then weighed to measure mass gain due to simple oxide layer growth. The mass loss due to erosion for an equivalent time period was

extrapolated from erosion rate data. The erosion rate data was taken from tests conducted at 24m.s^{-1} with 106-125µm ash, SiC and SiO_2 particles at a flux of 0.17kg.m^{-2}.s^{-1} on an HFS620 substrate.

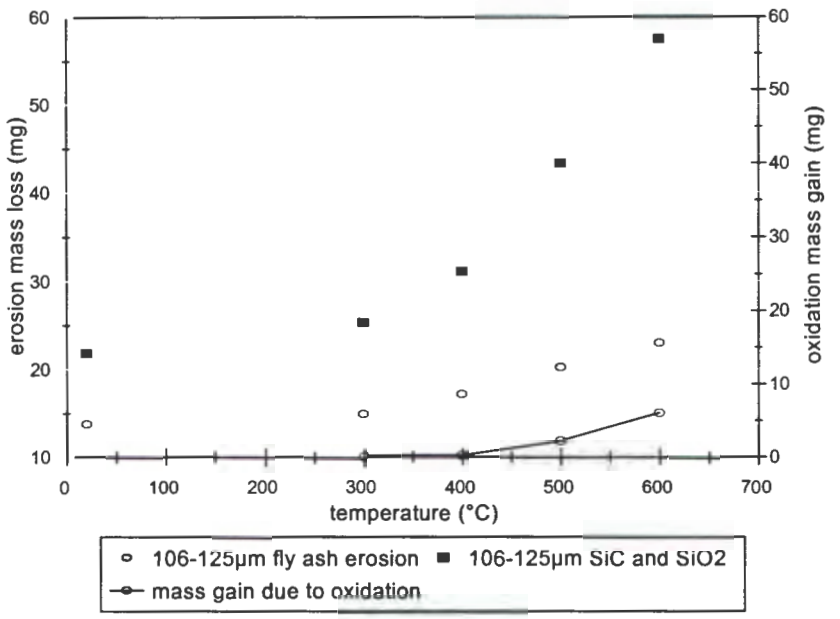

Figure 6.17 : Graph comparing the erosion mass loss to the oxidation mass gain for similar exposure times. The left hand primary axis shows the oxide mass gain whilst the right hand secondary axis shows the mass loss due to erosion.

It can be seen that mass loss due to erosion over the same time period as the specimens oxidised in a furnace is a substantially greater effect. At 500°C, the mass gain due to oxidation is 2.23mg compared with 20.26mg of mass loss due to erosion by ash and 43.29mg due to erosion by SiC and SiO_2. This is a difference of an order of magnitude. To compare the trends, the mass gain due to oxidation is graphed on the secondary (right hand) axis, whilst the mass loss due to erosion is graphed on the primary (left hand) axis.

6.4 The effects of particle velocity on erosion rates

The effects of velocity on erosion rates using fly ash as an erodent are shown in Figure 6.18. Due to the difficulties involved in obtaining sufficient quantities of the 106-125µm size range, tests were only conducted at room temperature. Testing was carried out at a flux of 0.21kg.m^{-2}.s^{-1} and the results cannot be directly compared to results obtained from SiC and SiO_2.which were conducted at fluxes of 2.3 and 2.1kg.m^{-2}.s^{-1} respectively.

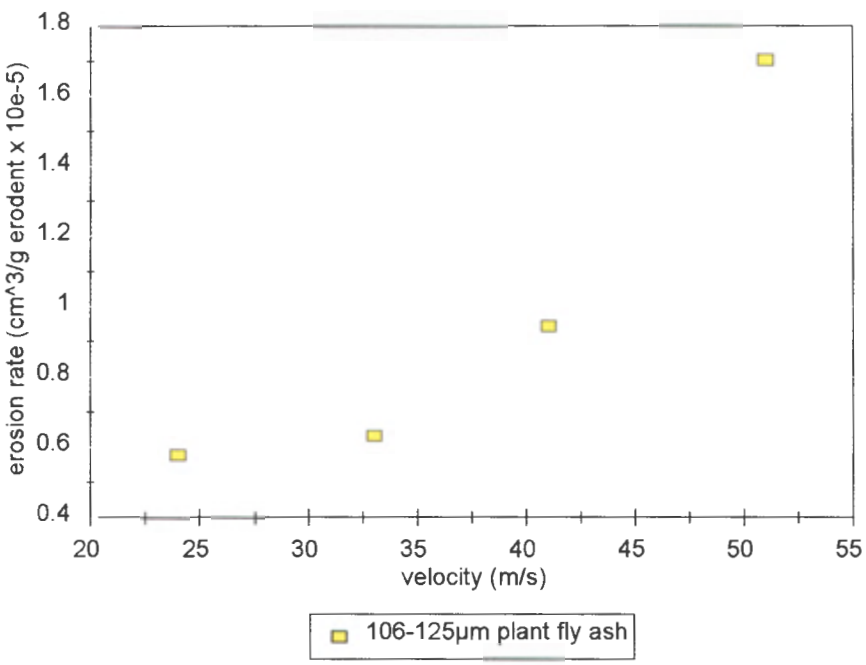

Figure 6.18 : Erosion rate vs particle velocity for a 106-125µm plant fly ash (Duhva power station) tested at room temperature only.

Figure 6.19 shows the erosion rate versus temperature using 106-125µm SiO_2 particles at different velocities ranging from 24±2 to 51m.s^{-1}. The average mass feed rate was 0.145g.s^{-1} which translates to a particle flux of 1.99kg.m^{-2}.s^{-1}. It is clear that there is an increase in the erosion rate with an increase in velocity from 24 to 51m.s^{-1}. At room temperature this increase is approximately 300%.

At a particle velocity of 24m.s^{-1} erosion rates remain constant until approximately 375°C whereafter they climb rapidly from 0.9cm^3/g erodent x10^{-5} to 2.3cm^3/g erodent x10^{-5}. At a particle velocity of 51m.s^{-1}, erosion rates remain constant up to 200°C whereafter they climb rapidly from 4cm^3/g erodent x10^{-5} to 6cm^3/g erodent x10^{-5} at 450°C. These periods of steady wear with temperature increase followed by a sudden increase in erosion rate at a critical temperature have not been previously reported. The same trend (see Figure 6.20) was found when performing tests using SiC particles.

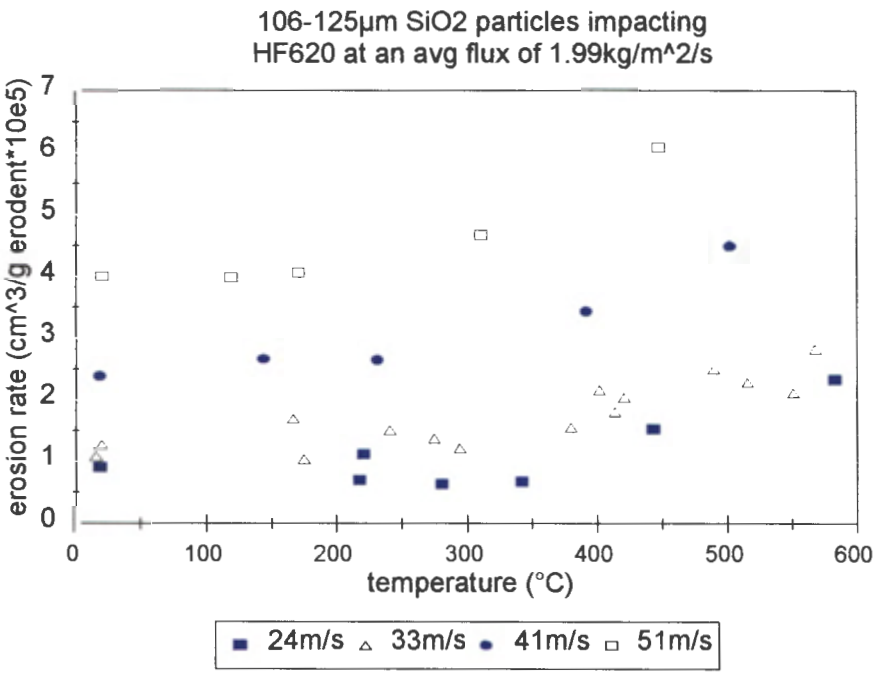

Figure 6.19 : Graph showing the results of 106-125µm Silica sand particles bombarding an HF620 steel at a fixed flux 2.1kg.m^{-2}.s^{-1} over a range of velocities. The trend of an increased wear rate with increasing temperature can be seen for all of the velocities.

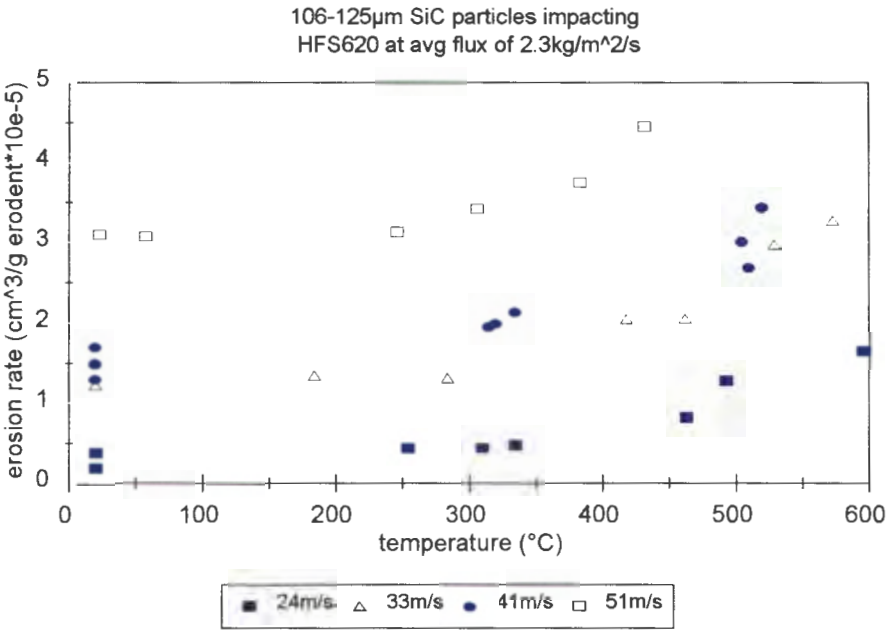

Figure 6.20 : Graph showing the results of 106-125µm SiC particles bombarding an HF620 steel at a fixed flux of 2.3kg.m^{-2}.s^{-1} over a range of velocities.

Tests using SiC were performed at a higher flux than the SiO_2 particles due to the inaccuracy caused by the use of the double cone feeder device which was in operation at the time. The particle flow behaviour could not be reproduced exactly and hence a difference in fluxes resulted. Similar behaviour with respect to velocity and temperature was observed but the magnitude of the erosion rate results were lower than those obtained using the SiO_2. This is due to the difference in fluxes used. Velocity tests with the SiC were performed with a flux of 2.3kg.m^{-2}.s^{-1}, whilst tests with the SiO_2 were performed with a flux of 2.0kgm^{-2}.s^{-1}. Figure 6.16 shows the marked drop in erosion rate by increasing the flux from 2.1 to 3.5kg.m^{-2}.s^{-1}.

6.5 Changes in the subsurface of the material during erosion

6.5.1 The change in the microhardness of the material as a function of depth below the surface

Cross-sectional mocrohardness profiles were taken of specimens eroded by 106-125µm plant fly ash particles at a particle velocity of 24m.s^{-1} and a particle flux of 0.17kg.m^{-2}.s^{-1} for four different specimen temperatures. A summary of the testing is seen in Figure 6.21 for two extremes of temperature tested. Here average Knoop hardness is mapped against the depth below the damaged surface. One data point is the average of 3 indents. Thus, one curve is the result of 60 indents.

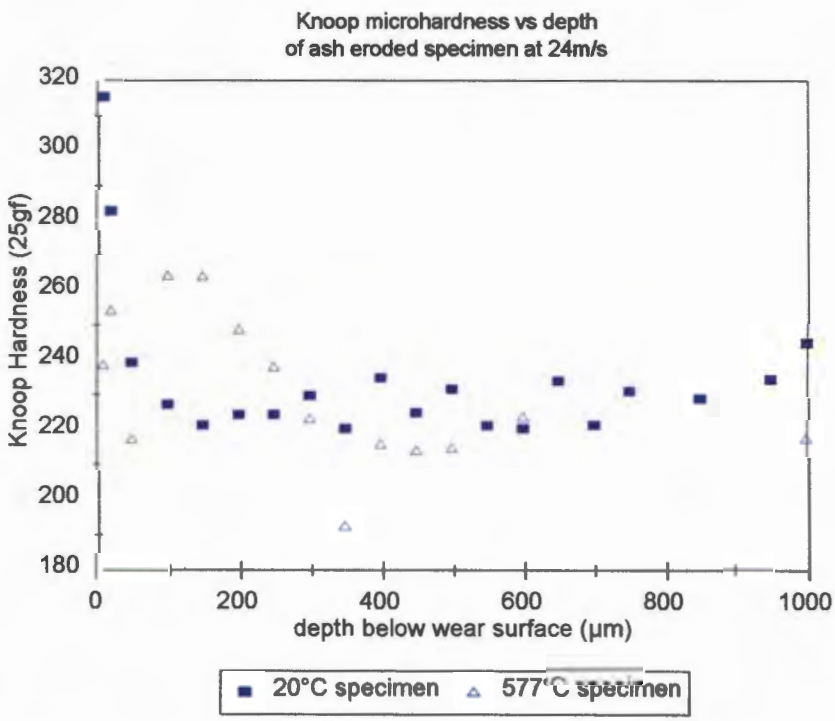

Figure 6.21 : Graph of microhardness vs depth below target surface for specimens eroded with fly ash (Hendrina power station), showing the increase in the depth of plasticity for the specimen eroded at higher temperature.

The specimen eroded at 20°C can be seen to have hardened appreciably at the surface. The hardness at 10μm below the surface is 315, compared with an average bulk hardness of 230. The depth to which the plastic deformation in this specimen extends is approximately 150μm. The specimen eroded at 577°C reaches a maximum hardness of 265 Knoop, but this is 130μm below the surface. The hardness of the specimen eroded at 577°C, 10μm below the surface is 240. However, the depth below the surface to which the plastic zone extends is 425μm for the 577°C specimen and 150μm for the 20°C specimen.

6.5.2 The dislocation density of the eroded specimens as a function of increasing temperature

Transmission electron microscopy was used in an attempt to view the subsurface damage of eroded specimens. An as-received specimen was first examined to quantify the presence of dislocations prior to damage by impacting particles. HFS620 specimens that had been eroded at a particle velocity of 24m.s^{-1} by 106-125μm ash particles were used to observe any changes in dislocation density and distribution due to an increase in strain and or temperature in the subsurface of the material. The different temperatures examined were 20 and 577°C.

Figure 6.22 shows the dislocation structure in a specimen prepared from the as received material. Dislocations are seen to be arranged in lines with a minimum of intersections and entanglement.

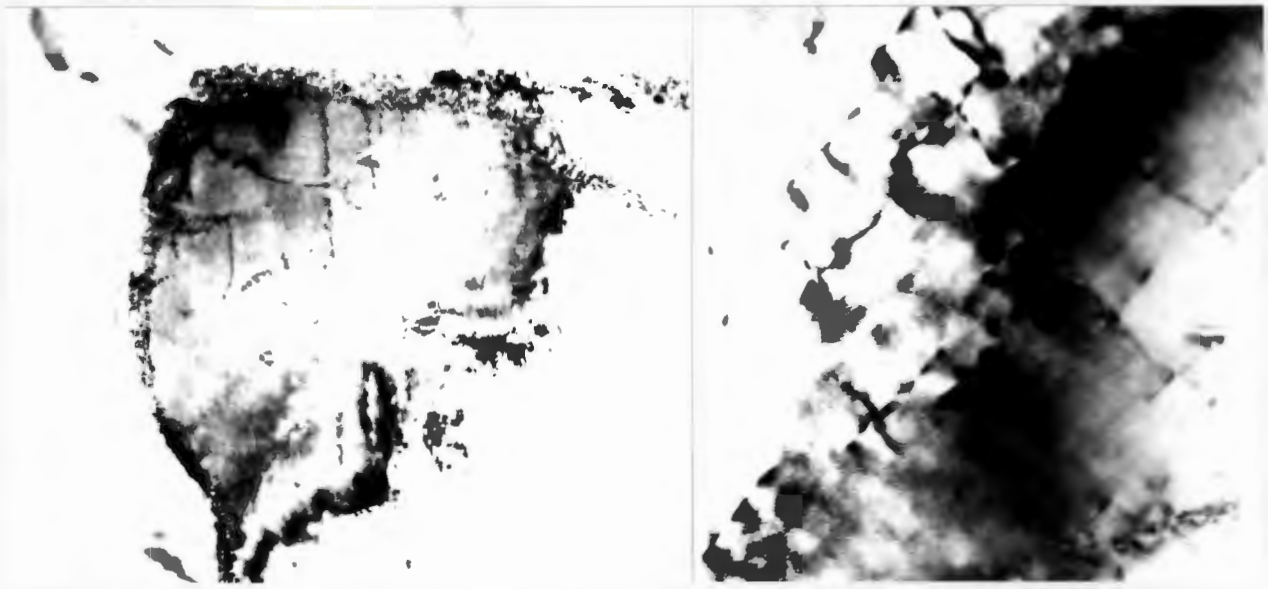

Figure 6.22 : Transmission electron micrograph of the dislocation density in an HFS620 specimen prior to erosion.

It was expected that entangled dislocations would be evident due to a buildup of strain in the material subsurface, concurring with the microhardness tests where the eroded specimens showed strong evidence of workhardening in this region. However no distinctive differences in dislocation density between the as received specimen, the specimen eroded at 20°C and the specimen eroded at 577°C were found. It is thought that more detailed studies would reveal more positive results. A greater buildup of strain could be achieved using SiC or SiO_2 particles at the highest velocity ($51m.s^{-1}$) which would yield a density of dislocaiton sites more easily differentiable from the material in its as received state.

6.6 The change in mechanical properties of the material as a function of material temperature.

Results of the tensile testing are shown in Figure 6.23. It can be seen that the yield strength of the HFS620 1Cr½Mo steel drops as a function of increasing temperature. The percentage reduction in area increases with temperature, which implies an increase in material ductility. This is marked at temperatures above 400°C.

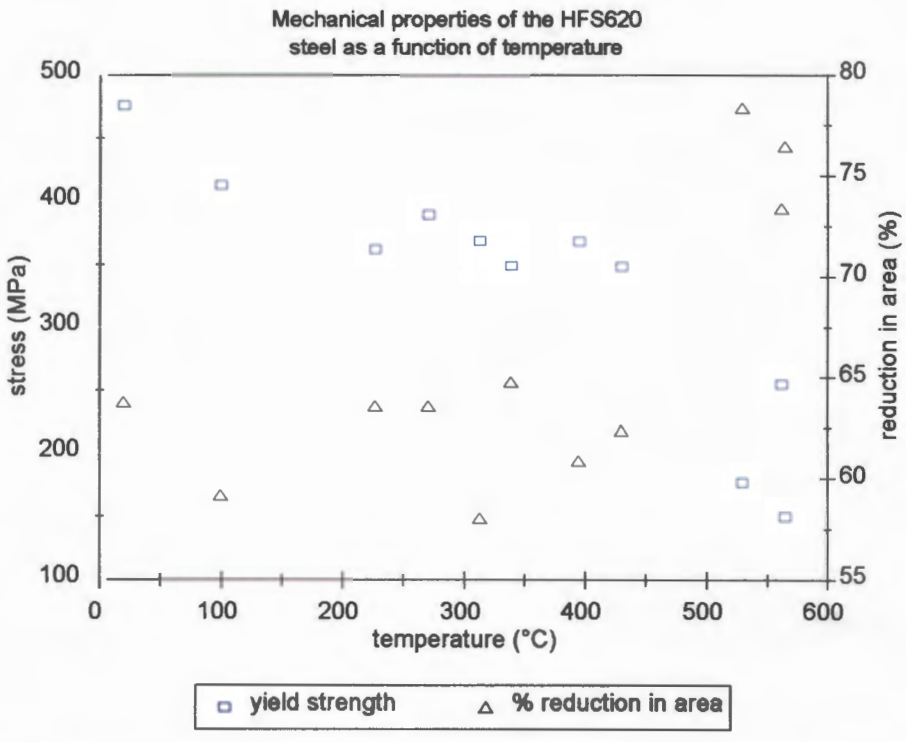

Figure 6.23 : Graph illustrating the changes in yield strength and percentage reduction in area with increasing temperature.

The results of this analysis are summarised in Table 6.4.

Temperature °C	Yield strength MPa	Reduction in area %
20	477	63.8
100	414	59.2
227	363	63.6
271	390	63.6
315	369	58.1
338	350	64.8
351	408	59.3
395	369	60.9
430	349	62.4
530	178	78.4
565	151	76.5

Table 6.4 : A list of the summarised data from material strength testing.

6.7 Results of the erosion testing of thermal sprayed coatings

This section describes results of high temperature erosion testing of two electric arc thermal sprayed coatings. These coatings are commonly used in the South African coal fired power generation industry as a means of increasing the time between boiler tube replacement. Their role is thus sacrificial. It is thus important to rank their erosion performance relative to an uncoated specimen to gauge their lifespan.

In addition to quantitative erosion tests, scanning electron micrographs assist in defining an erosion wear mechanism for these coatings. Table 6.5 summarises the erosion tests that were performed. In all cases the erodent used was 106-125µm silicon carbide. The nominal chemical composition of the coatings in percentage by mass is also shown. The substrate material for both coatings was the HFS620 1Cr ½Mo steel.

	Coating 1 Composition 43Cr 53Ni 4Al Substrate : HF 620	Coating 2 Composition 26.5Cr 67.75Fe 5.75Al Substrate : HF 620
thicknesses tested (μm)	100 200	100
velocities tested ($m.s^{-1}$)	24 42 52	24 42 52
range of temp (°C)	20 - 500	20 - 500
mass flux ($kg.m^{-2}.s^{-1}$)	2.1	2.1
as received surface roughness R_a (μm)	33.1 ± 0.3	26.2 ± 4.0

Table 6.5 : A list of the complete set of conditions used to test two arc sprayed coatings.

6.7.1 Measuring steady state mass loss

Following experience with testing the as received HFS620 steel it was decided to erode an as received coating with small increments (15g) of SiC particles (106-125μm) to determine when a steady state mass loss had been reached. Results of this testing, illustrated in Figure 6.24, show a large initial mass loss. The initial mass loss after 15g of 106-125μm SiC particles is 3 times the steady state mass loss per 15g of erodent. This result was obtained for a 100μm thick coating 1 bombarded at $41m.s^{-1}$. Roughness measurement results from similar tests also using 15g batches of erodent are also graphed and it can be seen how a smoothing of the surface accompanies steady state mass loss. These results are included on the secondary y-axis in Figure 6.24.

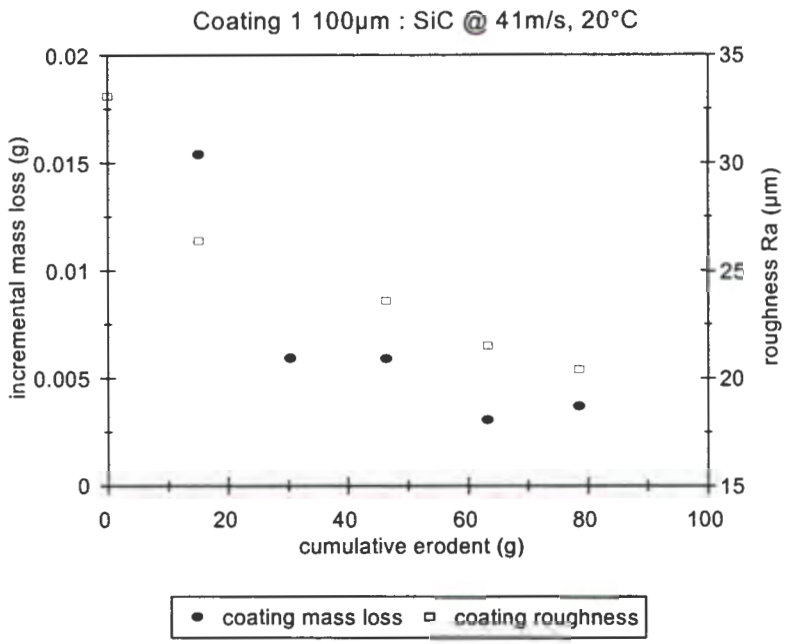

Figure 6.24 : Graph showing the incremental mass loss and decrease in surface roughness as a function of cumulative erodent when eroding an as received coating 1 (roughness measurements courtesy of P. Hoop).

The morphology of an as-received coating surface explains this high initial loss. This is seen in Figure 6.25(a) which is a low magnification scanning electron micrograph of coating 1. The surface is non-uniform with numerous crests and half exposed pores. These irregularities are more easily removed by impacting particles compared to a flat surface. Once the surface takes on a more regular surface profile steady state mass loss occurs. The appearance of an eroded surface after steady state mass loss has been reached is seen in Figure 6.25(b).

The extent of the smoothing is expressed in Table 6.6 which compares the roughnesses of the coatings before and after steady state mass loss occurred. These results are from tests conducted at $24m.s^{-1}$ with 106-125µm SiC particles at a velocity of $24m.s^{-1}$ and a flux of $2.85kg.m^{-2}.s^{-1}$. Coating 1 showed a 9% decrease in surface roughness (i.e. it became smoother) whilst coating 2 showed a more convincing 19% decrease in surface roughness. It can also be seen that there is no definite trend linking roughness to the specimen temperature during erosion tests.

Specimen temperature (°C)	Coating 1 : Roughness Ra (μm) as received = 33.1±0.3	Coating 2 Roughness Ra (μm) as received = 26.2±4.0
20	20.4±1.0	
434	32.6±1.2	
514	30.7±1.9	
20		18.7±1.3
415		24.3±0.9
550		20.5±1.9

Table 6.6 : Roughness of the coated specimens as a function of temperature.

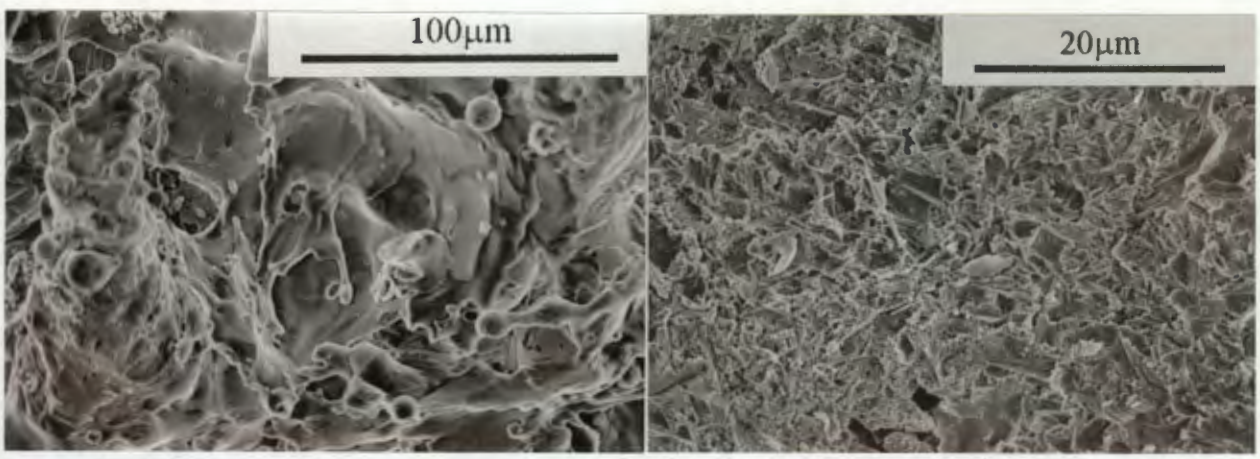

(a) *(b)*

Figure 6.25 : (a) Scanning electron micrograph of the as received surface of coating 1. Surface irregularities in the form of particle globules and splats can be seen. (b) Coating 1 after reaching steady state mass loss.

6.7.2 *The effect of temperature on erosion wear rates of thermal sprayed coatings*

Figure 6.26 illustrates the effect of temperature on the wear rates of the thermal sprayed coatings. These results are from tests conducted with 106-125μm SiC particles at a flux of 2.85kg.m^{-2}.s^{-1} and velocities of 24 and 41 m.s^{-1}. In addition, Figure 6.26 shows the results of testing carried out on the substrate material under similar conditions. Erosion rates increase with temperature for coatings 1 and 2 at 41 m.s^{-1}. These rates are greater in magnitude than that recorded for the bare substrate.

However, although both coatings have erosion rates higher than those determined for the bare substrate at room temperature, any trend of an increase in rates with increasing temperature was unclear, probably due to the inconsistency in the quality of the coating.

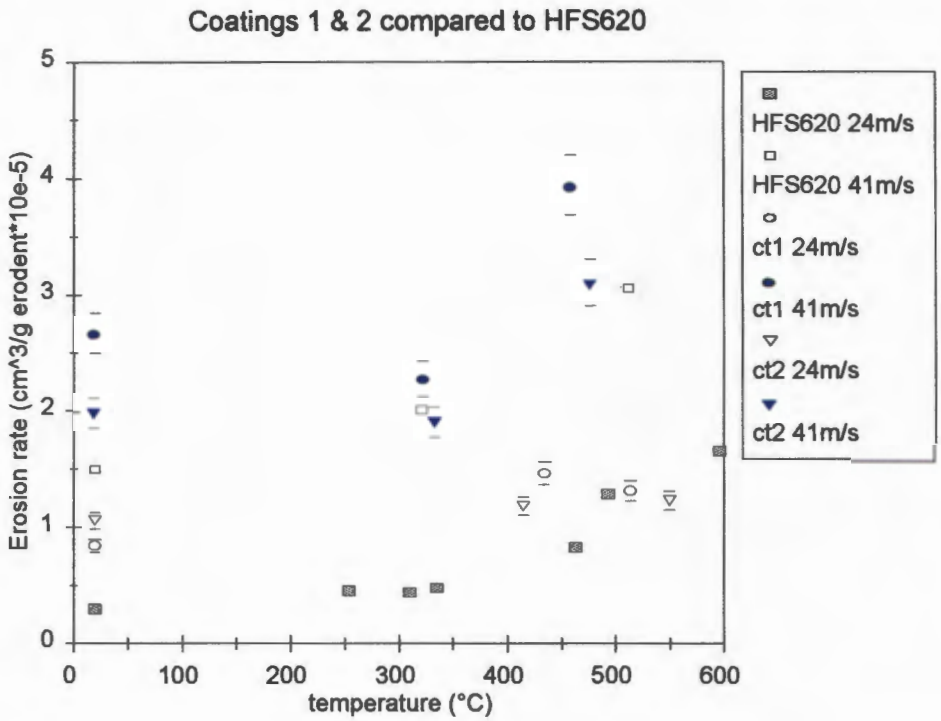

Figure 6.26 : Graph of erosion rate vs temperature for coatings 1 and 2 and a bare substrate at two different velocities, showing the increase in wear rates with temperature.

6.7.3 The effect of velocity on wear rates

The effect of velocity on wear rates was tested at 20°C only. An equivalent sensitivity to velocity can be seen for both the coatings since all of the data falls in one band. This can be seen in Figure 6.27 However, it is interesting to note that the velocity exponent for these two coatings at 20°C is 1.64 as opposed to 2.12 for the bare substrate at the same temperature (derivation of this exponent is shown in section 7.4). The physical significance of this is that the coatings are less sensitive to changes in particle velocity than the bare substrate.

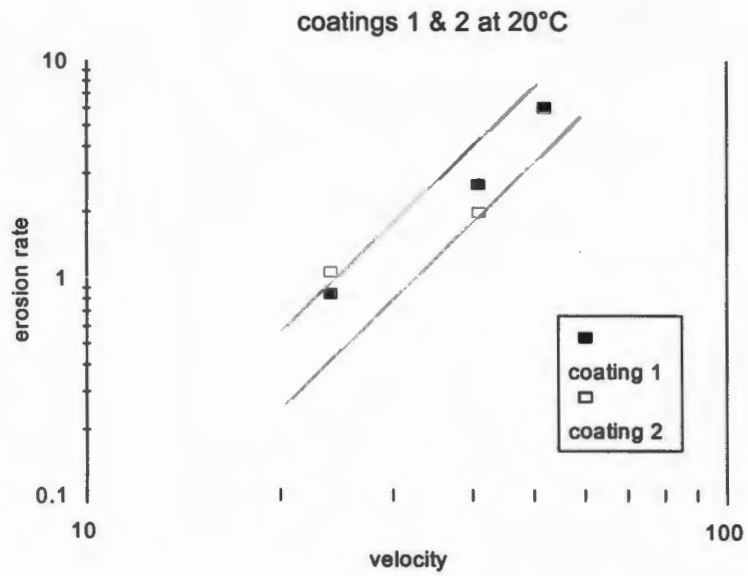

Figure 6.27 : Erosion rate vs velocity for coatings 1 and 2, showing a linear relationship between the natural logarithm of rate and velocity indicating an exponential relationship between erosion rate and particle velocity for this particluar temperature.

In an attempt to quantify the differences in mechanical properties between the deposited coatings and the bulk material, cross sectional microhardness tests were performed. The interface between the coating and substrate is clearly delineated in Figure 6.28 where there is a marked drop in microhardness between 200 and 350μm below the surface for coatings 2 and 1 respectively. Figure 6.29 also shows the deformed layer which exists beneath the coating due to shot blasting the specimen prior to coating application.

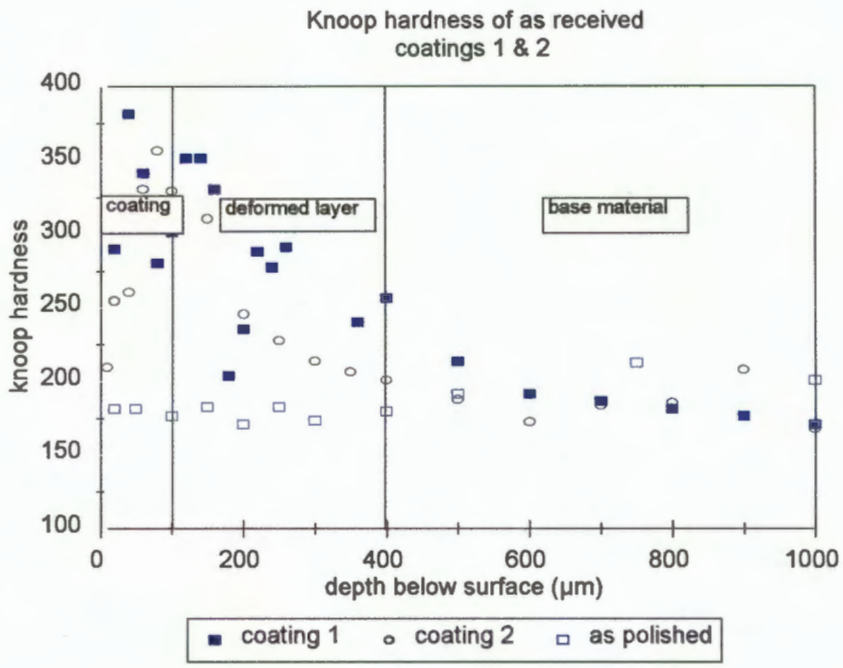

Figure 6.28 : A comparison of the microhardness of the as received coatings 1 & 2 and an as polished specimen of the bulk HFS620 material.

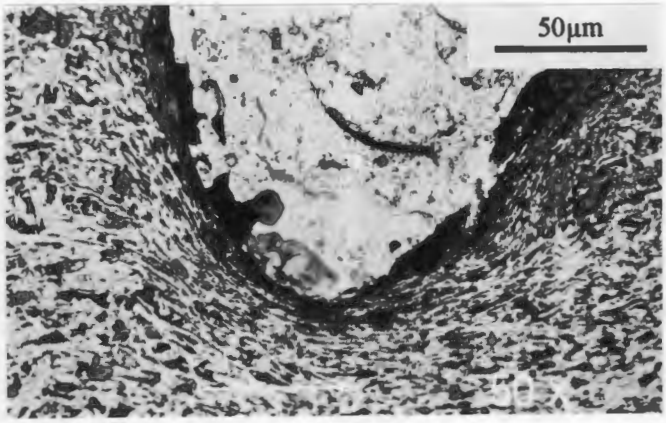

Figure 6.29 : Optical micrograph of a cross section of coating 1 showing the reduced grain size at the coating - substrate interface due to deformation from pre-coating application shot blasting.

6.7.4 The coating wear mechanism

The mechanism of coating removal is not disimilar to that observed on the bare substrate. This can be seen when comparing impact sites on the surface of an eroded coating with an impact site from a bare eroded HFS620, obtained under similar conditions of particle velocity, size and type. This is seen in Figure 6.30(a) and (b). Figure 6.30(a) shows an impact site on coating 1 caused by a SiC particle (106-125µm) at a velocity of 41 $m.s^{-1}$ and a specimen temperature of approximately 500°C. Figure 6.30(b) shows a site on a bare HFS620 caused by a similar SiC particle at 33 $m.s^{-1}$. Although the particle velocities are different, the same plastic deformation leading to the extrusion of lips and ridges can be seen. Subsequent particle strikes further work-harden these features until they fracture and are removed from the specimen surface.

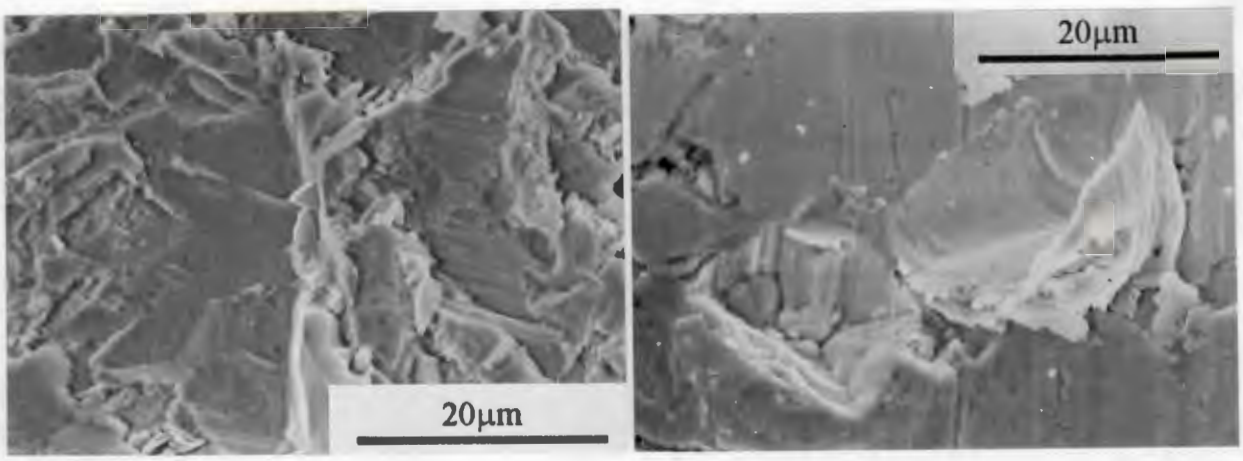

(a) (b)

Figure 6.30 : (a) An impact site on the surface of coating 1 eroded by SiC particles at 41 m.s^{-1}. (b) An impact site on the surface of an HFS620 specimen. This specimen has been eroded at 33 m.s^{-1}.

However, the removal of material is influenced by :

a) The presence of porosity in the coatings.

b) The rough surface morphology of the coating.

Both micro and macro porosity result due to the entrapment of gases on fast cooling of the molten liquid and the inhomogenous deposition of subsequent molten splats. A deposited splat is seen in Figure 6.31(a). Porosity also results when powders are not fully molten prior to impacting the substrate. Evidence of unmolten powder is seen in Figure 6.31(b) which is only weakly adhered to the surface. Porosity in the coating creates a stress raiser for the material lying above it. A particle strike above the location of a pore localises the stresses at the edge of the pore. There is thus a more rapid buildup of strain than were this material supported from below. This rapid strain buildup results in premature material loss and hence a higher erosion rate. This is seen in Figure 6.32 where a large pore has been exposed by continual particle bombardment.

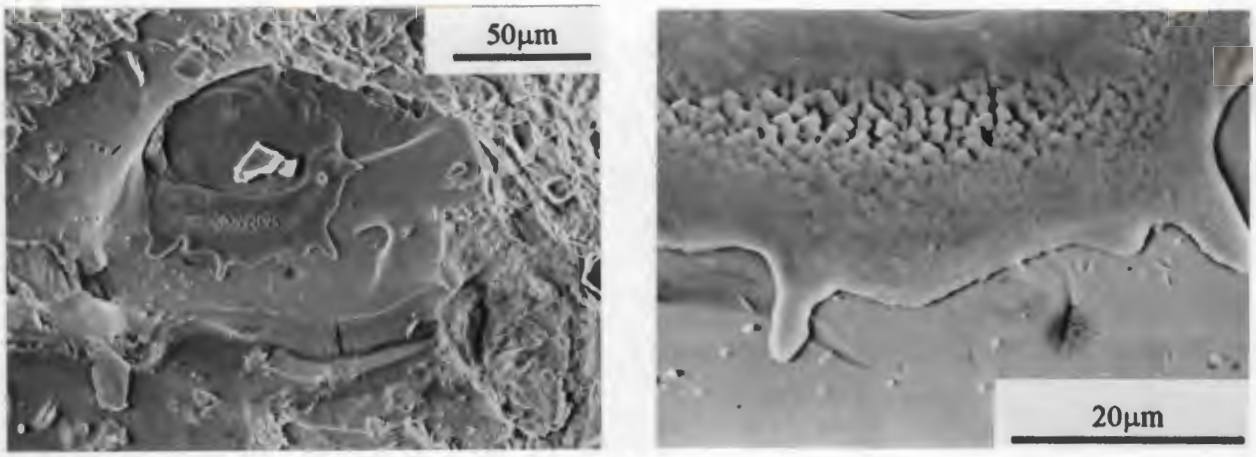

(a) (b)

Figure 6.31 : (a) The as received surface of coating 1. (b) A higher magnification of the area seen in (a). Here it is seen how the metal powder used for the coatings has not melted in the electric arc. A particle impact would easily remove such a feature.

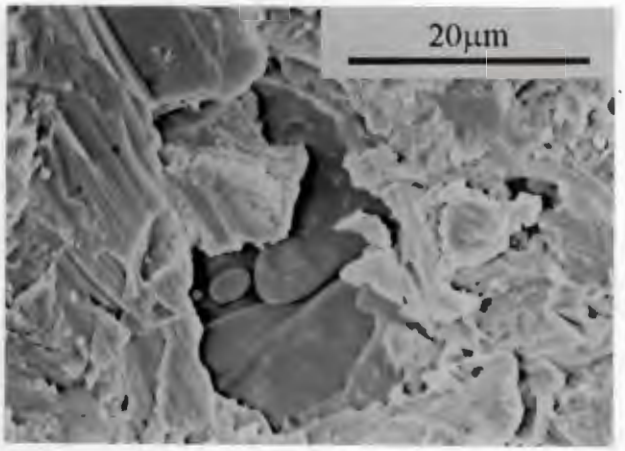

Figure 6.32 : Micrograph of a general erosion site on coating 1. A large pore can be seen in the center of the picture.

7. Discussion

The work performed falls clearly into two parts. Initially, the variables associated with high temperature erosive wear conditions in pulverised fuel boiler combustors were identified and quantified and an apparatus constructed to simulate those conditions. The design and performance of this apparatus has been discussed separately. The present discussion deals with the influence of process variables on the erosive wear of a boiler tube steel and attempts to relate trends that were found to the properties of erodents and the steel target.

7.1 The effect of erodent shape, type and size

7.1.1 The effect of erodent shape and type

The effect of particle type and shape on erosion rates has been reported to be significant [11,33]. Palasamudram and Bahadur [33] found that SiC particles caused up to 4.5 times more wear than similar sized SiO_2 particles. However, Levy and Chik [11] found that for particles, with an average hardness in excess of 700kg.mm^{-2}, impacting a ductile material, shape does not play a significant role in determining erosive wear rates. This conclusion was reached when it was shown that SiO_2, Al_2O_3 and SiC particles at a velocity of 80m.s^{-1} caused erosion of the same magnitude at specimen orientations of 30 and 90°. These erodents had measured hardnesses of 700, 1900 and 3000kgf.mm^{-2} respectively.

The present results are partly in agreement with Levy and Chik [11] and show that SiC and SiO_2 particles cause similar erosion rates across the range of test temperatures despite the SiC particles having a sharp, angular morphology in comparison to the more rounded SiO_2.

It is interesting to note, however, that when using steel shot as an erodent, Liebhard and Levy [10] found that angular steel particles (HV = 150kgf.mm^{-2}) caused up to 4 times more damage than spherical steel particles when impacting an AISI 1020 steel of HV 150kgf.mm^{-2}. It appears that as the erodent hardness approaches that of the target, the erosion rate becomes dependent on the particle shape, but when the particles exceed an average hardness of HV = 700kgf.mm^{-2}, shape effects are minimised [10,11].

It should be noted that Palasamudram and Bahadur performed their erosion tests in a fluidised bed environment, where the particle mass flux and velocities were considerably different to those of Levy and Chik. A difference in material removal mechanisms between these two different erosion systems may account for this conflict in opinion. MacAdam and Stringer [30] observed a low stress three body abrasion mechanism in their fluidised bed tests, where the eroding particles were often constrained to the surface of the target.

However, in a pure erosion situation such as gas blast apparatus, where the particles are not constrained to the target surface, Levy [47] found that material removal depends primarily on the forging and work hardening of lips and ridges that have been formed by the eroding particles. This is a subtly different situation, for although high strain rates are involved in both cases, three - body abrasion of a material results in more material removal through cutting compared to material removal being chiefly a secondary result of particle impact. Scanning electron microscopy of damaged surfaces bombarded by ash, SiC and SiO_2 particles in this work revealed the presence of extruded lips and ridges similar to those observed by Levy.

An erodent hardness threshold of HV > 700 cannot, however, be seen as an absolute value. This was evidenced in the results of comparative erosion tests between the 106-125μm SiO_2 (HV 1373), SiC (HV 2481) and a plant fly ash (HV 976). Despite the average hardness of the ash being in excess of HV 700, it caused only 75% of the wear caused by SiC and SiO_2 at room temperature and 36% thereof at 550°C. The difference in erosion rates between the three erodents can clearly not be solely

accounted for by particle hardness or shape or type, but rather a combination of these considerations.

The spherical ash particles can be classified into different groups. The majority of these particles are either hollow (cenospherical), or hollow containing small particles inside (plerospherical). It is thought that only the smallest of the particles (< 20μm) are in fact solid, those in the size range 20-100μm being either cenospherical or plerospherical. Although the fly ash shape is generally spherical in the smaller size ranges (<100μm) it becomes amorphous as the size increases. Particles larger than 100μm are either agglomerations of spheres or char particles which have not fully combusted. There is thus a mixture of shapes and constitution in any one ash sample.

The nature of the coal ash also makes it a friable particle. The energy that the particles have upon impact is not effectively transferred to the target surface and they fracture easily compared to the SiC and SiO_2 particles which only lose edges in the form of small chips of material. The larger ash particles which are generally agglomerations of spheres, separate as well as fragment. Evidence of spherical particles shattering was clearly shown in electron micrographs of particles which had impacted the surface. Thus much of the particles' kinetic energy is not transferred to the target and lower erosive wear rates result.

7.1.2 The effect of ash mineralogy on erosion

During the erosion process, only a small area of the particle surface comes into contact with the target material causing damage. The size of the resultant crater and associated deformed area is small compared to the size of the particle. This ratio varies with the type, size and velocity of the erodent particles. SiO_2 and SiC particles, for instance, cause much greater damage to the steel surface than the ash. Part of the reason for this is due to the nature of the ash which is generally friable and fragments upon impact as discussed previously.

It is believed that the 'abrasive' portion of the ash is quartz which has a high hardness [18] but is only present in small volumes within the erodent particle as evidenced by quantitative xray diffraction (XRD). Thus, individual damage sites are smaller than those obtained with harder and stronger erodent particles and the wear rates are proportionately lower. Further, it might be expected that as the quartz content increases, the erosivity of the ash will also increase. However, such a relationship has not been shown in this work where the erosivity of eight different plant fly ashes could not be positively linked to their quartz content within the error of the xray diffraction (XRD) measurements. No correlation was found however between the chemistry of the ash and the quartz and mullite content.

A relationship between the chemistry and the mineralogy of the ash was first proposed by Raask [18], who suggested that in the absence of mineralogical data, the percentage quartz content **q** of the ash can be estimated from the relationship :

$$\mathbf{q = SiO_2 - 1.5*Al_2O_3}$$

However, this relationship was proposed for northern hemispherical ashes, which have a different mineralogy compared to Southern African ashes. The constant of 1.5 in this equation was thus changed to 1.3 by averaging the quartz content in the eight ashes tested and equating it to the right hand side of the equation where the SiO_2 and Al_2O_3 contents of the ashes had also been averaged.

Figure 7.1 plots the percentage occurrence of the chemical constituents and the proposed chemistry-mineralogy relationship as a function of increasing quartz content in the different ashes. The equation $\mathbf{q = SiO_2 - 1.3*Al_2O_3}$ would be validated if $\mathbf{SiO_2 - 1.3*Al_2O_3}$ increased with increasing quartz as measured by XRD. However, the chemistry of the ash is shown to be independent of the percentage quartz measured by XRD, as this data falls on a horizontal line.

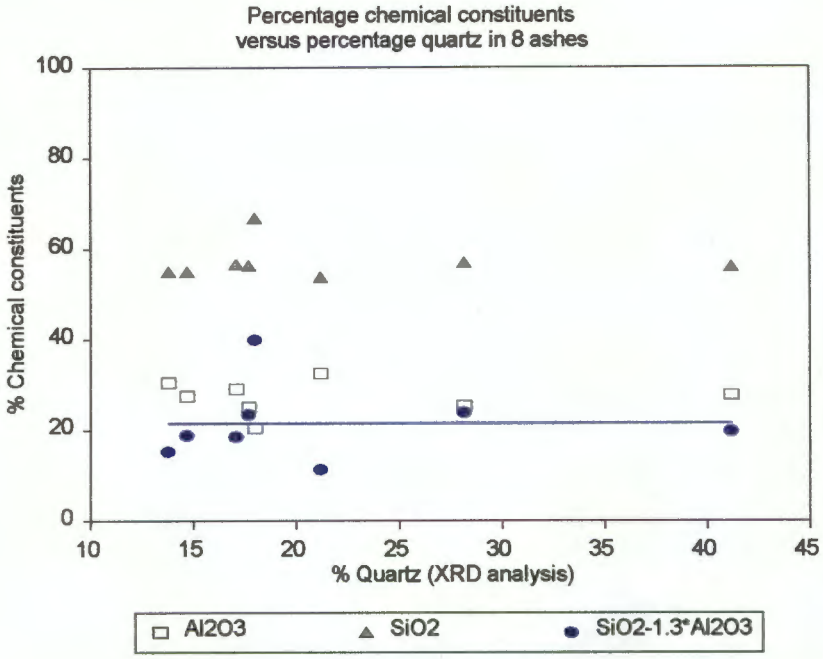

Figure 7.1 : Graph of the main chemical constituents of coal ash as a function of increasing quartz content. In addition the proposed relationship between chemistry and mineralogy is plotted.

The results of this analysis confirms work by Bosch [35] who showed that a relationship between chemistry and quartz for fly ash is not a general one but is dependant on the boiler from which it is sourced. He found a linear relationship between silica and quartz for different sized particles (sourced from different precipitator fields) for three different South African power stations. However, these relationships differed between the different power stations. This suggests that ash erosivity should be estimated solely by determining the mineralogy directly rather than from a chemical analysis which is in agreement with this work.

The mineralogy of the ash also has implications for changing erosivity with increasing temperature. The bulk of the ash consists of quartz and mullite. However, between 14 and 46% of an ash sample can be a glassy phase. Although the softening temperature of silica glass is quoted as 915°C, this is the temperature at which it deforms under its own weight. Silica based glassy phases in ash soften over a wide range of temperature, which has an influence on the plasticity and thus lowers the erosivity of fly ash as the temperature increases.

7.1.3 The effect of erodent size

Particle size is believed to have a significant effect on erosion wear rates [18,30,34]. It is generally accepted that erosion rates increase with increasing particle size until a plateau is reached whereafter any further increases in particle size has no effect. An explanation for this effect is discussed by Shewmon [103] for spherical particles impacting ductile materials at velocities between 70 and 130m.s^{-1}.

Shewmon argues that the sudden plastic deformation caused by an impacting particle results in a localised temperature increase, limiting the ability of the target to absorb work, but causing extreme localised plasticity. The depth of the deformed layer increases in proportion with the particle radius. For particle sizes less than a transition particle radius, any temperature rise will be lower leading to an increased material flow stress and a decreased erosion rate.

However, in the present work, the results of testing with the 63-106µm SiO_2 and SiC particle size range show erosion rates which are up to 100% greater than obtained for the 106-125µm size for similar conditions of particle velocity (24m.s^{-1}) and flux (2.43kg.m^{-2}.s^{-1}) at room temperature and 42% greater at 550°C. A similar effect has been reported by Liebhard and Levy [10].

Results of ash testing, however, show little difference in the erosion rates between the two size ranges where the 63-106µm particles caused 4% less wear on average at room temperature than the 106-125µm particles. It is believed that the differences in the morphology of the ash in these size rnages strongly influences the erosivity of the ash and assists in explaining this apparent anomoly compared to the results from testing the SiC and SiO_2 particles.

Metallographic evidence suggests that the agglomerations of smaller particles which make up the larger particles dissociate upon impact. This effectively means that smaller particles are striking the surface than the 106-125µm sieve aperture size range

and will cause similar damage to the nominally smaller particles in the 63-106μm size range.

In the case of the SiC and SiO_2 particles this result would suggest that despite the target being subjected to similar masses of different sized erodents with equivalent amounts of kinetic energy prior to impacting the specimen, the smaller particles are more effective in removing material from the surface.

These differences in erosion rates with changing particle size are difficult to explain quantitatively since it is generally believed that a number of factors combine to influence mass loss. An explanation for these results takes into account the specimen orientation and possible particle deflection as well as errors in the particle velocity calibration.

Ductile materials, such as the steel used in this work, show maximum wear rates when orientated at acute angles relative to the oncoming stream of particles. Sundararajan [43] has theoretically calculated this angle to be 18-22° for angular particles and in addition shown that for spherical particles the angle is 40-45°. Tests conducted using angular SiC particles showed the specimen orientation at which maximum wear takes place to be approximately 20°, which is in agreement with Sundararajan's theoretical prediction. Further tests with fly ash as the erodent, which is largely made up of spherical particles and agglomerations of spherical particles, confirmed this theoretical result of maximum wear at 40°. In this work the orientation of the specimen to the gas stream was fixed at 40° to achieve high erosive wear when using fly ash particles.

Small particles are more likely to follow the flow field of the carrier gas than larger particles and be deflected away from the target surface as the specimen orientation is lowered to angles less than 30° [31]. Tests by Tabakoff et al [31] showed that coal ash particles became noticeably influenced by a flow field when less than 30μm in size leading to lower erosion rates. This implies that the smaller particles do not possess sufficient momentum, due to their low mass, to follow the original direction of the gas movement when nearing the target, which reduces their average impact angle leading to a change in erosion rates.

The difference in wear rate for a specimen orientated at an angle of 40° compared to 20° was found to be 18% less when using 106-125μm SiC particles. If the smaller 63-106μm particles were deflected from the surface to strike the target at lower angles of incidence then it follows that, in this study, the 63-106μm SiC and SiO_2 particles will cause more wear than the 106-125μm size range.

However, calculations suggest that smaller 63-106μm particles do possess sufficient momentum to be unaffected by the gas flow field using the particle inertia approach by Dosanjh et al [32] where a momentum equilibrium constant λ is quantified.

$$\lambda = \rho_p * d_p^2 * 2 * u / (18 * \mu * d)$$

where :

ρ_p	=	particle density
d_p	=	particle diameter
μ	=	gas jet dynamic viscosity
d	=	nozzle diameter
u	=	gas jet velocity

e.g. Considering an SiO_2 particle from the 63-106μm size range,

ρ_p	=	$2880 kg.m^{-3}$
d_p	=	85μm (an average of the 63-106μm size range)
μ	=	3.765×10^{-5} $kg.m^{-1}.s^{-1}$ (air at 577°C)
d	=	9.6mm
u	=	$64 m.s^{-1}$

$$\lambda = 409$$

Values for the momentum equilibrium constant are listed in Table 7.1.

Particle size range	Momentum equilibrium constant at 20°C	Momentum equilibrium constant at 577°C
63-106μm	835	409
106-125μm	1555	762

Table 7.1: The momentum equilibrium constants for various temperatures.

Dosanjh et al state that for $\lambda > 10$, the particles will not be affected by the gas flow field, and in the case where there is an obstacle (i.e. an erosion specimen) in the gas / particle path, the particles will strike the obstacle. The value for λ for the two temperatures and size ranges tested is an order of magnitude greater than Dosanjh et al's critical value of 10. This particular approach therefore shows that neither the 63-106μm size SiO_2 particles, nor the 106-125μm size are likely to be affected by the flow of gas around the specimen.

For $\lambda = 9$ i.e. less than the limiting value of 10, in conditions of equivalent gas jet velocity and dynamic viscosity for the 577°C case, the calculation shows that a particle size of 13μm would be affected by the gas flow which supports Tabakoff's work [31]. However, the limitation of the momentum equilibrium constant λ to this work is that it was derived for the simple system of a flat plate normal to the impinging gas stream.

Tabakoff et al [31] showed that particles can be deflected by the specimen at angles of inclination to the gas stream less than 30°. Using an example of a 10μm fly ash particle from their work, at a velocity of 128m.s^{-1}, a nozzle diameter of 76.2mm, ambient temperature of 20°C and a 30° angled specimen, the momentum equilibrium constant was found to be $\lambda = 2$. Tabakoff et al are thus in good agreement with Dosanjh et al [32] which illustrates that in spite of the momentum equilibrium constant being derived for a plate normal to the gas stream, it is also applicable to the angled plate case too. It is not known, however, to what extent the value of the constant would change if all other variables were held constant except for the angle of inclination.

Nevertheless since test results are system dependent, it is believed that despite calculations showing otherwise, that particle deflection for the smaller particles does occur.

An analysis of the number of strikes in the centre of a target bombarded by a fixed mass (5g) of 106-125μm SiC compared with 5g of 63-106μm particles showed that despite there being 2.5 times more particles in the smaller size range, there were only 2.1 times more strikes counted. This implies that many of the 63-106μm particles are deflected away from the central part of the target. In addition, the average length of the cuts seen on the specimen bombarded by the smaller particles was half that of the larger particles; despite the volume of the larger particles being 2.5 times greater. This demonstrates that relative to their size, the smaller particles inflict longer cuts than the larger particles for the specimen orientation of 40°, and as a consequence cause more severe wear. However, it is clear that more work needs to be carried out on the effect of particle size on wear rates in order to clarify the situation further.

The substantial difference in erosion rates found between the large and the small erodents and between fly ash and SiC and SiO_2 may also in part be due to differences in particle velocity. As erosion rates are strongly dependant on particle velocity, a small increase in velocity results in a large increase in the erosion rate.

The calibration method used in this study did not detect any consistent difference in velocity between the particle types, nor the two size ranges tested under similar test conditions. However, a theoretical analysis of the particle flow in an air stream using an approach outlined by Raask [18] showed that there would be considerable differences in the velocity of the different erodents. This is due to variations in particle morphology and density when testing at similar gas pressures. The analysis showed that the final velocity of the coal ash particles would be 9% greater than the SiC and 22% greater than the SiO_2.

Based on this approach, each particle is given a shape factor which is determined by matching a Krumbein roundness scale chart of basic particle shapes with scanning electron micrographs of the particles themselves. These shape factors are then

normalised with respect to the drag coefficient of a sphere to estimate the drag coefficients (C_d) of the fly ash, SiO_2 and SiC particles.

Drag coefficients C_d :

Sphere	= 0.115	(for turbulent flow)
Fly ash	= 0.155 - 0.169	
SiO_2	= 0.176 - 0.181	
SiC	= 0.238 - 0.246.	

Drag on a particle, F_d $= 0.5*\rho_g*(v - v_g)^2*C_d*A_p$

Alternatively m*dv/dt $= 0.5*\rho_g*(v - v_g)^2*C_d*A_p$

According to Raask this equation can be rearranged and gives :

$$(\rho*d^2)/(18*\eta*C_d*Re) = (v - v_g)/(dv/dt)$$

where

ρ	=	particle density
d	=	equivalent particle diameter (sieved grit size average)
η	=	carrier gas viscosity
C_d	=	particle drag coefficient (normalised shape factor)
Re	=	Reynolds' number
v	=	particle velocity
v_g	=	gas velocity
dv/dt	=	particle acceleration
m	=	mass of one particle

The aim was to group all of the constants, and isolate the particle final velocity from which its acceleration through the tube could be determined. The constants for each particle in the 106-125μm size range were determined as follows :

coal ash	=	266×10^{-6}
silica sand	=	324×10^{-6}
silicon carbide	=	290×10^{-6}.

The spread of these derived constants is approximately 18% which is appreciable. This is seen in Figure 7.2 which graphs time of flight of a particle in the acceleration tube against its final velocity. The spread of velocities is seen when examining a fixed time of flight. At room temperature with a velocity exponent of 2.12 and an average particle velocity of $24 m.s^{-1}$ this 18% spread in the particles' velocities translates to a possible 46% greater erosion rate for ash compared to the SiO_2 erodent assuming similar erosivities.

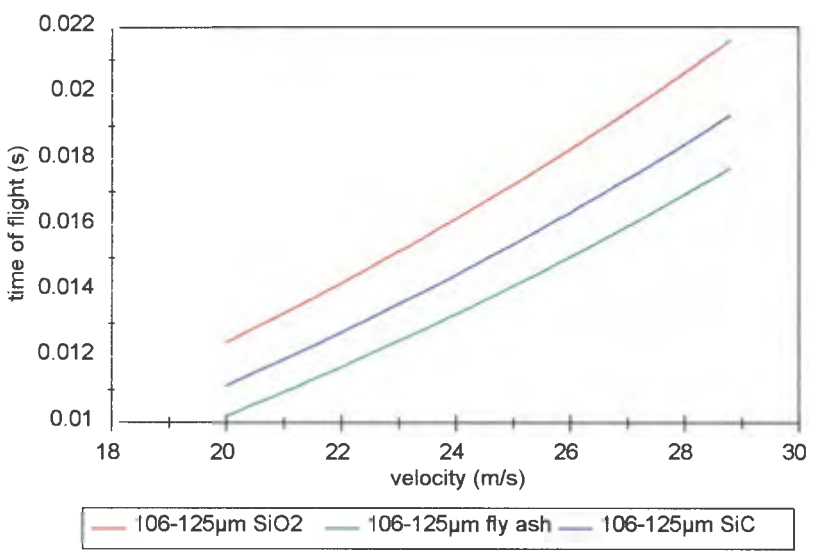

Figure 7.2 : Graph of the time of flight of each particle versus their final velocity, showing how the theory indicates a wide scatter of flight times that each erodent would need to achieve the same velocity.

However, the erosivity of ash is considerably less than the SiO_2 or the SiC and any differences in the erosion rate will be lower than the calculated figure of 46%. The actual results show that the ash has an erosivity which is only 75% of either the SiC or SiO_2 at room temperature.

In addition, the calculated differences in velocity were also not evident following experimentation as the error of the Ruff and Ives [99] measurement method of particle velocity was determined to be an average of ± 9% which is similar in magnitude to the theoretical difference in velocity between the three erodents in the same size range of 106-125µm. Calculated differences in particle velocity between the two size ranges is even larger at 56% from 63-106µm fly ash (the fastest) to 106-125µm SiC (the slowest). The scatter of results from velocity testing of the three erodents and two size ranges showed a scatter of approximately the same magnitude as the error determined in the Ruff and Ives method (± 9%). In addition, the ranking of these erodents and two size ranges were not consistent within this scatter which is seen in Figure 7.3.

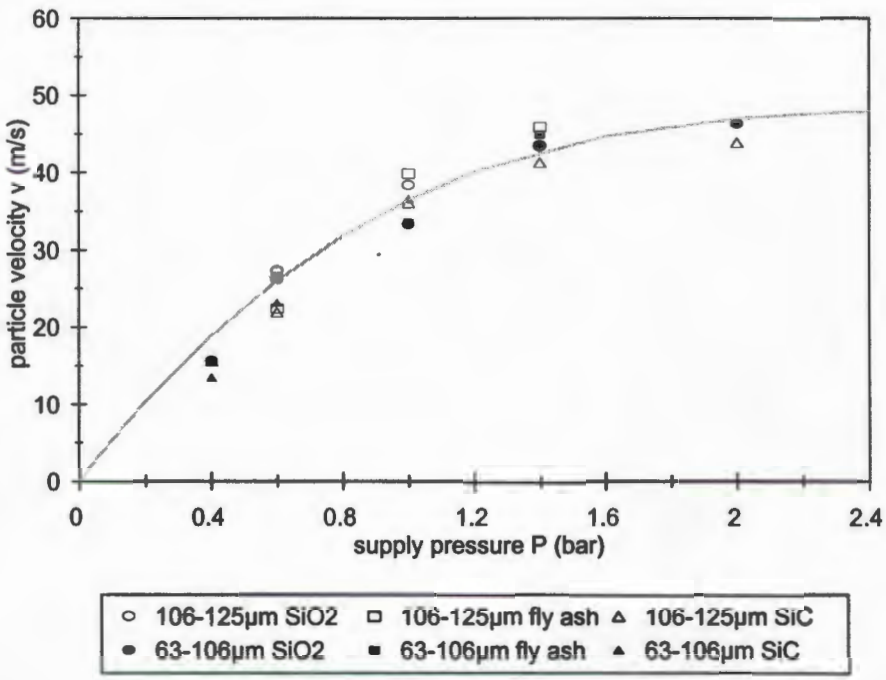

Figure 7.3 : Graph of particle velocity versus supply pressure for three erodents and two sizes. Note how the results are closely grouped making it difficult to distinguish between the three erodents as well as the different sized particles.

These anomolies between the calculated and experimental results of the particle velocities indicate that such calculations are flawed for two reasons. Firstly, the approach assumes undisturbed gas flow and is thus one dimensional, whereas the gas flow in the acceleration tube will have horizontal velocity flow components in addition to vertical velocity components due to the constraint of the tube. Secondly, although complex relationships have been derived to determine the drag coefficient of a sphere at Reynolds numbers from 0 - 70000, it could be an over-simplification determining drag coefficients of irregularly shaped particles based on the coefficient for the sphere. This results in exaggerated differences in the calculated velocities between the particle types and sizes.

7.2 The effect of mass flux

Few specific studies appear to have been conducted on the effects of mass flux on erosion rates despite its significance in the industrial situation such as power generation where coal ash flow varies greatly depending on boiler load. Anand et al [12] and Krishnamoorthy et al [5] however, found that erosion rates decreased with an increase in flux, attributing this observation to the effects of particle shielding of the specimen surface.

A decrease in erosion rates with an increase in particle flux was also found in the present work. In Figure 7.4 the erosion rate is shown plotted against particle flux for six different test temperatures. It can be seen that erosion rates measured for fluxes of $0.17 kg.m^{-2}.s^{-1}$ and $2.1 kg.m^{-2}.s^{-1}$ for different temperatures are similar. However, an increase in the flux above $2.1 kg.m^{-2}.s^{-1}$ results in a large decrease in the erosion rate.

This marked decrease is attributed to particle shielding. As the mass flux and hence the number of particles striking the surface increases, collisions occurring between rebounding and incoming particles also increase. Eventually a critical flux is reached when massive interaction occurs and any further increase in flux causes a significant decrease in erosion rates.

Such results support those of Shipway and Hutchings [26] who believe that the flux for a given test system may reach an optimum level, which was found to be 0.76kg.m^{-2}.s^{-1} at certain conditions in their apparatus. They found that at low particle fluxes using 215-250μm lead glass spheres at 45.5m.s^{-1} that the size of the scar formed by blasting a specimen increased with the natural logarithm of the mass of erodent used. However, as the flux was increased through a range of 0.008 to 45.7kg.m^{-2}.s^{-1} , this relationship deviated from being linear. They noted that this deviation was marked from a flux of 0.76kg.m^{-2}.s^{-1} upwards, indicating a transition in the particle - particle interaction mechanisms. This flux is intermediate to the range of fluxes of 0.17-2.1 kg.m^{-2}.s^{-1} in this study, where it is believed that the shielding effect becomes negligible.

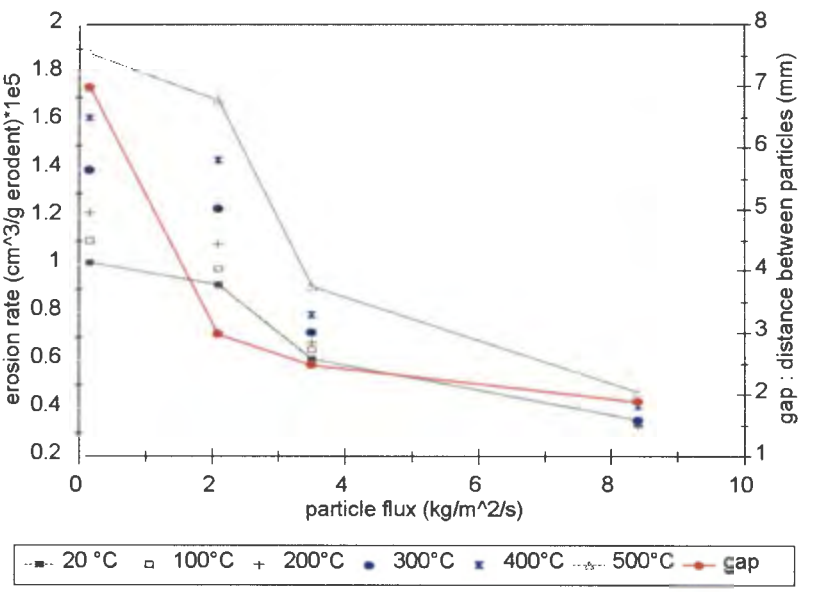

Figure 7.4 : Graph of erosion rate versus flux for several fluxes tested over a range of temperatures, using 106-125μm SiO_2 particles at 24m.s^{-1}. Note the sharp drop in erosion rate once the flux of 2.1 kg.m^{-2}.s^{-1} is exceeded. The calculated distance between the particles in the air stream is shown to compare with the trend of decreasing wear rates with increasing flux.

It is thought that the nature of the particle - particle interactions in the gas blast apparatus can be divided into two types :

a) Particle - tube interaction

At low fluxes in a gas blast apparatus, i.e. < 2.0kg.m^{-2}.s^{-1}, the particles experience interactions with the tube from the time that they are introduced into the gas stream. This slows the particles and partly accounts for their velocity being less than that of the gas [26,91].

The more particles that are introduced into the tube, the more particle - tube interactions take place. A drop in particle velocity as the flux increases can thus be expected. However, in this work no apparent change in particle velocity with particle flux was observed with the measuring system employed. This can be explained by comparing the inertia of the air to the inertia of the erodent particles. For an average air velocity of 64m.s^{-1}, which accelerates particles to a velocity of 24 ± 2m.s^{-1} , the mass flow rate m of the air = ρ*U*A

ρ = air density

U = air velocity

A = cross sectional area of nozzle / pipe

hence m = 6.03×10^{-3} kg.s^{-1}

and gas flux = 77kg.m^{-2}.s^{-1}.

Thus the inertia of the air outweighs that of the largest flux (8.4kg.m^{-2}.s^{-1}) by 9.1 times. It is thus not likely that changes in the erodent particle flux will have a significant effect on the final particle velocity.

b) Particle - particle interactions.

As the particle flux increases, particle - particle interactions are more likely in addition to particle - tube interactions, as the incoming particles begin to collide with particles rebounding off the target surface. The frequency of collisions between incoming and rebounding particles causes the specimen to become

progressively more 'shielded' as the flux increases. The specimen is therefore protected to an extent by the very barrage of erodent sent to damage it [5,12]. Significant specimen shielding will clearly contribute to a rapid decrease in erosion rate with an increase in flux.

From the work by Shipway & Hutchings [26] : $\mathbf{L = (m*V*\pi*r^2 / Q_0)^{1/3}}$

Where L = the average distance between successive particles
m = mass of each particle = 2.19×10^{-9} kg
(for the case of 106-125μm SiO_2 particles)
V = particle velocity = $24 m.s^{-1}$
r = radius of each particle = 116μm
(equivalent radius)
Q_0 = mass flow rate of the particles

If the flowrates from this work are labelled 1 - 4 from the lowest particle flow rate to the highest then :

Q1	=	$0.012 g.s^{-1}$,	flux	=	$0.17 kg.m^{-2}.s^{-1}$
Q2	=	$0.15 g.s^{-1}$,	flux	=	$2.1 kg.m^{-2}.s^{-1}$
Q3	=	$0.25 g.s^{-1}$,	flux	=	$3.5 kg.m^{-2}.s^{-1}$
Q4	=	$0.61 g.s^{-1}$,	flux	=	$8.4 kg.m^{-2}.s^{-1}$

and the corresponding average distances between successive particles are :

L1 = 570μm
L2 = 529μm
L3 = 207μm
L4 = 154μm

Clearly, if the particle velocity V is known, and the average distance L between them, then the average time between impacts is calculated as t = L/V.

e.g. for a flux of 8.4kg.m^{-2}.s^{-1}, the distance L between the particles is 154μm and the time t = 6.4μs.

For a flux of 0.17, L = 694 μm and t = 26.7 μs.

It can be seen from these figures that for an order of magnitude increase in particle flux from 0.17kg.m^{-2}.s^{-1} to 8.4kg.m^{-2}.s^{-1}, the time between impact decreases only 4.17 times. i.e. an increase by nearly two orders of magnitude in the particle flux does not result in the same magnitude of decrease in time between particle strikes.

These distances between particles for different fluxes are plotted on Figure 7.4 on the secondary axis. Here the decrease in successive particle - particle distance as a function of particle flux is seen to be marked between the fluxes of 0.17kg.m^{-2}.s^{-1} and 2.1kg.m^{-2}.s^{-1}. This transition is similar to the sharp transition shown in wear rates which occurs between fluxes of 2.1kg.m^{-2}.s^{-1} and 3.5kg.m^{-2}.s^{-1}.

7.2.1 The effect of mass loading in the system

Whilst the erosion rate can be graphed as a function of volume loss of material *per gram* of erodent, it is also helpful to determine the loss of material per unit time for practical purposes. In this way, the loss of material from a boiler tube for a given particle mass loading can be evaluated.

Thus, erosion rates in units of volume loss *per gram of impacting erodent* were converted to material volume loss *per second*, and graphed against temperature. Figure 7.5 illustrates that the greater mass fluxes of erodent result in a greater mass losses of material per unit time than low fluxes.

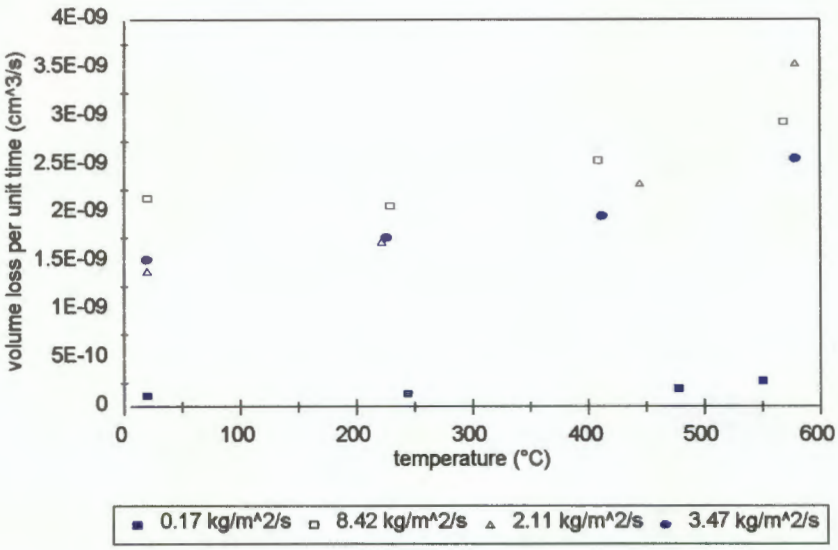

Figure 7.5 : Volume loss of HFS620 vs temperature to show the effect of a high mass loading on material volume loss for 106-125μm SiO_2 at 24m.s^{-1}.

At 20°C, a flux of 8.42 g.s^{-1} causes 14.8 times more volume loss of material per unit time than a flux of 0.17kg.m^{-2}.s^{-1} This result was obtained when using 106-125μm SiO_2 at 24m.s^{-1}. However, the greater shielding effect of the higher flux is still prevalent. Although approximately 14.8 times greater material loss is experienced using a flux of 8.42kg.m^{-2}.s^{-1} there is 49 times more erodent bombarding the target surface. Figure 7.5 shows a noticeable gap in the volume loss in unit time between the lowest flux and the intermediate fluxes at all temperatures.

The reasons for the behaviour of the system as described, is connected with the total energy in the system. With a large increase in the mass of erodent particles there is an associated increase in the kinetic energy available to be transferred to the target surface. However, although the increase in mass of the erodent in the system is 49 times greater from the highest compared to the lowest flux, the same increase is not reflected in the wear rate due to the marked shielding effect which occurs at high fluxes. This results in a drop in the efficiency at which energy from the erodent is transferred to the target surface.

These results were then graphed against flux to show the variation between volume loss per second and flux (see Figure 7.6). A sharp increase in loss rates is seen from the flux of 0.17 to 3.47kg.m^{-2}.s^{-1} . The lower limit shown is the best fit curve of results at room temperature and the upper results at high temperature. The results shown in Figure 7.6 are particularly significant because they include the effect of temperature. An increase in mass loading in a high temperature system results in a more noticeable increase in volume loss of material per unit time than at low temperature.

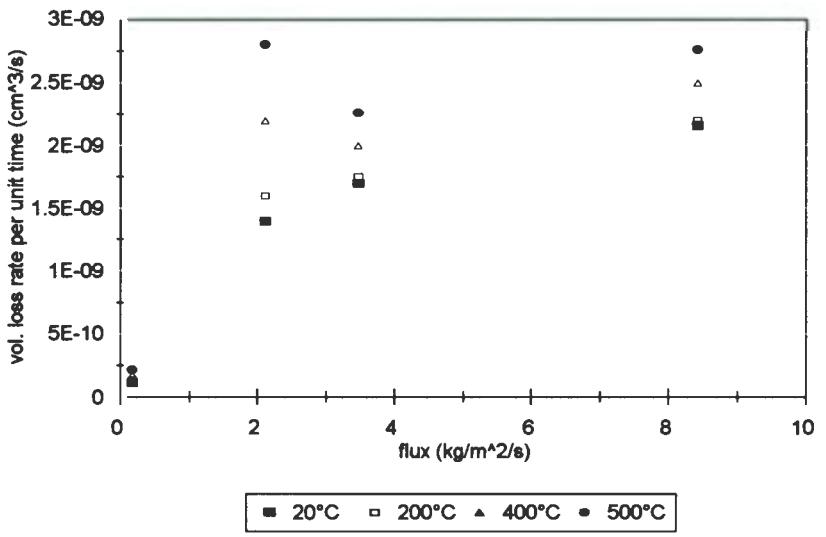

Figure 7.6 : Volume loss rate vs flux for the HFS620 where a sharp increase in material loss rates can be seen with increasing flux as well as with increasing temperature.

7.2.2 The effect of oxidation on erosive wear rates

Oxidation does occur during high temperature erosion testing which is evidenced in scanning electron micrographs of damaged surfaces where chips of oxide can be seen adjacent to impact craters. This can be seen in Figure 7.7(a) & (b) which show single impact sites on a specimen bombarded by 106-125μm SiC particles at 33m.s^{-1} .

Oxidation has a significant effect on high temperature erosion rates in fluidised bed conditions where a change in wear mechanism with increasing temperature occurs. At low temperatures the erosion process dominates whilst at high temperatures, the growth of an oxide layer results in a protective effect on the substrate and overall wear rates decrease. These changes result in a peak in the erosion rate versus temperature curve, where the synergistic erosion / oxidation wastage mechanism has the greatest effect. This peak is followed by a drop in the rate of material loss to a level comparable to that experienced at room temperature [8,51].

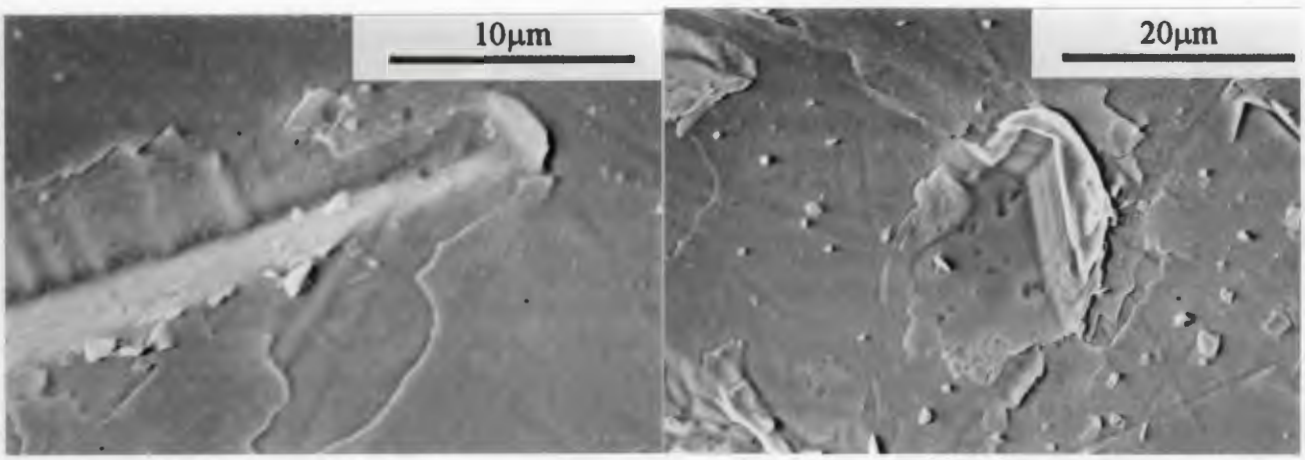

(a) *(b)*

Figure 7.7 : Regions of specimens eroded at 500°C at 33m.s^{-1} by 106-125μm SiC particles and a flux of 2.3kg.m^{-2}.s^{-1}.

It is interesting to note that opinion on whether the oxide layer assumes a protective role or not is divided in the literature. The fracture and loss of an oxide layer [55,56] would indicate a continuous wastage process. Ohlsson et al [54] claim that the layer Is *not* likely to give protection, whilst MacAdam and Stringer [4] suggest any protection that may exist is due to a duplex layer of erodent and oxide.

Whether the oxide layer acts as a protective barrier or not, the oxidation of specimens during high temperature erosion testing influences wear rates. The growth of an oxide layer will clearly lead to a mass gain. In this work the mass gain of an HFS620 specimen oxidised for 6¾ hours at 600°C was found to be 2.914mg when normalised for the elliptical crater cross section. This is an order of magnitude less than mass loss data extrapolated from 76 minutes of erosion testing to 6¾ hours when using 106-125μm fly ash particles at 24m.s^{-1} and a flux of 0.17kg.m^{-2}.s^{-1} . The same order of magnitude difference applies to erosion by SiO_2 and SiC particles of a similar size in similar operating conditions.

However, such comparisons have to be viewed with caution since the intermittent removal and subsequent oxidation of virgin surfaces may result in the role of oxidation being more significant on wear rates. Clearly the extent of oxide growth in the time between successive particle impacts is of concern, which is an issue also identified by Wright et al [60].

If a fixed damage crater area of 339mm^2 is assumed then the parabolic rate constant for oxidation growth is 3.52x10^{-16} at 600°C. This parabola is seen in Figure 7.8. A simple analysis was performed to compare the mass gain due to oxidation and the mass gain due to erosion over an area equivalent to an impact site on a target eroded by ash particles at 24m.s^{-1}. The results of this simple analysis are shown in Table 7.2 where it is seen how the mass gain due to oxidation is comparable to the mass loss due to erosion when the approximate area of a single impact site is examined.

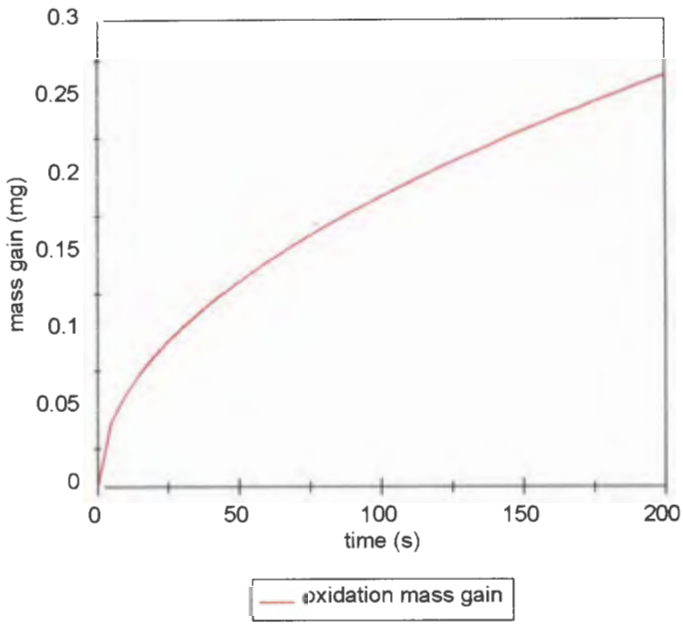

Figure 7.8 : The rate of oxide layer growth on an erosion scar area of 339mm^2 at a temperature of 600°C.

Whilst metallographic evidence shows that erosion in these specific conditions is the primary cause of material loss, this analysis of oxide layer growth between successive particle impacts emphasizes that within the time scales relevant to these conditions, oxide layer growth is a competing process to pure erosion and will influence the total erosion rate.

Average particle radius (assuming spherical particles)	116μm
Mass feed rate of particles (for a particle flux of 0.17kg.m^{-2}.s^{-1})	0.012g.s^{-1}
Total erodent used in 6¾ hours	299g
mass of one ash particle	1.626x10^{-6} g
total number of particles	184x10^{6}
number of particle strikes to cover the entire damage crater	678x10^{3}
approximate area of one strike	500x10^{-12} m^{2}
approximate number of times the same area is struck in 6¾ hours	271
time between successive strikes	90s
oxide mass gain per 90s using the parabolic relationship	**262x10^{-9} mg**
erosion mass loss per strike	**125x10^{-9} mg**

Table 7.2 : A list of the order of the steps taken and assumptions made, when determining the relative effects of oxide mass gain and erosion mass loss over the area of a single impact site.

Whether the oxide layer acts as a protective barrier to the underlying material could thus be a function of the kinetic energy of the erodent particles. The kinetic energy of the particles in the gas blast system exceeds that of particles fluidised beds by between 2 and 3 orders of magnitude. This energy difference clearly shows that the same pattern of wear behaviour observed in fluidised bed conditions will not be seen in the gas blast situation. Wear regimes in the gas blast situation will thus be erosion dominated and will not move from being erosion dominated at low temperatures to corrosion dominated at high temperatures, which is in agreement with Kang et al [53]. Since the mass loading, or flux of particles is high in fluidised bed conditions, it is clearly the low kinetic energy of these particles which cannot easily remove the oxide layer which covers the underlying material. To encourage oxide layer growth in the much higher particle velocity gas blast apparatus, the particle flux was reduced to increase the time between successive particle impacts. Despite lowering the flux from 8.4kg.m^{-2}.s^{-1} to 0.17kg.m^{-2}.s^{-1} no peak in wear rate was evidenced with an increase in temperature.

Another check was performed to characterise the influence of mass flux in determining the nature of the wear regime. The ratio of erosion rates from low to high fluxes ranges were compared from room temperature to 500°C, the results of which are seen in Table 7.3.

temperature (°C)	erosion rate (for a flux of $8.4kg.m^{-2}.s^{-1}$) $x10^{-5}$	erosion rate (for a flux of $0.17kg.m^{-2}.s^{-1}$) $x10^{-5}$	ratio of erosion rates from fluxes 0.17/8.4
20	0.354	1.01	2.85
100	0.338	1.10	3.25
200	0.329	1.22	3.71
300	0.353	1.40	3.97
400	0.412	1.62	3.93
500	0.471	1.88	3.99

Table 7.3 : Erosion rates from the best fit curves of erosion rate versus temperature for fluxes of 0.17 and $8.4kg.m^{-2}.s^{-1}$ using 106-125μm SiO_2 at $24m.s^{-1}$.

The ratio of wear rates from a flux of 0.17 to $8.4kg.m^{-2}.s^{-1}$ ranged from 2.85 at 20°C to 3.99 at 500°C. This result suggests that the time between impacts, ranging from 6.4μs at the highest flux, to 24μs at the lowest, does have an influence on the overall wear rate and that a thicker oxide layer is able to develop at the lower flux resulting in greater wear as chips of oxide are removed in addition to material being lost from pure erosion processes.

An additional surface effect contributing to the overall mass loss is surface decarburisation which was also found on the steel at elevated temperatures. This decarburisation develops as a result of the high temperature oxidising conditions prevalent in the system. De-carburisation is evidenced by large ferrite grains and an absence of pearlite as the carbon in the cementite bands combine with oxygen to form ferrous oxides (Fe_xO_y) at the material surface and carbon is removed as carbon dioxide (CO_2).

These decarburised layers can be seen in Figure 7.9, which shows optical micrographs of cross sections of specimens eroded by 106-125μm ash at $24m.s^{-1}$ at different

temperatures. At room temperature there is no carbon depleted zone at the surface, with ferrite and pearlite occurring in continuous bands. However, as the temperature is increased the zone of decarburisation becomes thicker.

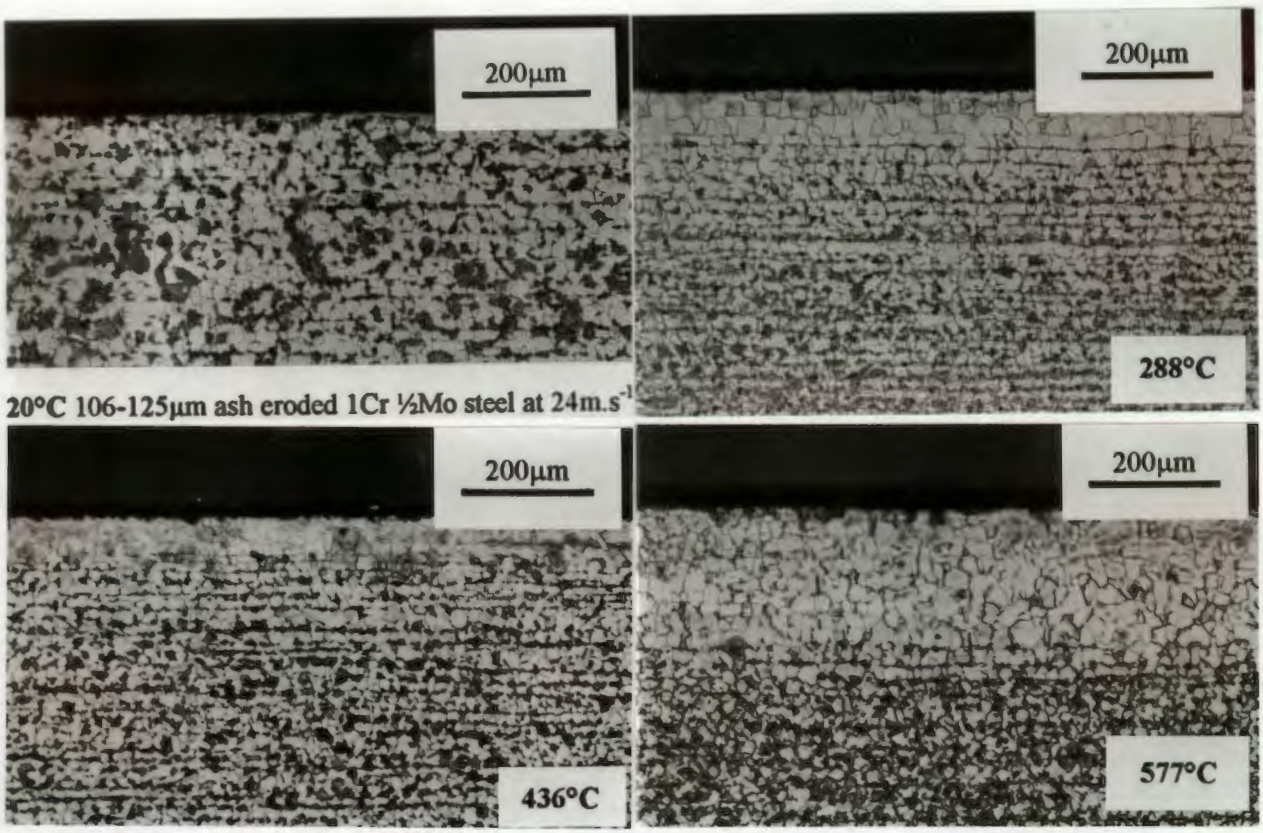

Figure 7.9 : Optical micrographs of ash eroded specimens, showing the increase in the depth of the decarburised zone with an increase in the target specimen. Specimens at temperatures > 20°C spent 76 minutes on average at the temperatures shown.

The implication of this decarburised zone on high temperature erosion is that the carbon depleted zone lacks the strength of the bulk material, facilitating easier material removal and resulting in higher erosion rates. This significant drop in the strength of the surface is shown in Figure 6.20 which maps the cross sectional microhardness profiles of steel specimens eroded by 106-125μm ash particles at 24m.s^{-1} across a range of temperatures. A lower surface hardness of the eroded specimen at 577°C clearly indicates the presence of a softened, decarburised zone.

7.2.3 The Depth of the plastic zone

In addition to a drop in the hardness in the immediate subsurface of the steel specimens that was noted with an increase in temperature, the depth of the plastic zone caused by erodent particles also increased with increasing temperature. This increase in plasticity is seen to relate directly to the erosion rate. This analysis was performed on specimens eroded by 106-125µm fly ash at a particle velocity of 24m.s^{-1} and a flux of 0.17kg.m^{-2}.s^{-1}. The depth at which readings deviate from the steel's bulk hardness of 220 Knoop is shown as a function of temperature in Figure 7.10.

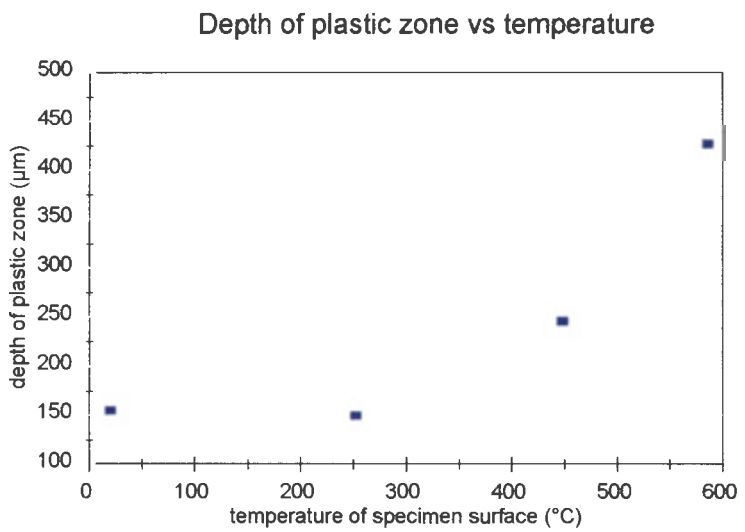

Figure 7.10 : Graph showing the increase in plastic zone depth as a function of temperature, the zone appearing to increase markedly in size with temperature.

The depth of the plastic zone increases markedly with temperature and is similar to the trend shown of an increase in erosion rate with temperature. In Figure 7.11 the depth of the plastic zone is plotted against erosion rate for a range of temperatures. A linear relationship is obtained indicating a direct correlation between erosion rate and plasticity of the steel.

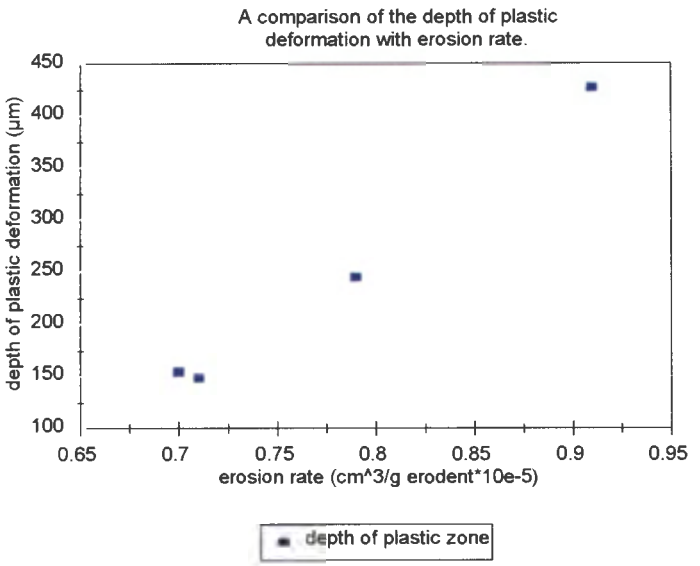

Figure 7.11 : Depth of plastic deformation graphed against erosion rate for 106-125µm ash impacted steel at 24m.s^{-1} and a flux of 0.17kg.m^{-2}.s^{-1}.

7.3 Cumulative heating effects due to successive particle strikes

The energy associated with the deformation of the material during a particle strike is largely converted to heat. If the time between particle impacts is low, then it is possible that the heat generated by an impact is not dissipated sufficiently quickly (i.e. adiabatic conditions are assumed) and there is a cumulative heating effect which may result in localised melting of material. However, it is more likely that any temperature rise would result in the lowering of the flow stress of the steel leading to increased material erosion rates [103].

Hutchings and Levy [70] as well as Doyle and Ball [71], used a simple heat diffusion model to compare the time taken for the heat generated by a particle impact to diffuse into the bulk of the material, to the time between successive particle impacts. Eroding 1100 and 7075 T6 aluminium alloys with 250μm SiC particles at $30m.s^{-1}$, Hutchings and Levy found that a cumulative heating effect, detected by a temperature rise at the surface of the target, is only possible when dealing with very high particle fluxes. In addition, they concluded that the maximum rise in temperature would be very much less than the adiabatic model. Doyle and Ball however, when eroding a 1030 carbon steel with 106-125μm SiC particles at $30m.s^{-1}$ calculated that adiabatic conditions were almost achieved and that a local temperature rise at particle impact of 500K could result.

A similar analysis of the possible rise in surface temperature of the 1Cr½Mo steel employed in this work has been made. An assumption of adiabatic conditions is made due to the velocity of an impact event. This analysis includes the effect of specimen temperature, changes in the material's thermal properties (thermal conductivity) and mechanical properties (a drop in hardness) as a function of increasing temperature. Thus:

ΔT = the mean adiabatic temperature rise

ΔT = $P/C_t\rho_t$

P = pressure resisting indentation (i.e. hardness)

= 1.67 Gpa (at 100°C)

C_t = specific heat of steel

= 0.46 kJ/kg°C

ρ_t = density of steel

= $7865\ kg.m^{-3}$

= **462 K** for the steel under examination

The depth of the plastic zone can be determined assuming normal particle impact and normal rebound.

x_p = depth of the plastic zone

$$x_p = r_e * v_e * (2 * \rho_t / 3 * P)^{0.5}$$

The case of a specimen temperature of 100°C is taken as an example :

r_e = radius of the erodent particle
= 106×10^{-6} m
v_e = vel. of the erodent particle
= 24 $m.s^{-1}$
ρ_t = density of steel
= 7865 $kg.m^{-3}$
P = 1320MPa

Thus x_p = **5.07µm**

To find the time of deformation associated with impact it is first necessary to find the ratio between x_p and x_d , the root mean square diffusion distance of heat from the impact site.

$$x_p / x_d = v_e * (r_e / 3 * \pi * k)^{0.5} * (2 * \rho_t / 3 * P)^{0.25}$$

k = thermal conductivity
= 55W/m°C at 100°C

$$x_d = (6 * k * t_p)^{0.5}$$

t_p = time of deformation

as x_p / x_d = 0.914 at 100°C,
t_p = 0.11 µs at 100°C

The resultant information calculated at two specimen temperatures of 100 and 600°C is shown summarised in Table 7.4. A difference of 2 orders of magnitude can be seen between the time between particle impacts and the time of deformation (Table 7.4). It is interesting to note that the ratio of depth of the plastic zone x_p and the root mean square diffusion distance x_d of heat from the impact site is 485×10^{-6} at 100°C and 837×10^{-6} at 600°C. This shows evidence of predominantly isothermal conditions [70]. Thus conduction of heat occurs away from the surface of the target steel. This implies that any

temperature rises due to particle impact will not be as great as that predicted when assuming adiabatic conditions. Indeed, according to Hutchings and Levy [70], in many practical cases of erosion, the maximum rise in temperature will be significantly lower than that of the adiabatic model.

Parameter	Property at 100°C	Property at 600°C
pressure resisting indentation (i.e. hardness) **P**	1320MPa	300MPa
thermal conductivity **k**	55W/m°C	36 W/m°C
x_p/x_d	$485x10^{-6}$	$867x10^{-6}$
depth of the plastic zone x_p	5.07μm	10.64μm
the root mean square diffusion distance x_d	10.46mm	12.30mm
time of deformation t_p	0.332μs	0.700μs
time between impacts t_i for a flux of $0.17kg.m^{-2}.s^{-1}$.	24μs	24μs

Table 7.4 : Summarised data from the thermal diffusion model.

Further, it can be assumed that localised melting as a mechanism accelerating erosive wear is not a significant effect during erosion of steels. The average time between particle impacts is two orders of magnitude greater than the time taken for heat generated by the particle impact to diffuse through the specimen. Thus, there is not likely to be a significant cumulative heating effect.

The change in thermal and mechanical properties of the specimen as a function of increasing temperature does change the depth of the plastic zone x_p, the root mean square diffusion distance x_d and the time of deformation t_p. However, these changes are not significant in comparison to the time between particle impacts which allows the dissipation of heat from the surface.

In addition, the assumption of adiabatic conditions when calculating the maximum temperature rise upon particle impact yields a value greater than will occur in most practical situations. Thus, the conditions at the impact site are dominantly isothermal

which is in agreement with Hutchings and Levy [70] but contrasts with Doyle and Ball [71].

7.4 The effect of particle velocity

The particle velocities in this work spanned a range from 24 to 51m.s^{-1}. It was therefore possible to determine a velocity exponent as a function of temperature. This was performed in the following way. Relationships between the erosion rate and temperature were established for the 20-200°C wear regime and then the 250-450°C range for SiC and SiO_2. Velocity tests using fly ash were limited to one temperature (20°C) due to the difficulties of procuring sufficient ash to perform the entire range of velocities and temperatures. Two relationships were thus derived for each particle velocity in the form of :

$$E = k_i * T^{ni} \text{ and } E = k_f * T^{nf}$$

E = erosion rate
T = temperature
k_i = erosion constant for the 20-200°C wear regime
ni = temperature exponent for the 20-200°C wear regime
k_f = erosion constant for the 200-450°C wear regime
nf = temperature exponent for the 200-450°C wear regime

Erosion rates for 20, 100, 300 and 450°C were then calculated. At each different temperature, the relationship :

$$E = k_v * V^{nv}$$

k_v = erosion constant
V = particle velocity

nv = velocity exponent

was converted to :

$$\ln(E) = \ln(k_v) + nv*\ln(V)$$

The exponent nv could then be found from a linear regression of these results which are summarised in Table 7.5. As mentioned, a velocity exponent for fly ash was derived for a single temperature of 20°C.

temperature	**velocity exponent nv**		
°C	fly ash	SiO_2	SiC
20	1.90	2.12	2.16
100	-	2.12	2.16
300	-	1.98	2.00
450	-	1.87	1.73

Table 7.5 : Table listing erosion rates for 3 set temperatures and 4 velocities for 106-125μm SiO_2 particles at a flux of 2.1kg.m^{-2}.s^{-1}.

The velocity exponent of the ash at 20°C is 1.90. The exponent drops from 2.12 at 20°C to 1.87 at 450°C when using SiO_2. A similar trend is seen when using SiC particles where the exponent drops from 2.16 at 20°C to 1.73 at 450°C. The ash velocity exponent is 10% less than the SiO_2 and the SiC particles. This is thought to be due to the ash's non-uniform structure causing it to absorb energy on impact and fracture as opposed to transferring energy to the target material.

The fact that the velocity exponent obtained from the SiO_2 and SiC tests straddles the value of 2 which is a value found by other researchers [13,29,48] when testing ductile materials, is encouraging. The physical significance of the exponent value decreasing with increasing temperature is that the target material becomes less sensitive to changes in velocity as temperature increases.

This is due to the change in the mechanical properties of the material with temperature. Tensile testing shows a decrease in strength and an increase in ductility with rising temperature. The drop in strength implies a drop in the energy required to cause

plastic deformation, whilst the increase in ductility implies that more plastic deformation will result per particle strike. If the dominant material removal mechanism relies on the work - hardening of lips and ridges to fracture [47,48], then the changing mechanical properties of the material with temperature would clearly influence this process.

It is interesting to note that the velocity exponent of the commercial electric arc sprayed coatings is 1.64 at room temperature. This is a significant difference compared to the bare substrate at this temperature which has an exponent of 2.12. It is thought that this apparent insensitivity to changes in particle velocity is due to the higher strength of the coating which allows it to respond elastically to many impacts. This was evidenced in cross-sectional microhardness profiles of the as received coating surfaces. Coating 1 and 2 had as-received hardnesses of 375 and 340 Knoop respectively. This is in comparison to the average hardness of an uncoated specimen of 220 Knoop.

In addition, the low value indicates a difference in response to impact than an homogeneous material. This is possibly due to the porosity within the coating. The pores within the coating platelets could act as energy dampers to impact where energy dissipation is proportional to impact velocity or pore compression. In addition, the bond between the coating and substrate relies on friction between the two materials. This is well illustrated in Figure 6.29 and 7.12. The interface between the coating and the substrate is also a possible site for energy dissipation as the elastic response of the coating would cause relative movement between the two different materials.

Although inconsistencies such as porosity and impurities (as seen in Figure 7.12) may change the coating's sensitivity to velocity, these and other features such as the nature of the bond between the coating and the substrate result in much higher wear rates than the bare substrate.

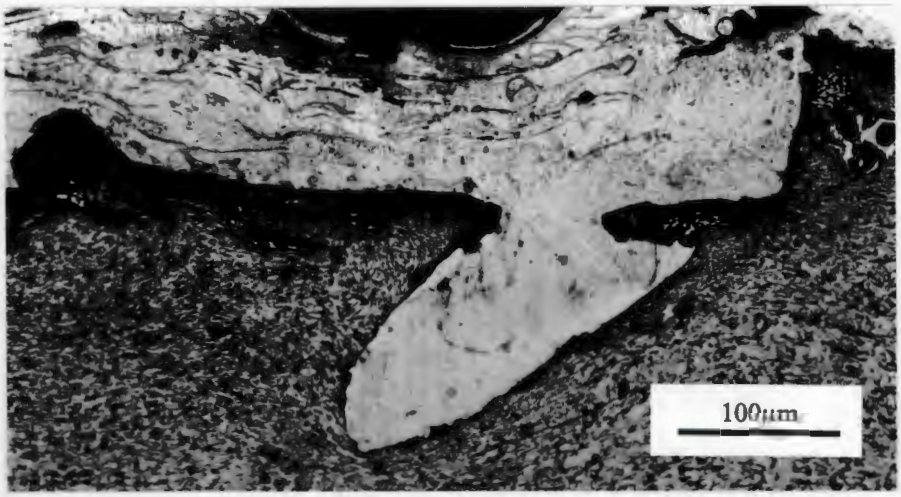

Figure 7.12 : Optical micrograph of coating 1. A distinct gap can be seen in areas where the coating has not adhered to the substrate.

7.5 The change in the response of the target to particle impact as a function of temperature

Levy et al [42] removed the effect of oxidation from their high temperature erosion tests on austenitic and ferritic steels by conducting tests in an inert gas. Nitrogen was used in a high temperature gas blast apparatus to blow 240-325μm SiC particles at 30m.s^{-1} and a mass loading of 10g.min^{-1} at the target specimen. They found that an increase in erosion rate with temperature is directly related to a decrease in the tensile strength of the test material.

Results of the present tensile testing of the target steel show a decrease in yield strength and an increase in ductility with an increase in temperature up to 600°C. These values are shown plotted against erosion rate in Figure 7.13 where a linear relationship was found between strength reduction and ductility increase and increasing erosion rates with temperature.

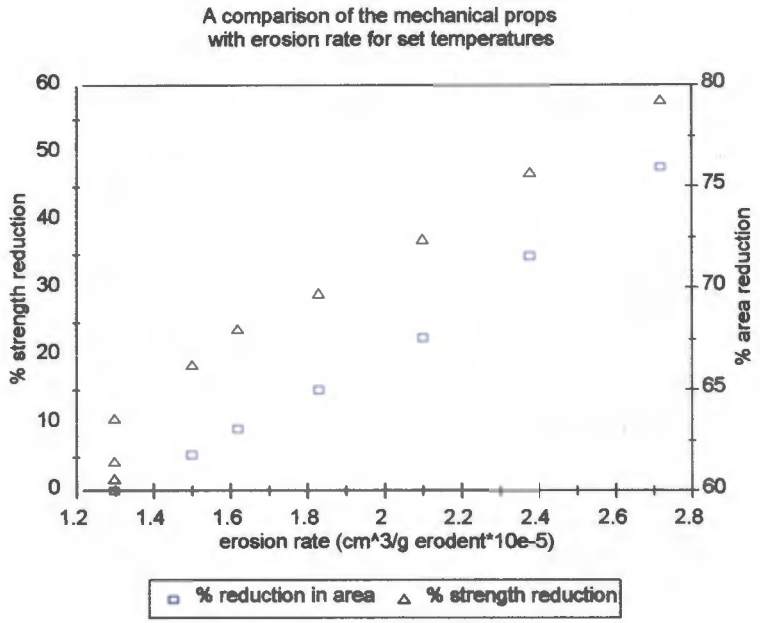

Figure 7.13 : % Reduction in area and % red. in strength of the tested steel shown graphed against ero. rate. The linearity of the trend suggests a relationship between the changing mech. props of the material and ero. rate with increasing temp.

The data used in Figure 7.13 is summarised in Table 7.6. Data was extracted from best fit curves.

temperature (°C)	erosion rate (cm3/g ero.x10^{-5})	reduction in area (%)	reduction in yield strength (%)
50	1.3	60.0	1.8
100	1.3	60.0	4.4
200	1.3	60.0	10.7
300	1.5	61.8	18.7
350	1.6	63.1	24
400	1.8	65.0	29.3
450	2.1	67.6	37.3
500	2.4	71.6	47.1
550	2.7	76.0	57.8

Table 7.6 : A summary of the data used in the comparison of mech. props with erosion rates.

In Figure 7.14 the natural logarithm of the erosion rate is plotted against the natural logarithm of the specific heat capacity of the material multiplied by the difference between the material's melting temperature and its actual temperature. This is for several velocities (24, 33, 41, 51m.s^{-1}) and a possible inflection point is observed. This data is summarised in Table 7.7 where it is also seen that there is an upswing in erosion rates which occurs over a narrow band of temperatures. This shows the presence of a change in the material's response to particle impact.

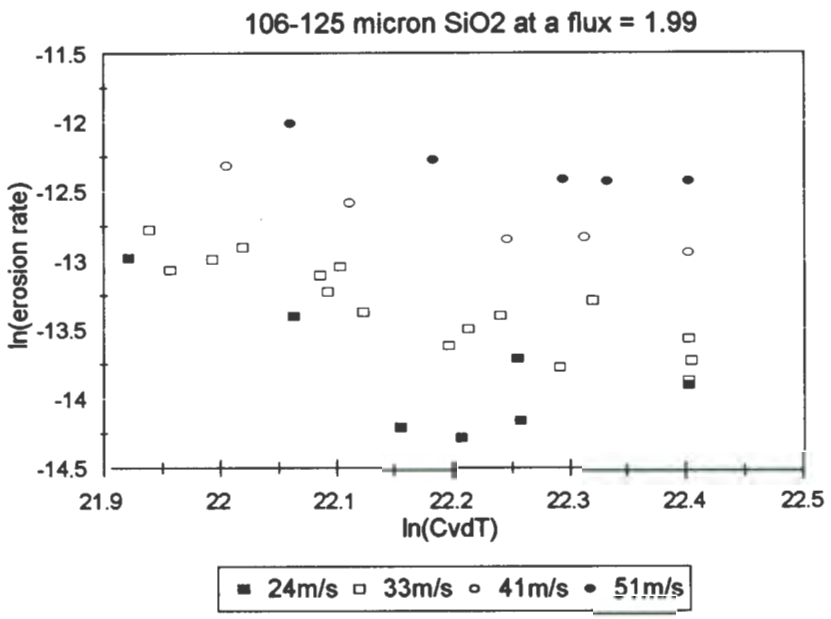

Figure 7.14 : Graph of the natural logarithm of erosion rate vs the natural logarithm of the specific heat of the steel multiplied by the difference in temp. of the specimen from its melting temp.

particle velocity m.s^{-1}	temperature at which transition occurs °C (± 60°C)
24	290
33	277
41	234
51	172

Table 7.7 : A list of the temperatures at which an upswing in erosion rates is seen, and the velocities at which this occurs.

This approach was adopted from Hutchings [104] who suggested that it is necessary to take into account the heat capacity of metals when comparing the erosive wear rates of different metals. This due to the high rate of strain caused by an impacting particle, resulting in near adiabatic conditions along the shear planes of the material. Thus, the tendency of a surface to thermal softening is enhanced by a low heat capacity and a low melt temperature. The erosive wear of a material is thus inversely proportional to its heat capacity multiplied by the difference between the melting point of the material and the ambient temperature.

As the particle velocity increases the strain rate at the material surface increases. This has two effects; firstly a higher strain rate results in a higher localised temperature rise which lowers the flow stress of the material. Secondly, a greater material plastic zone develops. This is seen in the relationship $x_p = r_e * v_e * (2 * \rho_t / 3 * P)^{0.5}$. Material hardness **P** decreases with increasing temperature which results in a larger depth of plastic zone x_p as seen in Figure 7.11 and noted in Table 7.4. This explains the general increase in erosion rates with increasing temperature. However, it is the first effect which explains the lowering of the temperature at which erosion rates begin to increase markedly as seen in Figure 7.14 and Table 7.7.

A point is reached where the temperature rise of the target surface due to particle impact added to the target bulk temperature results in material recovery. This causes a drop in strength of the material and subsequent increase in erosion rates. Hence the higher the particle kinetic energy, the greater is the resultant temperature rise at the surface of the target which causes erosion rates to start increasing rapidly at progressively lower temperatures.

References

[1] W. Tabakoff & B.V.R. Vittal, *High temperature erosion study of INCO 600 metal*, Wear 86, 1983, 89-99.

[2] D.J. Stephenson, J.R. Nicholls & P. Hancock, *Particle-surface interactions during the erosion of a gas turbine material (MarM002) by pyrolytic carbon particles*, Wear 111, 1986, 15-29.

[3] H. Gruber & K. Reinhard, *Long-Term Experience With Erosion in Wet Steam Turbines*, Combustion, March 1979, 11-14.

[4] S.S. MacAdam & J. Stringer, *Temperature Dependence of Steel Wastage in a bubbling Fluidized Bed Simulator*, Corrosion 49 (2), Feb. 1993.

[5] P.P. Krishnamoorthy, S. Seetharamu & P. Sampathkumaran, *Influence of the mass flux and Impact angle on the erosion resistance of materials used in pulverized fuel bends and other components in thermal power stations*, Wear 165, 1993, 151-157.

[6] E. Raask, *Tube erosion by fly ash impaction*, Wear 13, 1969, 301-315.

[7] M.M. El-Wakil, *Powerplant Technology*, McGraw-Hill, 1984.

[8] M.M. Stack, F.H. Stott & G.C. Wood, *Review of the mechanisms of erosion-corrosion of alloys at elevated temperatures*, Wear 162-164, 1993, 706-712.

[9] S. MacAdam & J. Stringer, *Development of a unique laboratory scale fluidized bed wear testing unit*, Wear 135, 1990, 403-422.

[10] M. Liebhard & A.V. Levy, *The effect of erodent particle characteristics on the erosion of metals*, Wear 151, 1991, 381-390.

[11] A.V. Levy & P. Chik, *The effects of erodent composition and shape on the erosion of steel*, Wear 89 (2), 1986, 151-162.

[12] K. Anand, S.K. Hovis, H. Conrad & R.O. Scattergood, *Flux effects in solid particle erosion*, Wear 118 (2), 1987, 243-257.

[13] I. Finnie & D.H. McFadden, *On the velocity dependence of the erosion of ductile metals by solid particles at low angles of incidence*, Wear 48 (1), 1978, 181-190.

[14] P.M. Rogers, T.E. Howes, I.M. Hutchings & J.A. Little, *Wastage of low alloy steels in a fluidised bed environment*, Wear 186-187, 1995, 306-315.

[15] Y.Liu & A.V. Levy, *The influence of test parameters on material wastage in a fluidised bed wear test rig*, Wear 151 (2), 1991, 365-379.

[16] B. Dooley, *Boiler tubes : Fly ash erosion of boiler tubes*, E.P.R.I. Jan 14, 1989, 54-56

[17] P. Mayer, *Boiler tubes : Boiler tube failure mechanism*, C.I.M. Bulletin 83, July 1990, 92-95

[18] E. Raask, *Erosion wear in coal utilisation*, Hemisphere publishing corp., 1988.

[19] D. Gibson, *Boiler Erosion, Report No. TRR/P92/118*, Eskom Technology Research and Investigations, Cleveland Johannesburg, December 1992.

[20] J. Stringer, *Practical experience with wastage at elevated temperatures in coal combustion systems*, Wear 186 - 187, 1995, 11-27.

[21] S.D. Strauss, *Boiler tubes : Tube life projection keyed to oxide scale measurements*, Power 133:60, December 1989.

[22] D. Stans (Eskom), *Boiler performance indicators*, Tutuka Power Station Unit 1, Schedule C23, February 1 1982.

[23] R.W. Taylor & T.E. Shell, *Ash fouling and erosion of silicon - based ceraminc expanders in coal fired power plants*, Lawrence Livermore Laboratory Publication UCRL - 52390, University of California 1978.

[24] A.G. Lorenzato & P.J. Blackbeard, *Collection, Storage and Transport of Ash at large Power Stations in South Africa*, Ash - a valuable resource S.387 (4), CSIR, Pretoria, 1987.

[25] T. van Niekerk & C. Wicker, *Private Communication*, Eskom Technology Research and Investigations Cleveland Johannesburg South Africa, 8 March 1995.

[26] P.H. Shipway & I.M. Hutchings, *A method for optimising the particle flux in erosion testing with a gas blast apparatus*, Wear 174, 1994, 169-175.

[27] A.V. Levy, E. Slamovich & N. Jee, *Elevated temperature combined erosion / corrosion of steels*, Wear 110 (2), 1986, 117-149.

[28] I. Finnie, *Erosion of surfaces by solid particles*, Wear 3, 1960, 87-103

[29] G.L. Sheldon & A.Kanhere, *An investigation of impingement erosion using single particles*, Wear 21, 1972, 195-209.

[30] S.S. MacAdam & J. Stringer, *Particle Impact and Impact Distribution within a fluidised bed combustor environment*, Wear 141, 1991, 373-394.

[31] W. Tabakoff, A. Hamed & B. Beacher, *Investigation of gas particle flow in an erosion windtunnel*, Wear 86, 1983, 73-88.

[32] S. Dosanjh & J.A.C. Humphrey, *The influence of turbulence on erosion by a particle laden fluid jet*, Wear 103, 1985, 309-330.

[33] S.L. Palasamudram & S. Bahadur, *Particle Characterization for Angularity and the effect of Particle size and Angularity on Erosion in a Fluidized bed Environment, Wear of Materials*, San Diego 1997 in press.

[34] I.M. Hutchings, *Recent advances in the understanding of solid particle erosion*, Mechanique, Materiaux, Electricite 365-366, 1980, 185-192.

[35] G.L. Bosch, *The mineralogy and chemistry of pulverised fuel ash produced by three South African Coal-burning power stations,* University of Cape Town M.Sc. Thesis, March 1990.

[36] W. Lesch & D.H. Cornell, *The Mineralogy and Morphology of Fly Ash from South African Power Stations*, Ash - A valuable resource S387, Vol. 3, CSIR, Pretoria South Africa, 1987.

[37] R.J. Lauf, *Microstructure of Coal Ash Particles*, Am. Ceram. Soc. Bull., 61 (4) 1982, 487-490.

[38] P.H. Shipway & I.M. Hutchings, *Influence of nozzle roughness on conditions in a gas blast erosion rig*, Wear 162-164, (1993), 148-158.

[39] R.H. Barkalow, *Material problems in fluidized bed combustion systems*, Pratt & Whitney Aircraft Group, East Hartford, Connecticut, Ref : 80 - 200 - 7082 - FR 1, October 1980.

[40] I. Finnie, J. Wolak & Y. Yabin, *Erosion of metals by solid particles, Journal of Materials*, Vol 2, No 3, Sept 1967.

[41] C.E. Smeltzer, M.E. Gulden & W.A. Compton, *Mechanisms of metal removal by impacting dust particles*, Journal of Basic Engineering, 92, 1970, 639-654.

[42] A.V. Levy, J. Yan & J. Patterson, *Elevated temperature erosion of steels*, Wear 108 (1), 1986, 43-60.

[43] G. Sundararajan, *A comprehensive model for the solid particle erosion of ductile materials*, Wear, 149 (1991) 111-127.

[44] J.G.A. Bitter, *A study of erosion phenomena*, Wear 6, 1963, 169-190.

[45] J.H. Neilson & A. Gilchrist, *Erosion by a stream of solid particles*, Wear 11, 1968, 111-122.

[46] G.P. Tilly, *A two stage mechanism of Ductile Erosion*, Wear 23, 1973, 87-96.

[47] A.V. Levy, *The Platelet Mechanism of Erosion of Ductile Metals*, Wear, 108 (1), 1986, 1-22.

[48] A.V. Levy, M. Aghazadeh & . Hickey, *The effect of test variables on the platelet mechanism of erosion*, Wear 108, 1986, 23-41.

[49] A. Ball, *On the importance of work hardening in the design of wear resistant materials*, Wear 91, 1983, 201-207.

[50] M.M. Stack, F.H. Stott & G.C. Wood, *Erosion/Corrosion of pre-oxidised Incoloy 800H in fluidised bed environments : effects of temperature, velocity and exposure time*, Materials Science and Technology 7, December 1991, 1128-1129.

[51] A.J. Ninham, I.M. Hutchings & J.A. Little, *Erosion/oxidation of Austenitic and Ferritic alloys*, Corrosion Magazine, 46 April 1990, 296-301.

[52] B. Wang, G. Geng & A.V. Levy, *Erosion and corrosion of cooled 1018 steel*, Wear 161, 1993, 41-52.

[53] C.T. Kang, S.L. Chang, F.S. Pettit & N. Birks, *Synergism in the degradation of metals exposed to erosive high temperature oxidising temperatures*, Proc. Conf. Corrosion Erosion wear of materials at elevated temperatures.

[54] M. Olsson, P. Tarkpea & U. Engman, *Erosion - corrosion of a 2.25 Cr - 1 Mo steel exposed at low particle velocities*, Tribology International 28 (2), 1995, 107-117

[55] J.V. Cathcart & R.E. Pawel, *The mechanical behaviour of oxide scales*, Conf. Proc. : Corrosion/Erosion of Coal Conversion System Materials, January 24-26 1979, Berkeley California.

[56] R.R. Dils & P.S. Follansbee, *Dynamic oxidation and corrosion in power generating units*, Corrosion, 33 (11), Nov 1977, 385-402.

[57] D.J. Stephenson & J.R. Nicholls, *Modelling the influence of surface oxidation on high temperature erosion*, Wear 186-187, 1995, 284-290.

[58] J.A. Maasberg & A.V. Levy, *Erosion of elevated temperature corrosion scales on metals*, Wear 73, 1981, 355-370.

[59] G. Zambelli & A.V. Levy, *Erosion of oxide scales on metal substrates*, Conf, Proc. : Corrosion / Erosion of Coal Conversion System Materials Jan 24-26 1979, Berkeley California.

[60] I.G. Wright, V.K. Sethi & A.J. Markworth, *A generalized description of the simultaneous process of scale growth by high temperature oxidation and removal by erosive impacts*, Wear 186-187, 1995, 230-237.

[61] M.M. Stack, Private Communication, June 1995

[62] W. Tabakoff, R. Kotwal & A. Hamed, *Erosion study of different Materials affected by coal ash particles*, Wear 52, 1979, 161-173.

[63] M.M. Stack, S. Lekatos & F.H. Stott, *Erosion - corrosion regimes : number, nomenclature and justification ?,* Tribology International 28 (7), 1995, 445-451.

[64] G.P. Tilly, *Erosion caused by Airborne particles*, Wear 14, 1969, 63-79.

[65] T. Foley & A.V. Levy, *The erosion of heat treated steels*, Wear 91 (1), 1983, 45-64.

[66] Kane & Torebelli, *Selecting alloys to resist heat and corrosion*, Advanced Materials & Processes 4, 1993.

[67] A.V. Levy, *The solid particle erosion behaviour of steel as a function of microstructure*, Wear 68 (3), 1981, 269-287.

[68] K-H Zum Gahr, *Microstructure and wear of materials*, Tribology series 10, Elsevier 1987.

[69] A.V. Levy, Z.R. Shui & B.Q. Wang, *Erosion of Solid - Solution - Strengthed alloys*, Wear 127 (2), 1988, 193-205.

[70] I.M. Hutchings & A.V. Levy, *Thermal effects in the erosion of ductile materials*, Wear 131 (1), 1989, 105-121.

[71] R.A. Doyle & A. Ball, *On the thermomechanical effects during solid particle erosion*, Wear 151, 1991, 87-95.

[72] A.G. Davis, D.H. Boone & A.V. Levy, *Erosion of ceramic thermal barrier coatings,* Wear 110 (2), 1986, 101-116.

[73] S. Hogmark & P. Hedenqvist, *Tribological Characterisation of thin, hard coatings,* Wear 179, 1994, 147-154.

[74] P.J. Burnett & D.S. Rickerby, *The Wear and Erosion resistance of hard PVD coatings,* Surface Coatings & Technology 33, 1987.

[75] Chin-Chen Chiu & Yung Liou, *Low velocity impact damage in brittle coatings,* Journal of Materials Science 30, 1995, 1018-1024.

[76] M. Olsson, P. Hedenqvist, B. Stridh & S. Söderberg, *Solid particle erosion of hard chemically vapour deposited coatings,* Surface Coatings & Technology 37, 1989, 321-337.

[77] J.I. Quereshi & W. Tabakoff, *The influence of Coating process parameters on surface erosion resistance and substrate strength*, Surface Coatings & Technology, 36, 1988, 433-444.

[78] V. Shanov, W. Tabakoff & M. Metawally, *Erosive wear of CVD ceraminc coatings exposed to particulate flow,* Surface Coatings & Technology 54-55, 1992, 25-31.

[79] Z.R. Shui, B.Q. Wang & A.V. Levy, *Erosion of Protective Coatings*, Surface Coatings & Technology 43-44, 1990, 875-887.

[80] J.A. Sue & R.C. Tucker Jr, *High temperature erosion behaviour of Tungsten and Chromium Carbide based coatings,* Surface Coatings & Technology 32, 1987, 237-248.

[81] P.H. Shipway & I.M. Hutchings, *Measurement of coating durability by solid particle erosion,* Surface and Coatings Technology 71, 1994, 1-8.

[82] W.P. Bauver*, T.C. McGough* & J.G. McGowan#, *A facility for the characterisation of erosion of heat transfer tubes in coal fired power plants*, Combustion Eng Inc., Windsor Conneticut*, Dept Mech. Eng, University of Massachusetts, Amherst, Massachusetts# .

[83] Colcough & Yeomans, *The elevated temperature erosion behaviour of SiC and SiC - TiB_2*, Dept of Mat. Sci. and Eng, University of Surrey, Guildford, Surrey GU2 5XH, U.K.

[84] W. Tabakoff & T. Wakeman, *Test facility for material erosion at high temperatures, Erosion : Prevention and Useful Applications*, ASTM Spec. Tech. Publ. 664, 1978.

[85] J.B. Maxwell, *Data book on Hydrcarbons - Application to process engineering*, Robert E. Kriegler Publ. Cor. Inc., 1977.

[86] R.L. Perry, *Perry's Chemical Engineer's Handbook*, McGraw-Hill 1963.

[87] J.P. Holman, *Heat Transfer*, McGraw-Hill, 1989.

[88] J. Shackelford & W. Alexander, *The CRC Materials Science and Engineering Handbook*, CRC Press Inc., 1992.

[89] S.S. Willmott, *Test rig design to simulate ashlock valve erosion in coal gasification systems*, M.Sc. Thesis University of Cape Town, 1984.

[90] S. Chinnadurai & S. Bahadur, *High temperature erosion of Haynes and Waspaloy : effect of temperature and erosion mechanisms*, Wear 186-187, 1995, 299-305.

[91] A.J. Ninham & I.M. Hutchings, *A computer model for particle velocity calculation in erosion testing*, Paper 50, Proc. 6th Int. Conf. on Erosion by solid and Liquid Impact, University of Cambridge, 1983.

[92] J.F. Douglas, J.M. Gasiorek & J.A. Swaffield, *Fluid Mechanics*, John Wiley & Sons Inc. second edition, 1985.

[93] A.P. Fraas & M. Necati Ozisik, *Heat Exchanger Design*, John Wiley & Sons Inc., 1965.

[94] Y.A. Çengel & M.A. Boles, *Thermodynamics : An Engineering Approach*, McGraw-Hill, 1989.

[95] Danielson, *Air pollution engineering manual*, U.S. Dept of Health Education and Welfare, Public Health Service Publication No. 999-AP-40, Cincinnati Ohio, 1967.

[96] P.N. Cheremisinoff, *Air Pollution and Design Handbook*, Marcel Dekker Inc., 1977.

[97] R.J. Goldstein, *Fluid Mechanics Measurements*, Hemisphere publishing corporation, 1983.

[98] J.T. Miller, *The instrument manual*, United Trade Press Ltd, 1975.

[99] A.W. Ruff & L.K. Ives, *Measurement of Solid particle velocity in erosive wear*, Wear 35, 1975, 195-199.

[100] R.A. Vaughan, *The effects of hardness, toughness, microstructure and thermomechanical heating on the erosion of ceramic and ultrahard materials*, M.Sc. Thesis, University of Cape Town, 1991.

[101] R.G. Wellman, *Solid particle erosion of ceramics*, M.Sc. Thesis, University of Cape Town, 1993.

[102] R.C. Pankhurst & Holder, Sir Isaac Pitman & Sons 1952

[103] P.G. Shewmon, *Particle size threshold in the erosion of metals,* Wear 68, 1981, 253-258.

[104] I.M. Hutchings, *Predictions of the resistance of metals to erosion by solid particles*, Wear 35, 1975, 371.

[105] T.E. Howes, P.M. Rogers, J.A. Little & I.M. Hutchings, *Erosion-corrosion of mild steel in a temperature gradient*, Wear 186-187, 1995, 316-324.